

Aus dem Departement für Physik
Universität Freiburg (Schweiz)



Development of an optical cardio-magnetometer

Inaugural-Dissertation

zur Erlangung der Würde eines
Doctor rerum naturalium
der Mathematisch-Naturwissenschaftlichen Fakultät
der Universität Freiburg in der Schweiz

vorgelegt von

Georg Bison

aus Bonn (Deutschland)

Nummer der Dissertation: 1450

Universitätsdruckerei Freiburg

2004

Von der Mathematisch-Naturwissenschaftlichen Fakultät der Universität Freiburg
in der Schweiz angenommen, auf Antrag der Herren

Prof. Dr. Dionys Baeriswyl, Universität Freiburg (Präsident der Jury)

Prof. Dr. Antoine Weis, Universität Freiburg (Referent)

Priv.-Doz. Dr. Frank Scheffold, Universität Freiburg (Koreferent)

Dr. Sergio-Nicola Ern , Universit t Ulm (Koreferent)

Freiburg, den 4. Juni 2004

Der Leiter der Dissertation



Prof. Dr. Antoine Weis

Der Dekan



Prof. Dr. Dionys Baeriswyl

Abstract

This thesis describes the development of a new type of cardiomagnetometer, a device that can measure the magnetic field generated by the beating human heart. Such exceedingly weak magnetic fields carry diagnostically relevant information and can be measured noninvasively at the surface of the body. Cardiomagnetic measurements were previously performed using superconducting magnetometers (SQUID) that have the required sensitivity (< 1 pT) to measure field changes fifty million times smaller than the earth's magnetic field. However, SQUIDs need to be cooled using liquified gases. The cost associated with that cooling is one of the reasons that prevented the widespread use of magnetocardiometry (MCG) in medical practice, despite the fact that MCG measurements have proven to be beneficial in the diagnosis of heart diseases.

The new type of cardiomagnetometer described herein is based on a completely different technology, optically detected magnetic resonance (ODMR), that does not need expensive cooling. ODMR combines laser spectroscopy and magnetic resonance in a vapor of paramagnetic atoms—Cs in our case—sealed in a glass cell. The angular momenta (spins) of the atomic valence electrons determine the optical properties of the medium. Magnetic fields can change those optical properties because of the coupling between the spin and the field mediated by the magnetic moment. This allows us to determine the magnetic field from a measurement of the alteration of optical properties such as the absorption coefficient.

The method is known since the 1960's and commercial lamp-based devices are used by archaeologists and geologists to measure variations of the earth's magnetic field. In contrast to those devices our magnetometer uses a frequency-stabilized diode-laser as light source. Under optimal conditions the magnetometer has a resolution of 63 fT/Hz^{1/2} and a detection bandwidth of 140 Hz using a cell of 6 cm³ volume. We used two such magnetometers in a gradiometric configuration to suppress interfering magnetic fields. One sensor was mounted close to the heart measuring both the heart field and the interfering field. The second sensor, some distance away, measured only the interfering field since the heart field drops rapidly with increasing distance. Homogeneous interfering fields cancel in the differential signal from both sensors. This setup allowed us to measure heart magnetic fields in weakly shielded environments.

By measuring the field at different positions in a plane above the chest a map of the heart magnetic field can be obtained. Using ECG-triggered averaging we could measure such maps for all times in the cardiac cycle. The dynamics of the magnetic field maps from four healthy volunteers were compared to SQUID-generated reference data. A direct comparison of magnetic field maps recorded with a commercial

SQUID magnetometer and with our optical magnetometer was performed at the University of Rome. The results shows that the data are compatible and makes us confident that optical cardiomagnetometry may be used one day as a standard medical technique.

Zusammenfassung

Diese Arbeit beschreibt die Entwicklung eines neuen Typs von Kardiomagnetometer, d. h. eines Geräts mit dem man das Magnetfeld des schlagenden menschlichen Herzens messen kann. Diese ausserordentlich schwachen Magnetfelder tragen medizinisch relevante Informationen und können nichtinvasiv an der Oberfläche des Körpers gemessen werden. Bisher wurden solche Messungen ausschließlich mit supraleitenden Magnetometern (SQUID) durchgeführt, welche die notwendige magnetometrische Empfindlichkeit (< 1 pT) haben, um Feldänderungen, die fünfzig Millionen Mal kleiner als das Erdmagnetfeld sind, nachzuweisen. SQUIDs sind allerdings auf eine aufwändige Kühlung mit verflüssigten Gasen angewiesen. Die mit der Kühlung verbundenen Kosten sind einer der Gründe dafür, dass sich die Kardiomagnetometrie bis jetzt nicht in der medizinischen Praxis etablieren konnte, trotz der erwiesenen Vorteile der Methode bei der oft schwierigen Diagnose von Herzkrankheiten.

Der neue Typ eines Kardiomagnetometers, der in dieser Arbeit beschrieben wird, basiert auf einer völlig anderen Technik, der optisch detektierten Magnetresonanz (ODMR), welche ohne Kühlung auskommt. Die ODMR kombiniert Laserspektroskopie und Magnetresonanz in einem Dampf von paramagnetischen Atomen — in diesem Fall Cäsium — in einer evakuierten Glaszelle. Der Drehimpuls (Spin) der Valenzelektronen der Atome bestimmt die optischen Eigenschaften des Dampfes. Da der Spin über das assoziierte magnetische Moment auch mit Magnetfeldern wechselwirkt, kann ein äusseres Magnetfeld die optischen Eigenschaften des Mediums beeinflussen. Somit kann aus einer Messung dieser Eigenschaften, wie z.B. dem Absorptionskoeffizienten, das Magnetfeld bestimmt werden.

Die Methode ist seit den sechziger Jahren bekannt und in kommerziellen Geräten verfügbar, die von Archäologen und Geologen eingesetzt werden, um Variationen des Erdmagnetfeldes zu messen. Im Gegensatz zu diesen Geräten, in denen als Lichtquelle Spektrallampen verwendet werden, benutzt unser Magnetometer einen frequenzstabilisierten Diodenlaser als Lichtquelle. Unter optimierten Bedingungen erreicht das Magnetometer eine Auflösung von $63 \text{ fT/Hz}^{1/2}$ und eine Bandbreite von 140 Hz mit einem Zellenvolumen von 6 cm^3 . Um Störfelder im Labor zu unterdrücken, betrieben wir zwei solcher Sensoren in einer gradiometrischen Anordnung. Dabei misst ein Sensor so nah wie möglich am Herz das Herzmagnetfeld zusammen mit den Störungen. Der zweite Sensor etwas weiter entfernt vom Herz misst nur noch die Störungen, da das Herzmagnetfeld schnell mit wachsender Entfernung abfällt. Im Differenzsignal fallen dann die homogenen Störungen heraus, was es uns ermöglicht hat, Herzmagnetfelder in einer schwach magnetisch abgeschirmten Umgebung zu messen.

Durch die Messung des Herzmagnetfeldes an verschiedenen Stellen über der Brust lassen sich Magnetfeldkarten des Herzen erzeugen. Dank EKG-getriggelter Mittelung gelang es, solche Karten für jeden Zeitpunkt des Herzzyklus zu messen. Die Dynamik der Herzmagnetfeldkarten von vier gesunden Probanden haben wir mit SQUID generierten Referenzdaten verglichen. Ein direkter Vergleich der Magnetfeldkarten von zwei Probanden gemessen mit einem kommerziellen SQUID Magnetometer und unserem optischen Magnetometer wurde an der Universität Rom durchgeführt. Die Ergebnisse zeigen, dass die Daten kompatibel sind, was uns zuversichtlich stimmt, dass optische Herzmagnetometrie eines Tages als medizinisches Standardverfahren etabliert werden könnte.

Contents

1	Introduction	3
1.1	Optically detected magnetic resonance in Cs atoms	3
1.1.1	The Cs atom	4
1.1.2	Optical pumping	4
1.1.3	Optically detected magnetic resonance as a three-step process	7
1.2	Magnetocardiography	8
1.2.1	Electrophysiological background	9
1.2.2	The cardiomagnetic field	12
2	Optimization and performance of an optical cardiomagnetometer	17
2.1	Introduction	17
2.2	Principle of scalar OPM operation	18
2.2.1	The M_x magnetometer	19
2.2.2	Nyquist plots	22
2.3	Experimental Setup	25
2.4	Optimization	27
2.4.1	Intrinsic resolution	28
2.4.2	Bandwidth	30
2.4.3	Experimental lineshapes	32
2.4.4	Optimization measurements	33
2.5	Results	34
2.5.1	Dependence on rf amplitude	34
2.5.2	Dependence on temperature and light power	35
2.6	Conclusion	37
2.7	Appendix A: The Cramér–Rao bound for frequency measuring magnetometers	39
2.8	Appendix B: The Cramér–Rao bound for phase measuring magnetometers	40
3	A laser-pumped magnetometer for the mapping of human cardiomagnetic fields	43

4	Dynamical mapping of the human cardiomagnetic field with a room-temperature, laser-optical sensor	53
4.1	Introduction	53
4.2	Experimental method and setup	54
4.3	Results	56
4.4	Conclusion	58
5	Mapping of the cardiomagnetic field using a room-temperature magnetometer	61
5.1	Introduction	61
5.2	Methods	61
5.3	Results	65
5.4	Discussion	65
6	Comparison of magnetocardiographic mapping with SQUID-based and laser-pumped magnetometers in normal subjects	69
6.1	Introduction	69
6.2	Methods	70
6.3	Results	70
6.4	Discussion	70
7	Conclusions and Outlook	77
7.1	Future improvements of the sensor	77
7.1.1	Coated cells	77
7.1.2	Double pass	78
7.1.3	Higher order gradiometers	78
7.1.4	Multichannel arrangement	80
7.2	Outlook	80
	Danksagung	83
	Curriculum vitae	85

Preface

The present Ph.D. thesis is a continuation of my Diploma Thesis [1] with which I graduated from the *Institut für Angewandte Physik der Universität Bonn, Germany* under the supervision of Prof. A. Weis. All studies and developments described here were carried out at the *Departement für Physik der Universität Freiburg, Switzerland* to where the group of Prof. Weis moved in the spring of 2000.

Five original articles represent the main work of this thesis. It is organized so that each of the Chapters 2 to 6 can be read as an independent text, which includes an introduction, a description of the experiment, results, a discussion, and the references of the article. The order of the articles was chosen for better comprehension and deviates from the chronological order of submission. The articles included are:

Chapter 2 *Optimization and performance of an optical cardiomagnetometer*, G. Bison, R. Wynands, and A. Weis, accepted for publication by JOSA B (2004).

Chapter 3 *A laser-pumped magnetometer for the mapping of human cardiomagnetic fields*, G. Bison, R. Wynands, and A. Weis, Appl. Phys. B **76**, 325 (2003).

Chapter 4 *Dynamical mapping of the human cardiomagnetic field with a room-temperature, laser-optical sensor*, G. Bison, R. Wynands, and A. Weis, Optics Express **11**, 904 (2003).

Chapter 5 *Mapping of the cardiomagnetic field using a room-temperature magnetometer*, G. Bison, R. Wynands, and A. Weis, Biomed. Tech. **48**, Suppl. 2, (2004), in press.

Chapter 6 *Comparison of Magnetocardiographic Mapping with SQUID-based and Laser-pumped Magnetometers in Normal Subjects*, R. Fenici, G. Bison, R. Wynands, D. Brisinda, A. M. Meloni, and A. Weis, Biomed. Tech. **48**, Suppl. 2, (2004), in press.

Chapter 2 describes the principles and the performance of the optical magnetometer used for the measurements reported in Chapters 3 to 5. It concentrates on the intrinsic sensitivity of the sensors and provides theoretical limits as well as an experimental optimization of the performance. The relatively high temperature of operation (53°C) that turned out to be optimum for magnetometric sensitivity and response bandwidth of the magnetometer was not used in the first biomagnetic

measurements. The performance of the magnetometer used for the experiments described in Chapters 4 to 5 was therefore slightly worse than the optimized values described in Chapter 2.

Chapter 3 is a brief report about our first measurement of a magnetic field map (MFM) of the heart using an optical magnetometer. The chapter represents the state of the experiment presented at the 13th International Conference on Biomagnetism held in 2002 in Jena.

Chapter 4 describes the extension of the technique using ECG-triggered averaging in order to generate magnetic field maps at any time during the cardiac cycle. The free online journal Optics Express was chosen for publication because of the possibility to publish movies of the measured MFM dynamics.

Two studies comparing data measured with optical magnetometer and with superconducting sensors (SQUID) were presented at the Conference on Noninvasive Functional Source Imaging in Chieti in September 2003. Chapter 5 and 6 are proceedings papers of that conference. Chapter 5 deals with the comparison of data measured with our optical magnetometer to SQUID generated reference data. The SQUID data were measured in the group of Prof. Van Leeuwen with healthy subjects different from our volunteers. The second study presented in Chapter 6 compares the magnetocardiograms of the same volunteers measured with the two methods. Therefore the Fribourg team travelled to Prof. Fenici's lab in Rome where SQUID based MCGs of Robert Wynands and Georg Bison were measured and compared to the data recorded with the optical magnetometer.

Chapter 1

Introduction

This introduction is divided into two parts and provides details about the basic principles that are not included in the articles of Chapters 2 - 5. The first part introduces relevant concepts of atomic spin physics, the technology our magnetometer is based on. The second part describes the electrophysiological processes that generate the magnetic field of the heart.

1.1 Optically detected magnetic resonance in Cs atoms

The magnetic moment associated with the electronic spin of paramagnetic atoms is a sensitive probe for many interesting phenomena. These magnetic moments can produce a macroscopic magnetization which greatly enhances magnetic effects when the spins of the medium are aligned along a common axis. An efficient way to produce such spin polarized media, called optical pumping, was discovered by J. Brossel and A. Kastler in 1949 [2]. This method uses circularly polarized light that excites the atoms by transferring the polarization of the light to the atoms. The same light can also be used for the efficient detection of changes in spin orientation when monitoring specific properties of the light that has passed through the medium (see Fig. 1.1).

Both the optical preparation and the detection can be used to monitor in an efficient way magnetic resonance transitions in the atom [3, 4], a technique called optically detected magnetic resonance (ODMR).

The sensitivity of the magnetic resonance to magnetic fields has been used in atomic magnetometers since 1958 [5] to measure the earth's magnetic field. The development of ODMR magnetometers is based on the work of W. E. Bell, A. L. Bloom, and H. G. Dehmelt [4, 6, 7]. The performance of ODMR magnetometers for earth magnetic field measurements has been pushed to its limits by E. B. Alexandrov and co-workers [8].

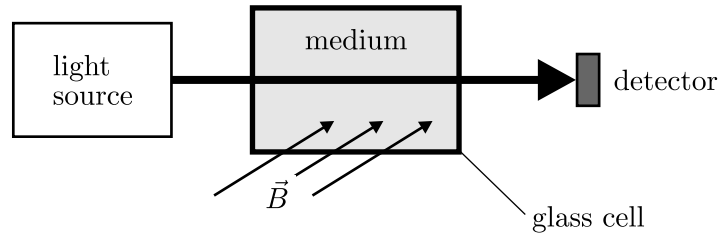


Figure 1.1: Schematic setup of an ODMR experiment. The light source—usually a laser or a spectral lamp—emits the light beam that passes through the medium consisting of an atomic vapor sealed in an evacuated glass cell. An external magnetic field \vec{B} acts on the spins of the atoms, thereby changing the optical properties of the medium. These changes can be detected by measuring the properties of the transmitted light.

1.1.1 The Cs atom

As stated above, paramagnetic atoms, like the alkali metals K, Rb, and Cs, are needed as a medium for optical magnetometers. We have chosen Cs for several reasons, like the availability of diode lasers for the relevant optical transition and the relatively high vapor pressure at room temperature. Another advantage is that Cs, the heaviest stable alkali metal, possesses only one stable isotope, ^{133}Cs with a nuclear spin of $I = 7/2$.

Cs has a hydrogen-like electron configuration with a $6S_{1/2}$ ground state that splits into two hyperfine states with total angular momentum quantum numbers of $F = 3, 4$. The lowest-lying excited states are $6P_{1/2}$ (D_1 transition) and $6P_{3/2}$ (D_2 transition). The magnetometer uses only the D_1 transition from $6S_{1/2}$ to $6P_{1/2}$ shown in Fig. 1.2. The excited state, like the ground state, is split into two hyperfine levels, yielding four allowed absorption lines. The separation of the ground state levels is 9.19 GHz, while the separation of the excited states is 1.38 GHz, large enough to produce resolved Doppler broadened absorption lines. Each hyperfine state splits into $(2F + 1)$ Zeemann substates under the influence of a small external magnetic field. The $F = 4$ ground state detected via the transition from $6S_{1/2} F = 4$ to $6P_{1/2} F = 3$ was found to have maximum magnetometric sensitivity. The laser light source used for the magnetometer was actively stabilized to that transition using a dichroic atomic vapor laser lock (DAVLL) [9]. The spectrally resolved hyperfine structure of the Cs D_1 transition results in a reliable frequency control of the laser light.

1.1.2 Optical pumping

The process of optical pumping uses light to change the population distribution among the Zeemann sublevels in the ground state of atoms. The relevant optical pumping for ODMR magnetometers uses circularly polarized light to align the spins

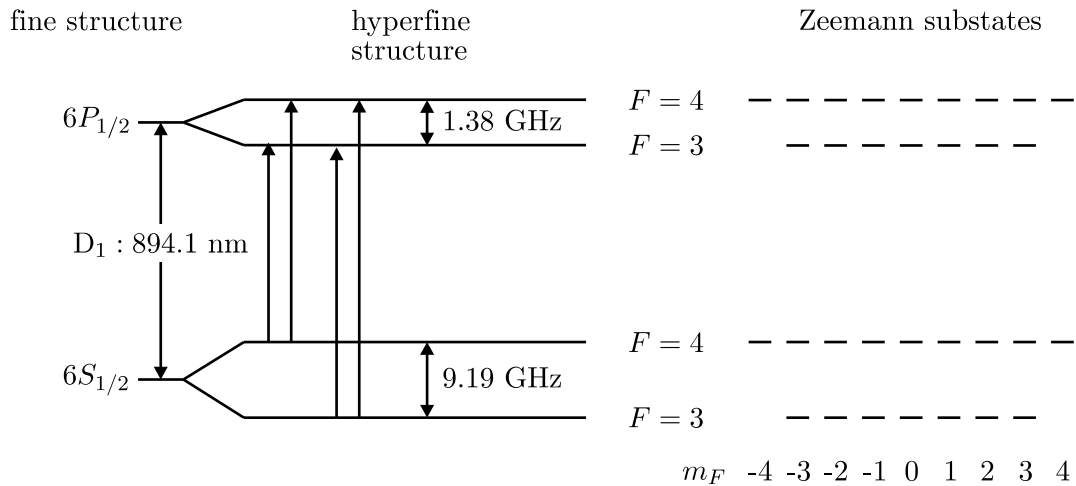


Figure 1.2: Energy diagram of the Cs D_1 transition (not to scale). The fine-structure levels split into two hyperfine levels each. Each hyperfine level has $2F + 1$ Zeeman sublevels.

of the atoms with the \vec{k} vector of the light. The Zeemann levels of the transition used are shown in Fig. 1.3 a.

If an atom absorbs a photon the angular momentum of the photon is transferred to the atom because of angular momentum conservation. If, for example, a quantum of σ_+ polarized light is absorbed the atom changes its magnetic quantum number m_F by $+1$. From the excited state the atom can decay via one of three possible decay channels which lead to an overall change of the ground state m_F value by 0 , $+1$, or $+2$. The probabilities for the absorption and the different decay channels are determined by their Clebsch-Gordan coefficients. Since there is a finite probability for the atom to decay into a level with a larger m_F value, the atom is “pumped” towards states with increasing angular momentum if the process of absorption and emission is repeated several times.

For each of those absorption-emission cycles, called optical pumping cycles, a photon of the incident light beam is absorbed. The photons spontaneously emitted by the atom when it decays back to the ground state have equal probability to be sent in any direction. As a result only a very small fraction of that fluorescence light travels along the incident light beam. Almost any photon scattered in an optical pumping cycle therefore decreases the intensity of the light beam.

The optical pumping process stops when the atom happens to fall into one of the two outermost states of the $F = 4$ hyperfine level, the so-called dark states (see Fig. 1.3a). From these ground states the atom cannot absorb any light since there is no corresponding excited state. The expression “dark state” was chosen because the sample emits no fluorescence light when the atoms are in dark states.

The existence of dark states provides an efficient way to detect spin orientation. The transmitted intensity becomes a maximum if all atoms are pumped into the dark

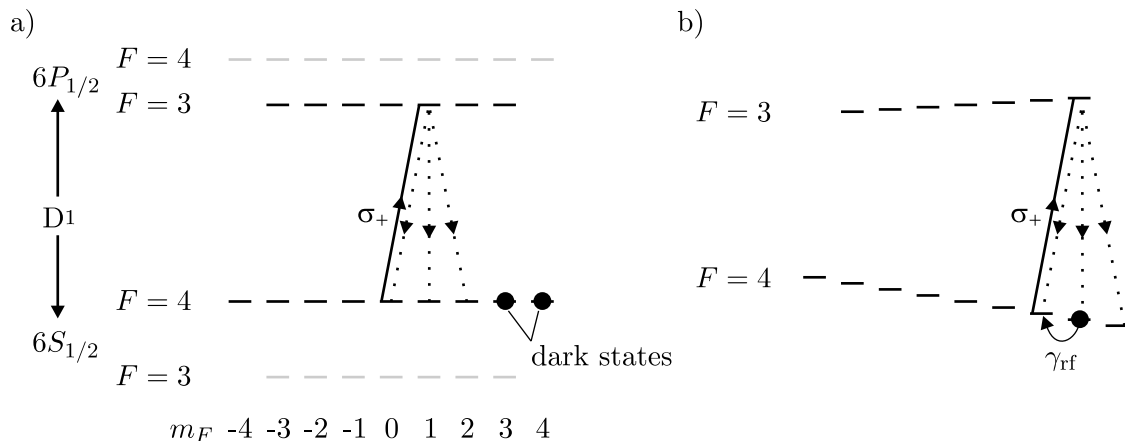


Figure 1.3: a) Zeemann structure of the Cs D₁ line with magnetic sublevels with quantum numbers m_F . The ordinate represents the energies of the levels (not to scale). The optical pumping process with circularly (σ_+) polarized light leads, after a few absorption-emission cycles, to the population of a dark state in which the atom cannot absorb the light any more. b) The Zeemann levels of the relevant transition when a magnetic field is applied. The atom can be transferred from the dark state to other spin states using a radio frequency photon γ_{rf} . Subsequently at least one pumping cycle is necessary to bring the atom back to the dark state.

state. The spin state of an atom can be changed to an absorbing (non dark) state (see Fig. 1.3b) by absorption of resonant radio frequency radiation. Subsequently at least one pumping cycle is needed to bring the atom back to the dark state, thus absorbing at least one optical photon from the light beam. If the transmitted intensity of the beam is measured the absorption of rf photons can thus be directly monitored via the absorption of optical photons, which represents an increase in energy of the respective quanta by 11 orders of magnitude. In this picture an atom in a dark state acts as a quantum amplifier with a energy amplification of 110 dB. The same effect is used in ODMR set-ups, in which the spins of the atoms periodically change from dark to absorbing states, thereby modulating the transmitted intensity [3].

In real media relaxation mechanisms, which try to reestablish thermal population distributions, work against the optical pumping. One important relaxation mechanism are wall collisions during which atoms stick to the wall of the glass cell for a finite amount of time. Their spins are rapidly depolarized by the fields from magnetic impurities in the glass, leaving the atom in an arbitrary spin state m_F when it leaves the surface. Two techniques have been developed in order to reduce such spin disturbing wall collisions. In the first method the addition of an inert buffer gas in the cell is used to suppress the ballistic flight of the atoms to the walls at a speed of about 300 m/s. Due to collisions with the buffer gas the alkali atom rather diffuses slowly through the gas atmosphere [6]. Frequent choices for the buffer gas are He, Ne, Ar, or N₂, which have a very small cross section for spin depolariza-

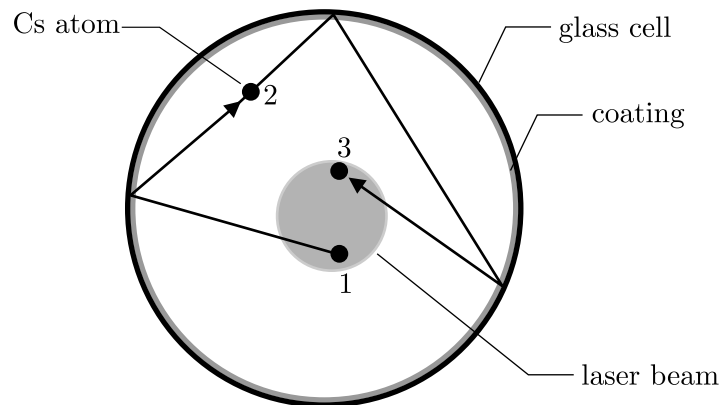


Figure 1.4: The three-step model of ODMR. 1: Optical pumping, 2: Interaction with fields, 3: Probing of the atom

tion. Another method is to coat the surface of the cell with a substance like paraffin or silane that strongly reduce the sticking time of the alkali atoms to the wall. In coated cells the atoms undergo hundreds of wall collisions without their spin being noticeably perturbed. In this respect the spin lifetime or spin decoherence time may be defined as the average time between two spin-disturbing processes. In well-coated cells the spin lifetime can exceed 1 s [8].

Another important relaxation mechanism is magnetic field components, that are not parallel to the spin and thereby cause it to precess. On the other hand, the spin precession in transverse fields is also used in a coherent way in ODMR magnetometers in which the atoms are made to precess with equal phase (see Chapter 2) by imposing that phase through a rotating magnetic field. For practical reasons this field is produced by the one of the rotating components of a linearly polarized field. When the rotating field is not applied the incoherent precession of the atoms acts like a decoherence process that destroys the spin polarization in the medium.

1.1.3 Optically detected magnetic resonance as a three-step process

Optically detected magnetic resonance can, like other nonlinear magneto-optical effects, be understood as a three-step process [10]: optical pumping process, interaction with external fields, probing process (see Fig. 1.4). This picture is complementary to the model introduced in Chapter 2, which describes what happens in step 2 in a more quantitative way. In an optical magnetometer those three steps occur in parallel in the same cell where atoms are pumped, interact with the fields, and are probed in a continuous way. However, each atom individually evolves through the three steps:

- 1. Optical pumping:** The process is started when the atom crosses the laser beam. The circularly polarized light optically pumps the atom, aligning its

spin with the \vec{k} vector of the light beam (see section 1.1.2). In this model we assume that the light is strong enough to pump the atom to a dark state during the time the atom spends in the laser beam.

- 2. Interaction with external fields:** After the atom has left the laser beam the spin of the atom can evolve freely. It precesses around the applied magnetic field at the Larmor frequency (see Chapter 2 for details). During this time the spin accumulates an increasing phase angle. The longer is the interaction time of spin and field the more information about the field is collected by the spin and the more precisely the field can be measured. However, this information is lost by dephasing collisions of the atom, for instance with an uncoated cell wall.
- 3. Probing:** The atom is probed by the light when it reenters the laser beam. The information about the magnetic field is gained from the phase accumulated during the spin precession in step 2. If the atom has precessed to an absorbing state, i.e., if the spin is not aligned with the \vec{k} vector of the light, it is pumped back to the dark state, thereby absorbing some of the laser light. This situation can be detected as a decrease of the transmitted power. Since the atom is pumped to the dark state the probing process is also the starting process of the next three-step cycle.

A macroscopic amplitude modulation of the transmitted light can be achieved when a large fraction of the atoms rotate coherently in phase. This is necessary since incoherent phases would average out the modulation. The coherence is assured by an additional rotating magnetic field resonant with the Larmor frequency, which synchronizes the precession of the atomic spins.

The three step model is applicable to many nonlinear optical processes [11] and well visualizes the principles of optically detected magnetic resonance. The more quantitative model used in Chapter 2 treats the optical pumping as a relaxation process that pumps the spin state towards the dark state in an exponential manner.

1.2 Magnetocardiography

The history of magnetocardiography [12] started 1963 when Gerhard Baule and Richard McFee measured the first magnetocardiogram (MCG) using induction coils [13]. 1970 David Cohen was the first to use a SQUID to measure MCGs [14]. Since then SQUIDs were the detectors of choice that allowed Kariniemi et al. in 1974 to record the first fetal magnetocardiogram [15]. In 1981 Livanov et al. used discharge-lamp pumped optical magnetometers, operated at room temperature, to record the human magnetocardiogram [16]. At that time optical magnetometers could not be established in the MCG community that continued to use SQUIDs. In 1990 Schneider et al. demonstrated a multichannel magnetocardiography system covering the whole chest [17] that decreased the time for measuring a magnetic field map significantly. Large efforts were invested in the development of more affordable cardio-magnetometers using high-temperature SQUIDs, first demonstrated by

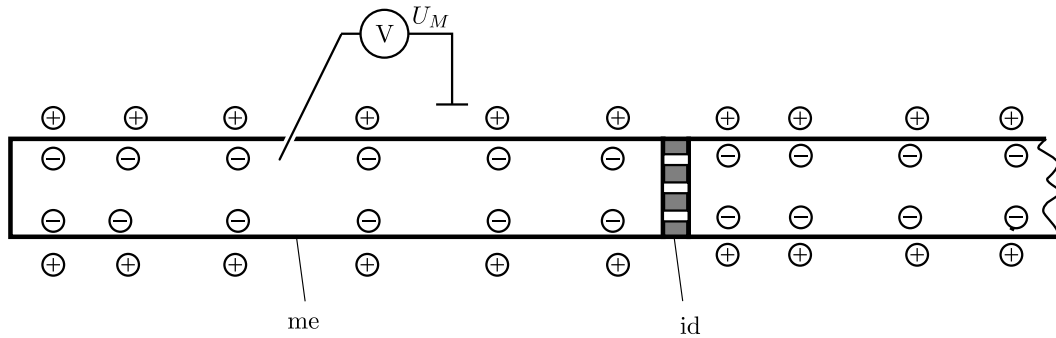


Figure 1.5: Schematic picture of a heart muscle cell. The membrane (me) forms the outer bound of the cell and is impermeable for the ions schematically shown as circles. The transmembrane potential can be measured with a probe. The intercalated disks (id) that connect neighboring cells are permeable for ions.

Saburo Tanaka et al. in 1994 [18]. As an alternative to SQUIDS, a MCG measurement using flux-gate magnetometers was presented in 1998 [19].

1.2.1 Electrophysiological background

The magnetic field generated by the beating heart is a consequence of electric currents flowing in the muscle tissue of the heart (myocardium). Those currents are carried by ions involved in the electrophysiological processes that trigger the mechanical contraction of the heart. The same processes also produce the electric potential differences that are measurable as the electrocardiogram at the surface of the body.

The heart muscle consists of muscle cells that are about $100\ \mu\text{m}$ long with a diameter of about $15\ \mu\text{m}$ [20]. As shown in Fig. 1.5 the cells are stacked together with intercalated disks between them. Each cell consists of a membrane separating the inner volume of the cell from the surrounding intercellular liquid [21]. The membrane consists of lipids and has a high permeability for water and some other molecules. However, it is impermeable for charged molecules and ions like the physiologically relevant Na^+ , K^+ , Cl^- , and Ca^{2+} . The electrophysiology of muscles and nerves is based on the exchange of those ions between the inner volume of the cell and the surrounding volume. Since the membrane itself is impermeable for ions, special gating proteins (ion channels), specific for each type of ions, are needed to control the flux of ions through the membrane. That flux is influenced by electric forces, concentration differences, the gating proteins that control the permeability of the membrane and special proteins that actively pump Na^+ out of the cell and K^+ into it using physiological energy [21].

Concentration differences of ions across the membrane lead to a transmembrane potential U_M , i.e., the voltage difference between the inside and the outside of the

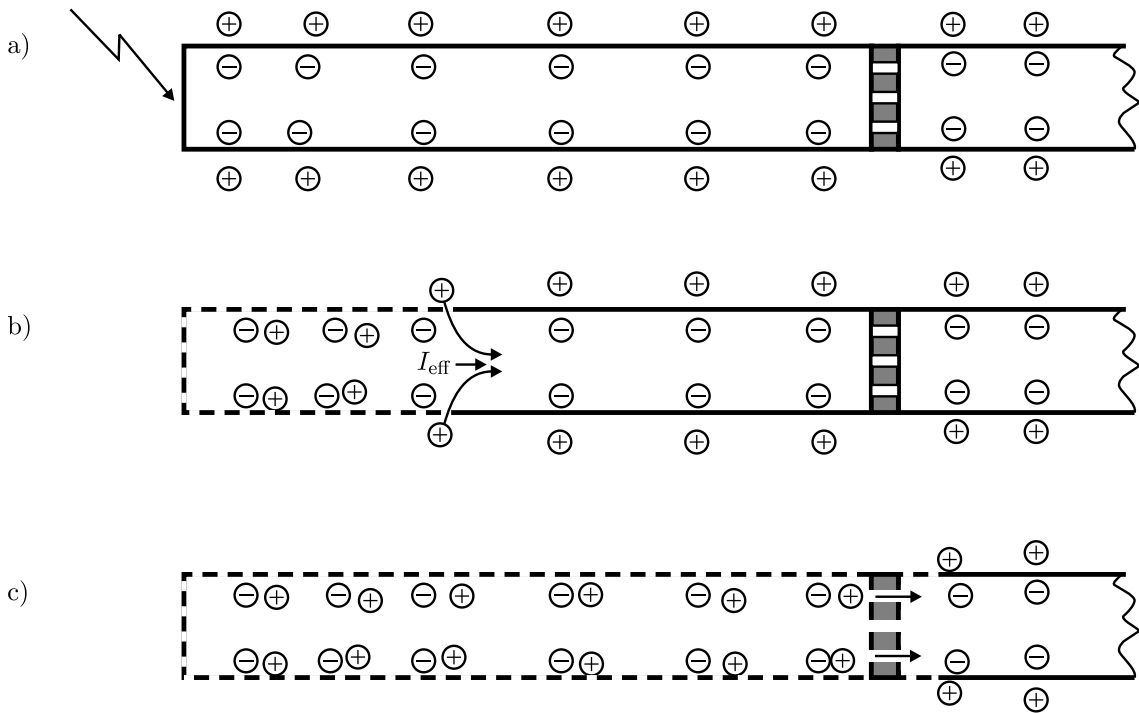


Figure 1.6: a) A muscle cell that is electrically stimulated at one end. The stimulus raises the transmembrane potential above threshold in the region where it was applied. As a consequence the Na^+ channels in that region are opened and Na^+ ions flowing into the cell further increase the potential. b) Attracted by the negative charges at the other end of the cell the Na^+ ions move along the cell raising the transmembrane potential over threshold in a larger region. The currents caused by these ions sum up to an effective current I_{eff} along the cell. c) When a muscle cell is completely depolarized the next cell is triggered by ions moving through channels in the intercalated disk. This chain reaction moves along the heart muscle fibers at a speed of about 1 m/s until all muscle cells in the heart are depolarized.

membrane. Since the membrane capacitance is rather small (about $1 \mu\text{F}/\text{cm}^2$) tiny concentration differences lead to a significant transmembrane potential U_M . In the inactive state U_M is stabilized by an equilibrium of the different ion diffusion processes to a value of about -70 mV . However, if the cell is electrically stimulated, i.e., U_M is raised above a threshold potential the situation changes drastically. The Na^+ channels are opened, allowing Na^+ ions, accelerated by electrical forces, to flow into the cell, further raising U_M to zero or even slightly positive values. This process is called depolarization and manifests itself as a depolarization wave travelling along the muscle cell (Fig. 1.6).

The main part of the ionic current causing the depolarization flows normal to the cell membrane and contributes no net magnetic field because of symmetry [20]. A small fraction of this current, however, moves along the cell carrying the depolarization wave (Fig. 1.6 b). The return current is carried by ions as well and flows

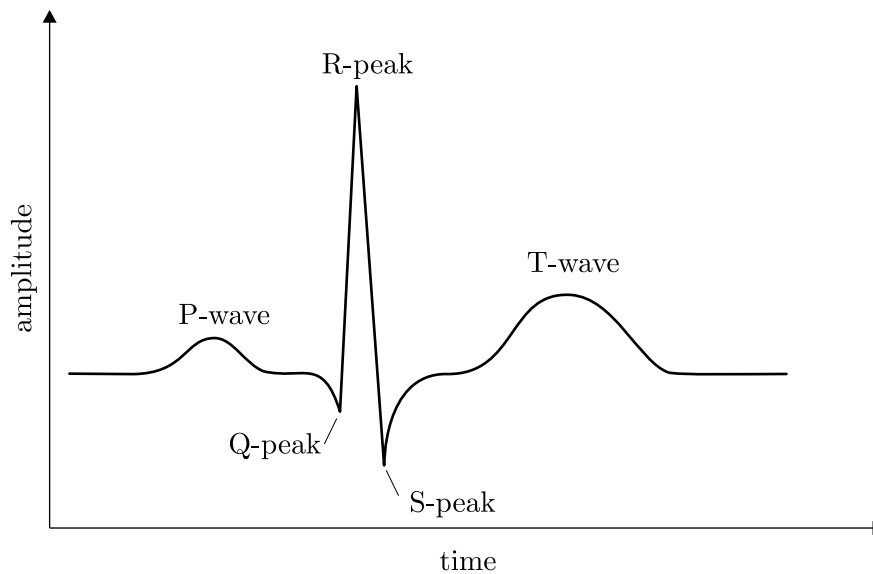


Figure 1.7: Schematical cardiac signal with standard labelling of the different events in the cardiac cycle. The Q-peak, R-Peak and S-peak together are called QRS-complex. Electrocardiograms and magnetocardiograms have the same basic shape because they are generated by the same electrophysiological processes.

through the intercellular medium. Under some constraints that are relatively well fulfilled in the human heart, it can be shown [22] that the return current does not contribute to the magnetic field. This leaves the small current segment I_{eff} , a current dipole with a source at one end of the heart muscle cell and a sink at the other end, as the primary source of the heart's magnetic field.

Many electrophysiological processes are triggered by the depolarization. One of these leads to increased Ca^{2+} permeability of the membrane, largely increasing the usually very low concentration of Ca^{2+} ions in the cell. The Ca^{2+} ions in the cell trigger its mechanical contraction which follows the depolarization with a small delay.

The heart beat is generated at the sinoatrial node which triggers both atrial heart chambers. This first depolarization is electrically as well as magnetically detectable as P-wave (see Fig. 1.7). After the atrium is completely depolarized the main (ventricular) heart muscle is triggered via the His bundles. The depolarization wave moving along the ventricular myocardium generates the QRS-complex (see Fig. 1.7).

200 ms after the depolarization of the muscle cells the repolarization process is started. This process restores the polarized state of the cell mainly by allowing K^+ ions to move out of the cell [21]. This repolarization progresses in a similar way as the depolarization but with smaller currents that act over a longer time. The resulting currents for the ventricular repolarization generate the T-wave shown in Fig. 1.7. The depolarization-repolarization cycle has increased the Na^+ concentration and decreased the K^+ concentration in the cell. This change is cleared by the sodium

pump of the cell pumping out three Na^+ ions in exchange for two K^+ ions that are pumped in. Finally, the transmembrane potential is held at a stable level until the cell is triggered again.

1.2.2 The cardiomagnetic field

The magnetic field of the heart is generated by the ionic current flowing inside the heart muscle cells. The diffuse return current through the intercellular medium does not contribute to the magnetic field [22], as mentioned above. The magnetic fields from the individual current dipoles of the active cells in the heart sum up to the magnetic field that can be measured at the surface of the body. A simplified model of the heart magnetic field can be obtained by summing up all active current dipoles in a total current vector that is also called the “heart vector”.

Figure 1.8 a shows the magnetic field lines generated by the total current dipole. The standard magnetocardiogram (MCG) is a measurement of the z -component of this field in a plane above the source. Magnetic field maps (MFM) are obtained by measuring at different points in that plane and can be visualized as contour plots. Figure 1.8 b shows the contour plot calculated for the current shown in Fig. 1.8 a. Current dipoles generate MFMs that are symmetrical with respect to the projection of the dipole on the measurement plane. Such dipolar maps feature a positive region where the field lines enter the plane and a negative region where they come out of the plane. The connecting line between those positive and negative regions is perpendicular to the current dipole.

Real magnetic field maps (see Fig. 1.9), are mainly bipolar with some deviation due to the fact that the heart generates many elementary current dipoles with different orientations distributed over the extended volume of the heart. Modelling of the electric activity of the heart is an active research field that has developed much more sophisticated models than the simple dipole. The actual shape of the heart is used in such models to reconstruct the current distribution in the heart muscle from the MCG measurements (current density imaging see Chapter 6). Such current distributions for different times in the cardiac cycle represent the information the cardiologists are interested in.

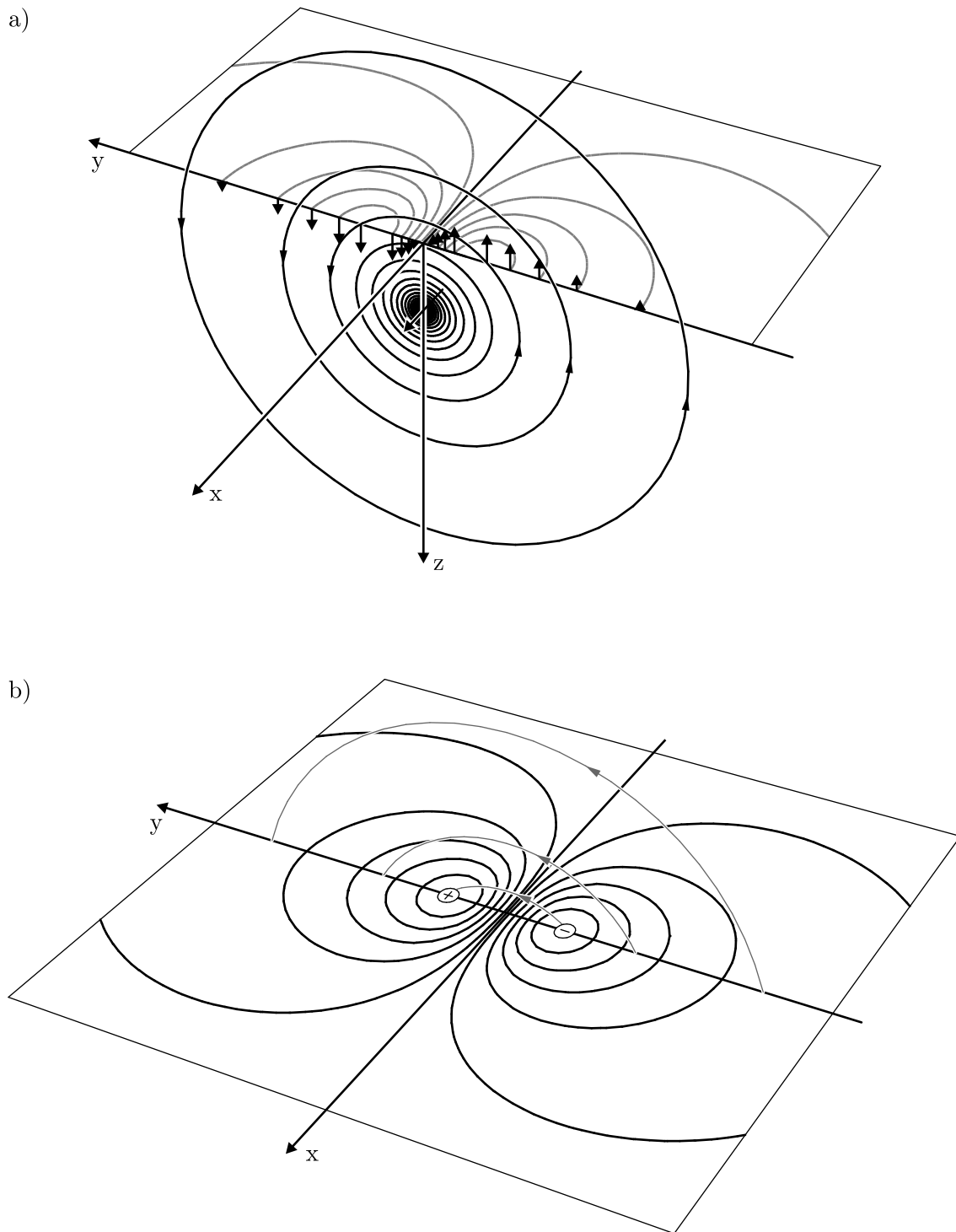


Figure 1.8: a) The small current element (current dipole) in the center generates circular field lines. The contour plot of B_z is shown on a surface parallel to the surface of the chest. The vertical arrows show the outwards and inwards (positive z direction) pointing B_z components. b) full contour plot (black) and field lines above the chest (gray lines). The current dipole is oriented perpendicular to the line that connects the positive (+) and the negative (-) regions of the contour plot.

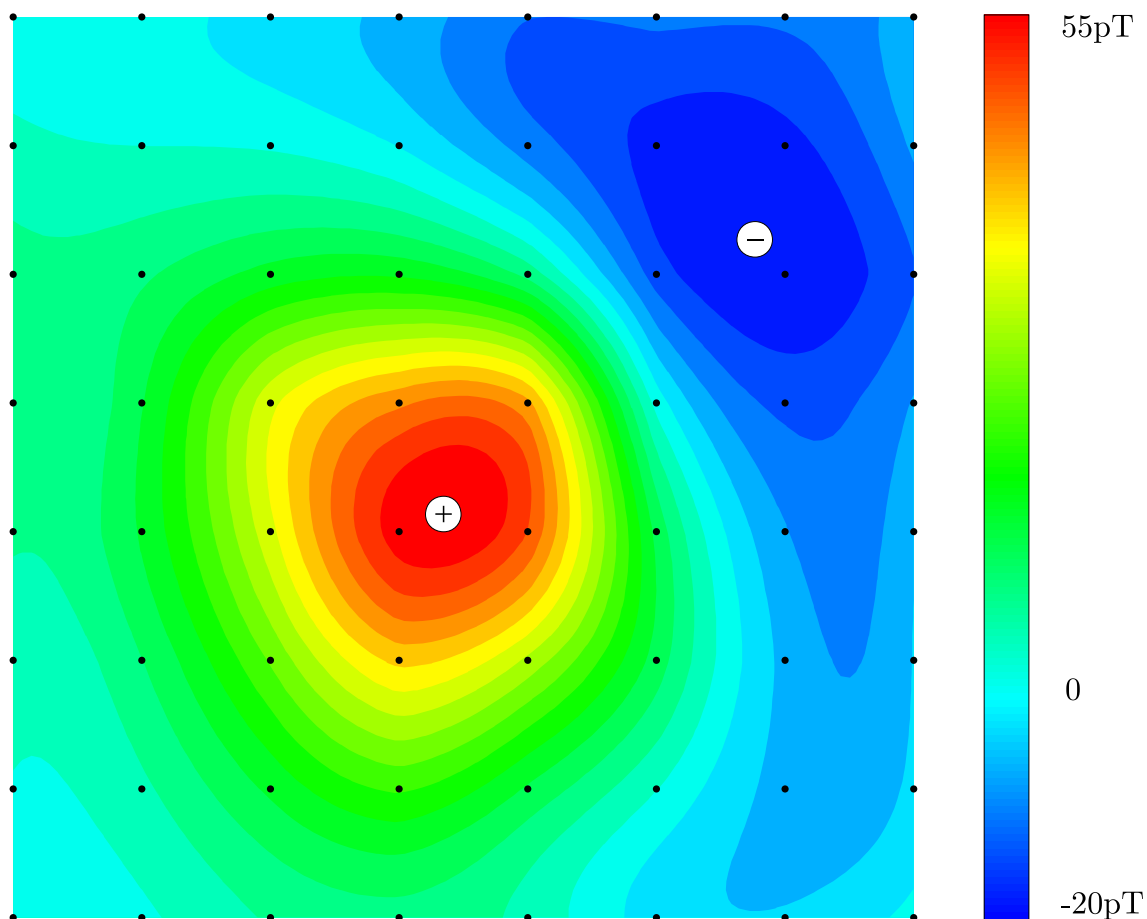


Figure 1.9: Contour plot of the magnetic field map at the R-peak measured with the optical magnetometer. The values between the measurement points (shown as dots) were calculated using third order polynomial interpolation.

References

- [1] G. Bison. Diplom Thesis (Universität Bonn, 2000).
- [2] J. Brossel and A. Kastler. La détection de la résonance magnétique des niveaux excités - l'effet de dépolarisation des radiations de résonance optique et de fluorescence. *C. R. Acad. Sci. URSS*, **229**(23):1213–1215, 1949.
- [3] H. G. Dehmelt. Modulation of a light beam by precessing absorbing atoms. *Phys. Rev.*, 105 (5):1924–1925, 1957.
- [4] W. E. Bell and A. L. Bloom. Optical detection of magnetic resonance in alkali metal vapor. *Phys. Rev.*, 107 (6):1559–1565, 1957.
- [5] T. L. Skillman and P. L. Bender. Measurement of the earth's magnetic field with a rubidium vapor magnetometer. *J. Geophys. Res.*, 63 (3):513–515, 1958.
- [6] H. G. Dehmelt. Slow spin relaxation of optically polarized sodium atoms. *Phys. Rev.*, 105 (5):1487–1489, 1957.
- [7] A. L. Bloom. Principles of operation of the rubidium vapor magnetometer. *Appl. Opt.*, 1:61–68, 1962.
- [8] E. B. Alexandrov and V. A. Bonch-Bruевич. Optically pumped atomic magnetometers after three decades. *Opt. Eng.*, 31(4):711–717, 1992.
- [9] K. L. Corwin, Z.-T. Lu, C. F. Hand, R. J. Epstein, and C. E. Wieman. Frequency-stabilized diode laser with the Zeeman shift in an atomic vapor. *Appl. Optics*, 37(15):3295–3298, 1998.
- [10] A. Weis, J. Wurster, and S. I. Kanorsky. Quantitative interpretation of the nonlinear Faraday effect as a Hanle effect of a light-induced birefringence. *J. Opt. Soc. Am. B*, 10(4):716–724, 1993.
- [11] D. Budker, W. Gawlik, D. F. Kimball, S. M. Rochester, V. V. Yashchuk, and A. Weis. Resonant nonlinear magneto-optical effects in atoms. *Rev. Mod. Phys.*, 74 (4):1153–1201, 2002.
- [12] Brief History of Magnetocardiography: www.magnetocardiography.info.
- [13] G. M. Baule and R. McFee. Detection of the magnetic field of the heart. *Am. Heart J.*, 66:95–96, 1963.
- [14] D. Cohen, E. A. Edelsack, and J. E. Zimmerman. Magnetocardiograms taken inside a shielded room with a superconducting point-contact magnetometer. *Appl. Phys. Lett.*, 16:278–280, 1970.
- [15] V. Kariniemi, J. Ahopelto, P.J. Karp, and T.E. Katila. The fetal magnetocardiogram. *J. Perinat. Med.*, 2:214–216, 1974.

- [16] M. N. Livanov, A. N. Kozlov, S. E. Sinelnikova, Ju. A. Kholodov, V. P. Markin, A. M. Gorbach, and A. V. Korinewsky. Record of the human magnetocardiogram by the quantum gradiometer with optical pumping. *Adv. Cardiol.*, 28:78–80, 1981.
- [17] S. Schneider, E. Hoenig, H. Reichenberger, K. Abraham-Fucks, W. Moshage, W. Oppelt, A. Stefan, A. Weikl, and A. Wirth. Multichannel biomagnetic system for study of electrical activity of the brain and the heart. *Radiology*, 176:825–830, 1990.
- [18] S. Tanaka, H. Itozaki, H. Toyoda, N. Harada, A. Adachi, K. Okajima, H. Kado, and T. Nagaishi. Four-channel $\text{YBa}_2\text{Cu}_3\text{O}_{7-y}$ dc squid magnetometer for biomagnetic measurements. *Appl. Phys. Lett.*, 64:514–516, 1994.
- [19] C. Dolabdjian, S. Saez, A. Reyes Toledo, and D. Robbes. Signal-to-noise improvement of bio-magnetic signals using a flux-gate probe and real time signal processing. *Rev. Sci. Inst.*, 69 (10):3678–3680, 1998.
- [20] J. P. Wikswo. Biomagnetic sources and their models. In S. J. Williamson, editor, *Proceedings of the Seventh International Conference on Biomagnetism, New York, 13-18 August 1989*, page 1, New York, 1989. Plenum Press.
- [21] R. F. Schmidt and G. Thews. *Physiologie des Menschen*. Springer (Berlin, Heidelberg), 27th edition, 1997.
- [22] D. Cohen and H. Hosaka. Magnetic field produced by a current dipole. *J. Electrocard.*, 9:409-417, 1976.

Chapter 2

Optimization and performance of an optical cardiomagnetometer

G. Bison
R. Wynands
A. Weis

Accepted for publication by the Journal of the Optical Society of America (JOSA) B.

Cardiomagnetometry is a growing field of noninvasive medical diagnostics that has triggered a need for affordable high sensitivity magnetometers. Optical pumping magnetometers (OPM) are promising candidates satisfying that need since it has been demonstrated that they can be used to map the magnetic field of the beating human heart. We discuss the principle of a phase detecting OPM and describe the procedures used to optimize its performance. The optimized OPM has an intrinsic magnetometric sensitivity of $63 \text{ fT/Hz}^{1/2}$ and a measurement bandwidth of 140 Hz with a spatial resolution of 28 mm, measured in a weakly shielded environment. We further discuss the fundamental limitations of frequency and phase detecting magnetometers based on information theory.

2.1 Introduction

Biomagnetometry is a rapidly growing field of noninvasive medical diagnostics [1]. In particular, the magnetic fields generated by the human heart and brain carry valuable information about the underlying electrophysiological processes [2]. Since the 1970s superconducting quantum interference devices (SQUIDs) have been used to detect these generally very weak biomagnetic fields [3]. The magnetic field of the human heart is the strongest biomagnetic signal, with a peak amplitude of 100 pT, but since this is still orders of magnitude weaker than typical stray field interference the measurement of such signals could initially only be performed inside expensive

magnetically-shielded rooms (MSR). Progress in medical research in the past decade has motivated a need for more affordable cardiomagnetic sensors. Recently, multi-channel SQUIDs were developed that no longer require shielding due to the use of gradiometric configurations. Such devices are commercially available but are still quite expensive in both capital and operational costs.

Optical pumping magnetometers (OPM) have been widely known since the 1960s [4], and offer both high sensitivity and reliable operation for research [5] and applications like geomagnetometry [6]. Since OPMs usually work with a near room-temperature thermal alkali metal vapor, they avoid the need for the cryogenic cooling that makes SQUIDs so costly and maintenance intensive. Our goal was to develop an affordable, maintenance-free device that is both sensitive and fast enough to measure the magnetic field of the human heart. In order to be competitive with the well-established SQUIDs, a cardiomagnetic sensor has to offer a magnetic field sensitivity of at least 1 pT with a bandwidth of about 100 Hz. Furthermore, the spatial resolution of the sensor has to be better than 4 cm, the standard separation of grid points during mapping.

Since the cardiomagnetometry community is mainly interested in one of the components of the magnetic field vector, one might think of using vector-type OPMs like the Hanle magnetometer [7] or the Faraday magnetometer, devices which operate in zero fields only [8]. However, these devices lose their sensitivity in the presence of even tiny field components in directions perpendicular to the field of interest. The broadening caused by such transverse field components must be kept well below the width of the magnetometer resonance [8], thus limiting those components to values below a few tenths of pT. Accordingly, optical vector magnetometers cannot be used for cardiomagnetometry in a straightforward way since the heart field features time-varying transverse field components on the order of 100 pT. We have therefore concentrated on the Cs based M_x OPM, which exhibits a fast response and which has been shown to be sufficiently sensitive in an unshielded environment. Furthermore, lamp-pumped M_x OPMs were used for the first biomagnetic measurements [9] with optical magnetometers in the early 1980s, although that work was discontinued. Instead of lamps, we use diode lasers as a light source in order to build a device that will scale to the many channels needed for fast mapping of the cardiomagnetic field.

2.2 Principle of scalar OPM operation

Optically pumped magnetometers operate on the principle that the optical properties of a suitable atomic medium are coupled to its magnetic properties via the atomic spin. The ensemble average of the magnetic moments associated with the spins can be treated as a classical magnetization vector $\vec{M} = N_F g_F \mu_B \langle \vec{F} \rangle / \hbar$ in space. Here $N_F \langle \vec{F} \rangle = N_F \text{tr}(\rho_F \vec{F})$ with $\text{tr} \rho_F = 1$ is the total angular momentum of N_F atoms in an optical hyperfine level F where ρ_F is the density matrix, μ_B the Bohr magneton, and g_F the Landé factor of the state. Optical magnetometers detect changes of the medium's optical properties induced by the precession of \vec{M} in a magnetic field \vec{B}_{tot} . The frequency of this precession, the Larmor frequency ω_L ,

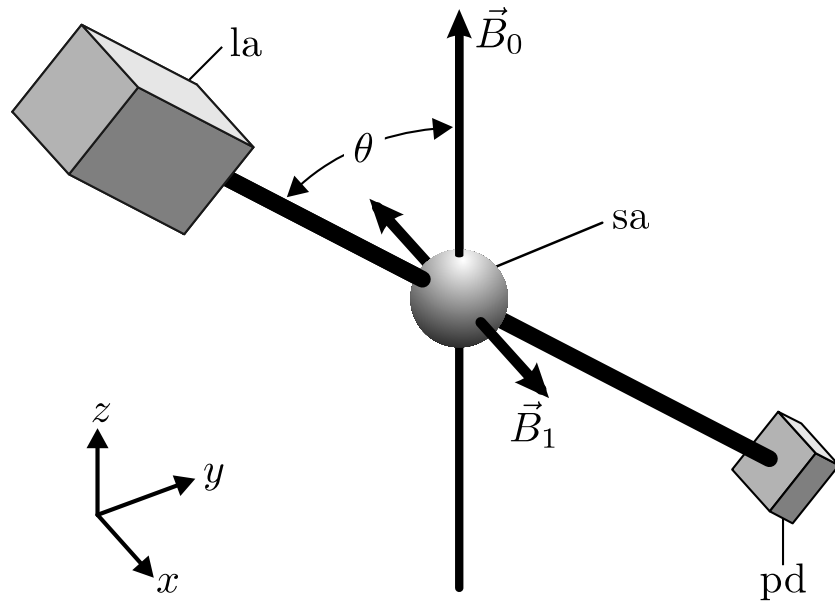


Figure 2.1: Basic geometry of the M_x -magnetometer setup: The laser (la) emits a beam that traverses the sample (sa) at angle θ with respect to the magnetic field \vec{B}_0 . The transmitted power is detected by a photodetector (pd). The static magnetic field \vec{B}_0 is aligned along the z -direction. The oscillating magnetic field \vec{B}_1 is aligned along the x -direction.

is proportional to the modulus of \vec{B}_{tot} :

$$\omega_L = \frac{g_F \mu_B}{\hbar} |\vec{B}_{\text{tot}}| \equiv \gamma_F |\vec{B}_{\text{tot}}|. \quad (2.1)$$

For Cs the constant of proportionality, γ_F , has a value of $2\pi \times 3.5$ Hz/nT. All atomic vapor magnetometers measure the magnetic field via a direct or indirect measurement of the Larmor frequency.

2.2.1 The M_x magnetometer

In the case of the M_x magnetometer, a magnetic-resonance technique is used to measure the Larmor frequency directly, by employing two perpendicular magnetic fields \vec{B}_0 and \vec{B}_1 . The static magnetic field \vec{B}_0 is aligned along the z -direction. As Fig. 2.1 shows, the \vec{k} -vector of the laser beam lies in the yz -plane and is oriented at an angle θ with respect to the z -direction. The magnetometer is sensitive to the modulus of \vec{B}_0 . The oscillating magnetic field $\vec{B}_1 = \hat{x} B_{1f} 2 \cos \omega_{rf} t$ is aligned along the x -direction with an amplitude much smaller than B_0 .

In order to introduce the basic concepts we discuss the simplest case of an $F = 1/2$ state. The motion of \vec{M} under the influence of \vec{B}_0 and \vec{B}_1 is then given by the Bloch equations:

$$\begin{aligned} \begin{pmatrix} \dot{M}_x \\ \dot{M}_y \\ \dot{M}_z \end{pmatrix} &= \begin{pmatrix} M_x \\ M_y \\ M_z \end{pmatrix} \times \begin{pmatrix} \gamma_F B_{\text{rf}} 2 \cos \omega_{\text{rf}} t \\ 0 \\ \gamma_F B_0 \end{pmatrix} \\ &\quad - \begin{pmatrix} \gamma_2 M_x \\ \gamma_2 M_y \\ \gamma_1 M_z \end{pmatrix} + \Gamma_P \begin{pmatrix} -M_x \\ M_0 \sin \theta - M_y \\ -M_0 \cos \theta - M_z \end{pmatrix}. \end{aligned} \quad (2.2)$$

The first term describes the precession of \vec{M} around the magnetic fields. The second term describes the longitudinal (γ_1) and transverse (γ_2) relaxation of \vec{M} . The third term represents the effect of optical pumping with circularly polarized light that creates the magnetization. It can be treated as an additional relaxation leading to an equilibrium orientation aligned with the \vec{k} -vector of the incoming light at the pumping rate Γ_P . Both relaxations add up to the effective relaxation rates $\Gamma_{1,2} = \gamma_{1,2} + \Gamma_P$. In the case of small B_{rf} amplitudes, Eq. (2.2) can be solved using the rotating-wave approximation [10] which leads to a steady-state solution where \vec{M} rotates around \vec{B}_0 at the driving frequency ω_{rf} .

The optical property used in the M_x magnetometer is the optical absorption coefficient which determines the power, P , of the light transmitted through the medium. For circularly polarized light, the transmitted power is proportional to the projection of \vec{M} on the \vec{k} -vector of the incoming light. Therefore, the precessing magnetization results in a modulation of the absorption index measurable as an oscillation of P . The in-phase and quadrature components of P with respect to the driving field can be obtained from Eq. (2.2):

$$P_{\text{ip}}(\delta) = -P_0 \sin(2\theta) \frac{\Omega_{\text{rf}} \delta}{\Omega_{\text{rf}}^2 \Gamma_2 / \Gamma_1 + \Gamma_2^2 + \delta^2}, \text{ and} \quad (2.3)$$

$$P_{\text{qu}}(\delta) = -P_0 \sin(2\theta) \frac{\Omega_{\text{rf}} \Gamma_2}{\Omega_{\text{rf}}^2 \Gamma_2 / \Gamma_1 + \Gamma_2^2 + \delta^2}. \quad (2.4)$$

Here $\Omega_{\text{rf}} = \gamma_F B_{\text{rf}}$ is the Rabi frequency and $\delta = \omega_{\text{rf}} - \omega_L$ the detuning of the oscillating field \vec{B}_1 from the Larmor frequency. The constant P_0 combines all factors such as the initial light power, the number of atoms in the sample, and the cross section for light-atom interactions determining the absolute amplitude of the signal. The components can be measured using phase-sensitive detection. The signals are strongest for $\theta = 45^\circ$, which was used in all experiments.

Both P_{ip} and P_{qu} show resonant behavior near $\delta = 0$. P_{qu} has an absorptive Lorentzian line shape, and P_{ip} has a dispersive Lorentzian line shape with the same half width expressed as

$$\Delta\omega_{\text{HW}} = \sqrt{\Omega_{\text{rf}}^2 \Gamma_2 / \Gamma_1 + \Gamma_2^2} = \Gamma_2 \sqrt{S + 1}. \quad (2.5)$$

Here $S = \Omega_{\text{rf}}^2 / (\Gamma_1 \Gamma_2)$ is the saturation parameter of the rf field. Figure 2.2(a) shows measured line shapes under conditions optimized for maximal magnetometric sensitivity (see Sec. 2.4 for details).

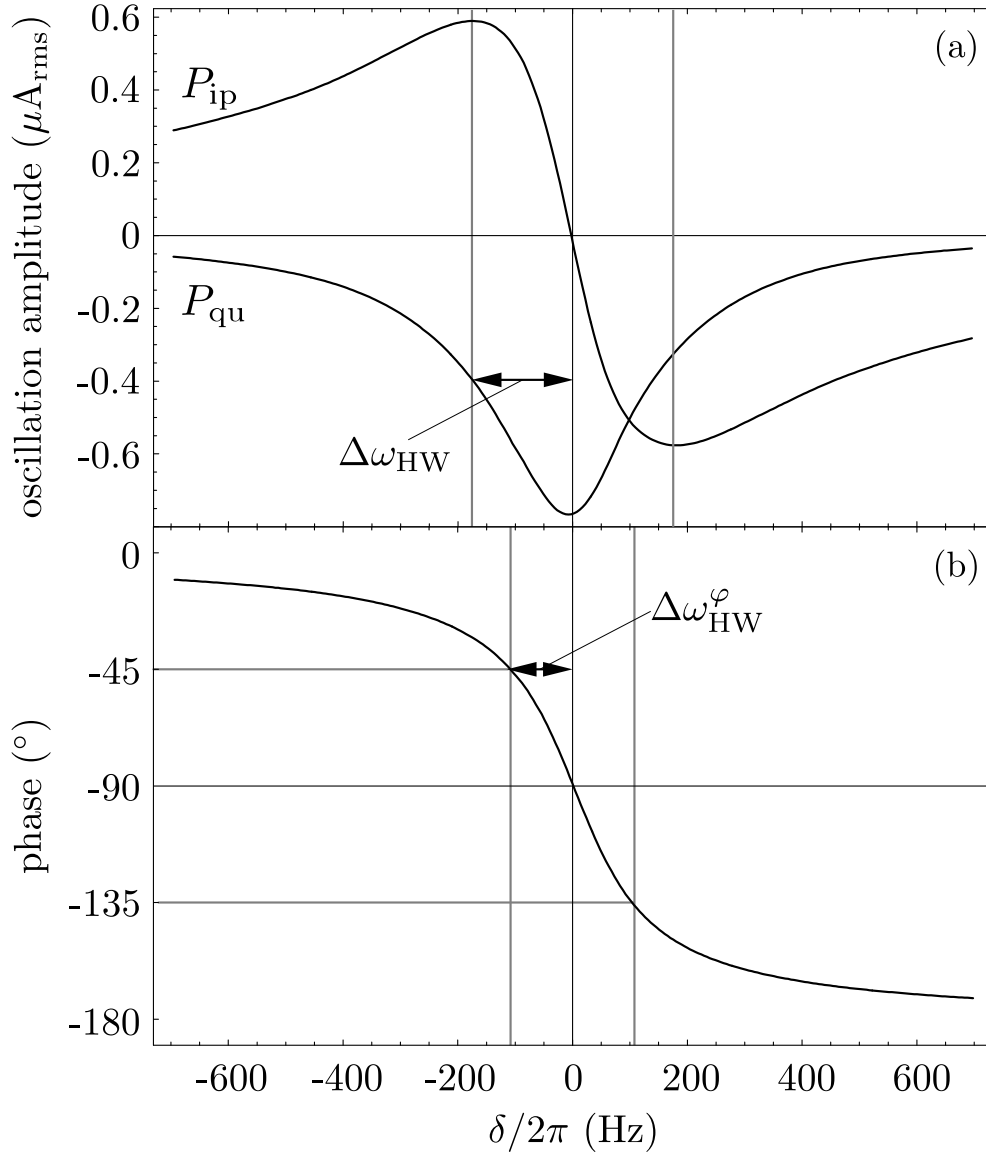


Figure 2.2: (a) Measured magnetic resonance lineshapes of the in-phase (a_1) and quadrature signals (a_2), measured in a single sweep of 20 s with the cardiomagnetometer placed in a poorly shielded room. Magnetic 50 Hz line interference was suppressed using a 4th order lowpass filter (time constant 10 ms). The half-width, derived from a fit, was $\Delta\omega_{\text{HW}}/2\pi = 173$ Hz. (b) Magnetic resonance line shape of the oscillation phase measured with respect to the driving field B_{rf} . The data was obtained in real time using a digital lock-in amplifier. The fitted half-width is: $\Delta\omega_{\text{HW}}^\phi/2\pi = 109$ Hz.

Signal P_{ip} is of particular interest because it has a dispersive shape, featuring a steep linear zero-crossing at $\delta = 0$. In this region P_{ip} can be used to measure the deviation of \vec{B}_0 from the value that corresponds to ω_{rf} . The same is true for the deviation of the phase difference φ between the measured oscillation and the driving field from -90° (see Fig. 2.2(b)). The phase difference φ can be calculated from P_{ip} and P_{qu} , yielding

$$\tan \varphi = \frac{P_{\text{qu}}}{P_{\text{ip}}} = \frac{\Gamma_2}{\delta}. \quad (2.6)$$

The phase signal changes from $\varphi = 0$ at low frequencies to $\varphi = -\pi$ at high frequencies. For practical reasons it is preferable to shift the phase by 90° so that it passes through zero in the center of the resonance ($\delta = 0$). This can easily be done by shifting the reference signal by $\pi/2$ using the corresponding feature of the phase detector. In mathematical terms that 90° shift is equivalent to the transformation $P_{\text{qu}} \rightarrow -P_{\text{ip}}$ and $P_{\text{ip}} \rightarrow P_{\text{qu}}$, yielding

$$\tan \varphi' = -\frac{\delta}{\Gamma_2}. \quad (2.7)$$

The width of the phase signal $\Delta\omega_{\text{HW}}^\varphi$ is smaller than $\Delta\omega_{\text{HW}}$ because it is not affected by rf power broadening, i.e., it is independent of Ω_{rf} :

$$\Delta\omega_{\text{HW}}^\varphi = \Gamma_2 < \Delta\omega_{\text{HW}}. \quad (2.8)$$

The narrower lineshape of the phase signal is exactly compensated by a better S/N ratio of P_{ip} [see Eqs. (2.5), (2.10), and (2.11)] resulting in a statistically equivalent magnetic field resolution for both signals. However, since the lineshape of the phase signal depends only on Γ_2 , it is easier to calibrate in absolute field units. Furthermore, light amplitude noise, for instance caused by fluctuating laser intensities, does not directly affect the phase signal, since both P_{ip} and P_{qu} scale in the same way with light intensity. Only the much weaker coupling via the light shift can cause the phase signal to reflect light amplitude noise. Considering those practical advantages of the phase signal we concentrate in the following sections on the sensitivity of the phase signal to magnetic field changes.

2.2.2 Nyquist plots

The lineshapes $P_{\text{ip}}(\delta)$, and $P_{\text{qu}}(\delta)$ of the magnetic resonance have a major influence on the magnetometric sensitivity. The magnetic resonances in Eqs. (2.3) and (2.4) can be interpreted as a complex transfer function $t(\omega)$ connecting the current that drives the rf-coils, $I_i = I_0 \exp(i\omega t) + c.c.$, and the photocurrent $I_p = t(\omega)I_i$ of the photodiode. By setting the effective transverse relaxation rate Γ_2 as the unit of frequency and using the normalized detuning $x (= \delta/\Gamma_2)$, t can be written in dimensionless units as:

$$t = t_0 \frac{\sqrt{S}(i+x)}{1+S+x^2}. \quad (2.9)$$

A parametric plot of $t(x)$ in the complex plane — called a Nyquist plot — was found to be useful for the inspection of experimental data. In this representation

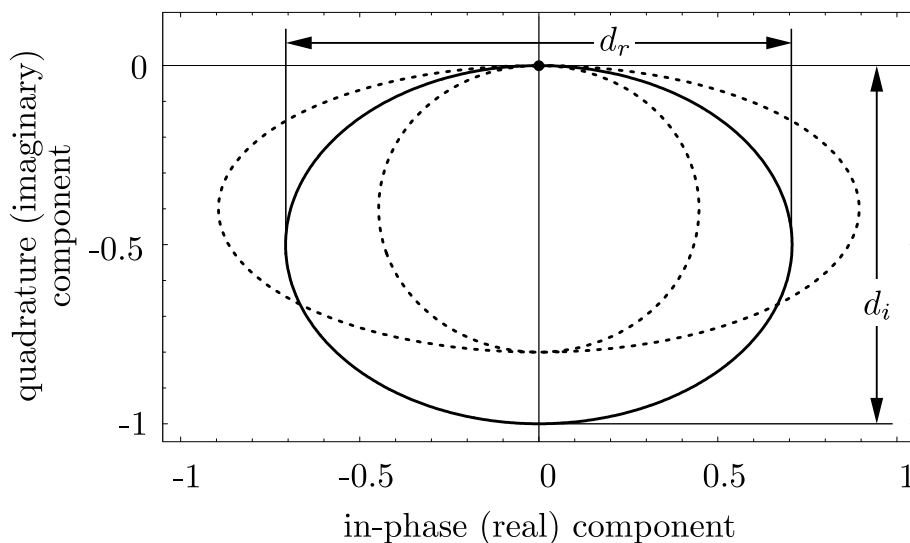


Figure 2.3: Nyquist plots for three different values of S . The solid line is for $S = 1$, the dashed lines are for $S = 0.25$ (nearly round) and $S = 4$ (elliptical), respectively. If ω_{rf} is scanned towards increasing values the system evolves clockwise through the Nyquist plot.

$t(x)$ appears as an ellipse with diameters d_r and d_i for the real (in-phase) and imaginary (quadrature) components respectively (see Fig. 2.3):

$$d_r = t_0 \sqrt{\frac{S}{1+S}} \quad (2.10)$$

$$d_i = t_0 \frac{\sqrt{S}}{1+S}. \quad (2.11)$$

The saturation parameter of the rf transition, S , can be extracted from the ratio of the two diameters:

$$S = \frac{\Omega_{\text{rf}}^2}{\Gamma_1 \Gamma_2} = \frac{d_r^2}{d_i^2} - 1. \quad (2.12)$$

Figure 2.4 shows a Nyquist plot of a resonance for a situation in which an interfering sine wave is added to the photocurrent, leading to a shifted ellipse. The amplitude r_i and the phase φ_i of the interference can be easily extracted from the Nyquist plot. A phase shift in the demodulation leads to a rotated ellipse. In this situation the spectra of in-phase $P_{\text{ip}}(\delta)$ and quadrature $P_{\text{qu}}(\delta)$ components as a function of rf detuning appear asymmetric.

By means of Nyquist plots it is easy to distinguish between an asymmetry caused by improper adjustment of the lock-in phase and one caused by inhomogeneous broadening. The latter causes a deviation from the elliptical shape. One model for inhomogeneous broadening is to assume a gradient in the static magnetic field. Since we use buffer-gas cells the atoms do not move over large distances during their spin coherence lifetime so that inhomogeneous magnetic fields are not averaged out.

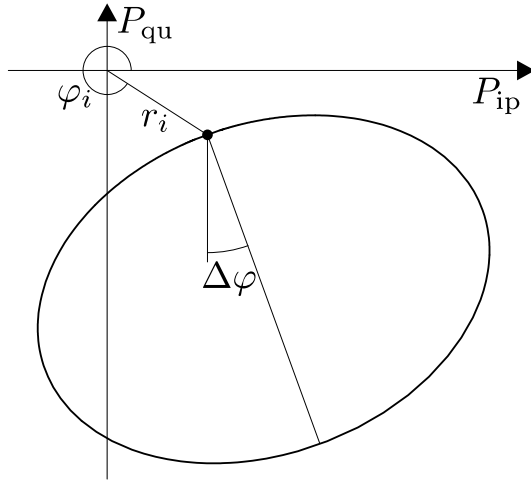


Figure 2.4: Nyquist plot of a resonance with $S = 1$ when an interfering sine wave of amplitude r_i and phase φ_i is added. A phase offset of $\Delta\varphi$ in the demodulation due to a poorly adjusted lock-in phase leads to a rotated ellipse.

Instead, atoms at different locations in the cell see different magnetic fields, resulting in an inhomogeneous broadening of the magnetic resonance line.

Figure 2.5 shows calculated Nyquist plots for different gradients of the static field \vec{B}_0 . The simplest model for such an inhomogeneity is a constant gradient dB_z/dz over the length l_z of the cell. This is expressed by a convolution of the theoretical magnetic resonance signals $t(x)$ [see Eq. (2.9)] with the normalized distribution of magnetic fields $g(x)$ which, in this case, is a constant over the interval

$$2x_g = \frac{\gamma_F}{\Gamma_2} l_z dB_z/dz. \quad (2.13)$$

Since $g(x)$ vanishes everywhere except for $-x_g \leq x \leq x_g$ the convoluted resonance t' is given by

$$t'(x) = \int_{-x_g}^{x_g} t(x-x') g(x') dx', \quad (2.14)$$

which can be evaluated analytically

$$\begin{aligned} t' = & \frac{\sqrt{S}}{4x_g} \left[\ln \left\{ 1 + S + (x_g - x)^2 \right\} \right. \\ & \left. - \ln \left\{ 1 + S + (x_g + x)^2 \right\} \right] \\ & - \frac{i}{2x_g} \sqrt{\frac{S}{1+S}} \left\{ \arctan \left(\frac{x_g - x}{\sqrt{1+S}} \right) \right. \\ & \left. + \arctan \left(\frac{x_g + x}{\sqrt{1+S}} \right) \right\}. \end{aligned} \quad (2.15)$$

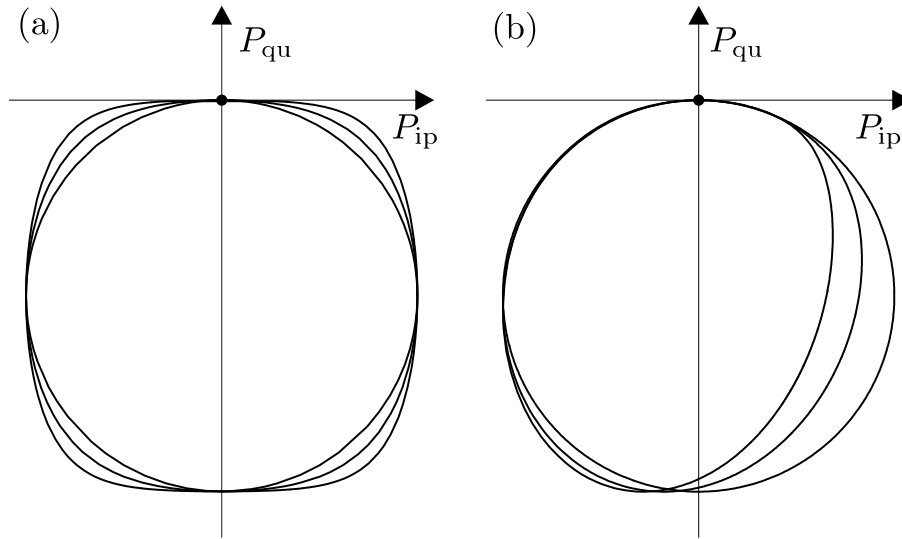


Figure 2.5: Nyquist plots for different magnetic field distributions, each scaled to fit in a square of length 1. Part (a) shows the deviation from circular for constant magnetic field distributions. The innermost trace is for an unperturbed resonance. The two outer traces are calculated for field distribution widths of $x_g = 40 \Gamma_2$ and $400 \Gamma_2$, respectively. Part (b) shows the deviation from circular for linear field distributions. The (outer) circular trace is for an unperturbed resonance. The other two are calculated for distribution widths of $x_g = 5 \Gamma_2$ and $10 \Gamma_2$, respectively.

The main effect of the constant magnetic field distribution is to broaden the resonance, to decrease the amplitude, and to make the line shape differ from a Lorentzian. In the Nyquist plot this is seen by a deformation of the elliptical trace towards a rectangular trace as shown in Fig. 2.5(a). The effect is clearly visible in Fig. 2.5(a) for rather large widths of the magnetic field distribution; in the experiment, however, the effect can be detected for much smaller inhomogeneities due to the large signal/noise ratio.

2.3 Experimental Setup

The magnetometer used for the present study is identical to the reference channel magnetometer of our previous measurements of the human MCG.[11, 12] However, for those measurements the temperature degree of freedom was not optimized and the measurements were carried out at $25^\circ\text{C} - 40^\circ\text{C}$ and at much lower light power than displayed in figure 5.4. The setup (Fig. 5.2) was designed so that a volunteer could be placed under the sensor, with his heart close to the glass cell containing the Cs sample. For moving the volunteer with respect to the sensor—necessary for mapping the heart magnetic field—a bed on a low friction support was used.

The magnetometer sensor head itself was placed in a room with moderate magnetic shielding. The room was $1.7 \times 2.3 \times 2.5 \text{ m}^3$ in volume shielded by a 1 mm

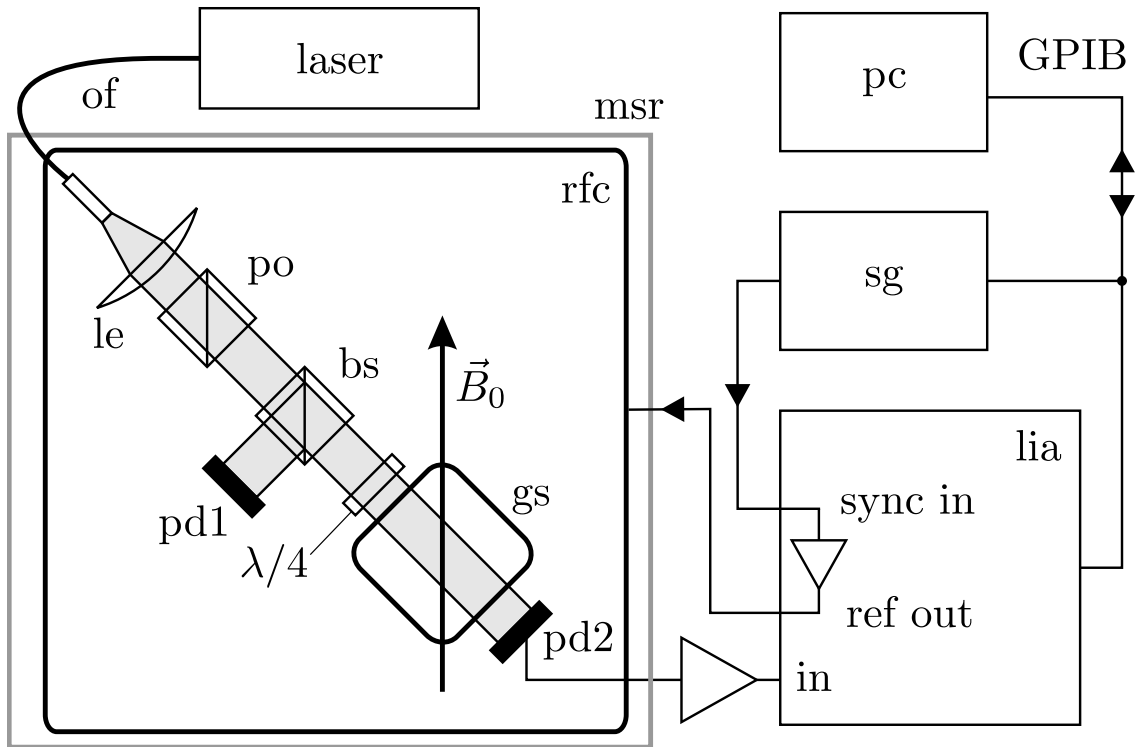


Figure 2.6: Schematic of the experimental setup. Light from the diode laser is delivered via an optical fiber (of) to the experiment in the magnetically shielded room (msr). The light is collimated by a lens (le) and polarized by a polarizing beam splitter cube (po). The beam splitter (bs) reflects 50% of the beam to photodiode 1 (pd1) used for monitoring of the initial light power. The remaining beam passes a quarter-wave plate ($\lambda/4$) providing circular polarized light to the glass cell (gs) that contains the atomic medium. Photodiode 2 (pd2) measures the transmitted light intensity. Its signal is amplified by a current amplifier and fed to the lock-in amplifier (lia). The reference output of the lia drives the radio frequency coils (rfc). The reference frequency of the lia is controlled by a sweep generator (sg). Automatic control and data acquisition is done by a PC via the GPIB bus.

μ -metal layer and an 8 mm copper-coated aluminum layer. For low frequencies, the shielding factor was as low as 5 to 10, whereas 50 Hz interference was suppressed by a factor of 150. Inside the shielded room, surrounding the sensor itself, three coil pairs were placed for the three dimensional control of the magnetic field. In the z -direction (vertical) two round 1 m diameter coils were used. To make room for the patient, the spacing between the coils had to be 62 cm, far away from the Helmholtz optimum of 50 cm. The two coil pairs for the transverse magnetic fields (x and y directions) formed four of the faces of a cube 62 cm on a side. All six coils were driven independently by current sources so that the sum and the difference of the currents in each coil pair could be chosen independently. This allowed us to control not only the magnetic field amplitudes in all three directions, but also the gradients dB_i/di . The field components and gradients were adjusted to produce a homogeneous field of 5 μ T in the z direction.

An extended-cavity diode laser outside the shielded room was used as a light source. The laser frequency was actively stabilized to the $F = 4 \rightarrow F = 3$ transition of the Doppler broadened Cs D₁ line (894 nm) using DAVLL spectroscopy [13] in an auxiliary cell. The light was delivered to the magnetometer sensor proper by a multimode fiber (800 μ m core diameter). After being collimated, the light was circularly polarized by a combination of a polarizing beam-splitter and a multiple-order quarter-wave plate. The circularly polarized light then passed through a glass cell containing the Cs vapor and a buffer gas to prevent the atoms from being depolarized by wall collisions. The cell could be heated to 65° C using hot air which flowed through silicon tubes wrapped around the cell holder. The light power, P , transmitted through the glass cell was detected by a photodiode specially selected to contain no magnetic materials. A current amplifier (FEMTO Messtechnik, model DLPCA-200) converted the photocurrent into a voltage that was fed to the input of the lock-in amplifier. The detection method resulted in a noise level 5 to 20% above the electron shot noise in the photodiode (Fig. 2.7). The digital lock-in amplifier (Stanford Research Systems, model SR830) demodulated the oscillation of P with reference to the applied oscillating magnetic field. That field was generated by two extra windings on each of the B_x coils and was powered by the analog output of the reference function generator contained within the lock-in amplifier. The built-in function generator has the advantage that it delivers a very pure sine wave (phase locked to the synchronization input) and its amplitude can be controlled via the GPIB interface of the lock-in amplifier.

In order to record magnetic resonance lineshapes the lock-in amplifier was synchronized to a reference frequency supplied by a scanning function generator. The data measured by the lock-in (amplitudes of the in-phase and quadrature signals) were transmitted in digital form to a PC, thus avoiding additional noise.

2.4 Optimization

Although the theory of optical magnetometry is well known [4], predictions about the real performance of a magnetometer, especially when it is operating in weakly shielded environments, are difficult to make. The performance depends on laser

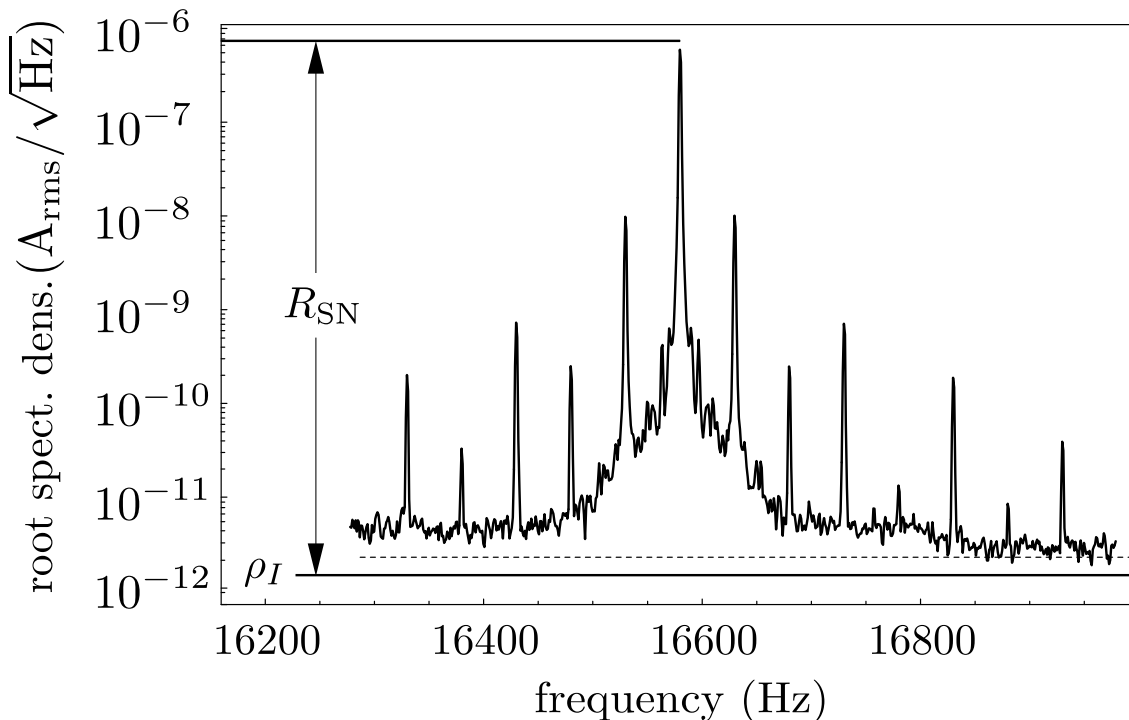


Figure 2.7: Root power spectrum of the photocurrent when the driving field is in resonance with the Larmor frequency. The data sample was recorded at 54° C under conditions optimized for maximum magnetometric sensitivity with a resolution bandwidth of 1 Hz (sampling time 1 s). The amplitude measured by the lock-in amplifier corresponds to the upper horizontal line. The amplitude of the central peak is depressed, since it is slightly broadened by the Hanning window used by the FFT spectrum analyzer (see text). The level ρ_I is the shot-noise level calculated from the DC-photocurrent. The dashed line marks the rms noise measured at 23 kHz. The R_{SN} with respect to the calculated shot-noise level is 5×10^5 . The rms noise is a factor of 1.55 higher than ρ_I resulting in a R_{SN} of 3.2×10^5 .

power, rf power, cell size, laser beam profile, buffer-gas pressure, and the temperature-dependent density of Cs atoms. The size of the cells and the buffer gas pressure were dictated by the available cells: We used 20 mm long cells with 20 mm diameter including 45 mbar Ne and 8 mbar Ar with a saturated Cs vapor. Since the cell is oriented at 45° with respect to \vec{B}_0 , the transverse spatial resolution was 28 mm. The cross section of the laser beam was limited by the 8 mm apertures of the optical components (polarizers and quarter-wave plates).

2.4.1 Intrinsic resolution

Our magnetometer produces a signal which was proportional to the magnetic field changes. The noise of the signal in a perfectly stable field therefore determines the smallest measurable magnetic field change, called the noise equivalent magnetic

field (NEM). The NEM is given by the square root of the power spectral density, ρ_B^2 , of the magnetometer signal, expressed in T/Hz^{1/2}. The rms noise, σ_B , of the magnetometer in a given bandwidth f_{bw} is then

$$\sigma_B = \rho_B \sqrt{f_{\text{bw}}}. \quad (2.16)$$

A straightforward way to measure the intrinsic sensitivity would be to extract the noise level from a sampled magnetometer time series via a Fourier transformation. However, that process requires very good magnetic shielding since the measured noise is the sum of the magnetic field noise and the intrinsic noise of the magnetometer. Many studies under well-shielded conditions have been carried out in our laboratory, leading to the result that optical magnetometers are in principle sensitive enough to measure the magnetic field of the human heart. However, the shielding cylinders used in these investigations were too small to accommodate a person. The present study investigates which level of performance can be obtained in a weakly shielded environment with a volume large enough to perform biomagnetic measurements on adults. In the walk-in shielding chamber available in our laboratory the magnetic noise level was about one order of magnitude larger than the strongest magnetic field generated by the heart. In order to compensate for this the actual cardiomagnetic measurements were done with two magnetometers in a gradiometric configuration [11]. However, the optimal working parameters were determined for a single magnetometer channel only.

Since all time series recorded in this environment are dominated by magnetic field noise, the straightforward way of measuring the intrinsic noise could not be applied. As an alternative approach a lower limit for the intrinsic noise can be calculated using information theory. The so-called Cramér–Rao lower bounds [14] gives a lower limit on how precisely parameters, such as phase or frequency, can be extracted from a signal in the presence of a certain noise level. For the following discussion we assume that the signal is a pure sine wave affected by white noise with a power spectral density of ρ^2 . We define the signal-to-noise ratio R_{SN} as the rms amplitude, A , of the sinusoidal signal divided by the noise amplitude, σ , for the measurement bandwidth, f_{bw} :

$$R_{\text{SN}} = \frac{A}{\sigma} = \frac{A}{\rho \sqrt{f_{\text{bw}}}}. \quad (2.17)$$

Since R_{SN} depends on the bandwidth all numerical values in this publication will be given with respect to unit bandwidth ($f_{\text{bw}} = 1\text{Hz}$).

For a magnetometer generating a Larmor frequency proportional to the magnetic field, Eq. (2.1), the ultimate magnetic sensitivity is limited by the frequency measurement process. The Cramér–Rao lower bound for the variance, V_ω , of the frequency measurement [14] is used (Appendix 2.7) to calculate ρ_B

$$\rho_B = \frac{\sigma_B}{\sqrt{f_{\text{bw}}}} = \frac{4\sqrt{3}\sqrt{f_{\text{bw}}}}{\gamma_F R_{\text{SN}}}. \quad (2.18)$$

For cardiac measurements a bandwidth of $f_{\text{bw}} = 100\text{ Hz}$ is required.[16] This together with a typical value for R_{SN} of 10^4 results in a magnetic field resolution of

315 fT/Hz^{1/2}. In order to be competitive with SQUID-based cardiometers that feature an intrinsic noise of 5...20 fT/Hz^{1/2} this level of performance is not sufficient. For that reason we have concentrated on a different mode of operation where the phase signal is measured by digital lock-in detection.

In this mode of operation ω_{rf} has a fixed value near the Larmor frequency. The information about the magnetic field is obtained from the phase shift of the magnetometer response at that frequency. The Cramér–Rao bound for a phase measurement of a signal with known frequency is used in Appendix 2.8 to calculate the NEM for that case:

$$\rho_B = \frac{\Gamma_2}{\gamma_F R_{\text{SN}} \sqrt{f_{\text{bw}}}}. \quad (2.19)$$

Equations (2.18) and (2.19) define the bandwidth:

$$f_0 = \frac{\Gamma_2}{4\sqrt{3}}, \quad (2.20)$$

for which both approaches yield the same magnetometric sensitivity. For bandwidths larger than f_0 , a phase measurement is more advantageous whereas for bandwidths smaller than f_0 a frequency measurement gives the higher sensitivity.

2.4.2 Bandwidth

In addition to the sensitivity, the bandwidth, i.e., the speed with which the magnetometer signal follows magnetic field changes, is an important feature of a magnetometer. The steady-state solutions of the Bloch equations, P_{qu} and P_{ip} [Eqs. (2.3) and (2.4)], follow small field changes at a characteristic rate Γ_2 , corresponding to a delay time $\tau_{\text{us}} = \Gamma_2^{-1}$. Since the steady state is only reached exponentially, the frequency response is that of a first order low-pass filter [see Fig. 5.1(a)] with a (-3 dB) cut-off frequency f_C given by

$$f_C = \frac{1}{2\pi\tau_S} = \frac{\Gamma_2}{2\pi} = \Delta\nu_2, \quad (2.21)$$

and hence a bandwidth of

$$f_{\text{bw}} = \frac{1}{4\tau_S} = \frac{\Gamma_2}{4} = \frac{\pi}{2} \Delta\nu_2, \quad (2.22)$$

where $\Delta\nu_2$ is the half width of the phase signal measured in Hz.

To achieve maximum sensitivity, atomic magnetometers aim at a maximum τ_S , at the cost of a reduced bandwidth of typically a few tenths of Hz. A large bandwidth can be obtained by increasing the light power since that leads to shorter τ_S and therefore to higher bandwidth. Larger light powers also increase the S/N ratio but the effect can be overcompensated by magnetic resonance broadening, resulting in a degradation of the magnetometric resolution.

Using feedback to stabilize the magnetic resonance conditions is another way to increase the bandwidth. Figure 5.1(c) shows the frequency response of the OPM

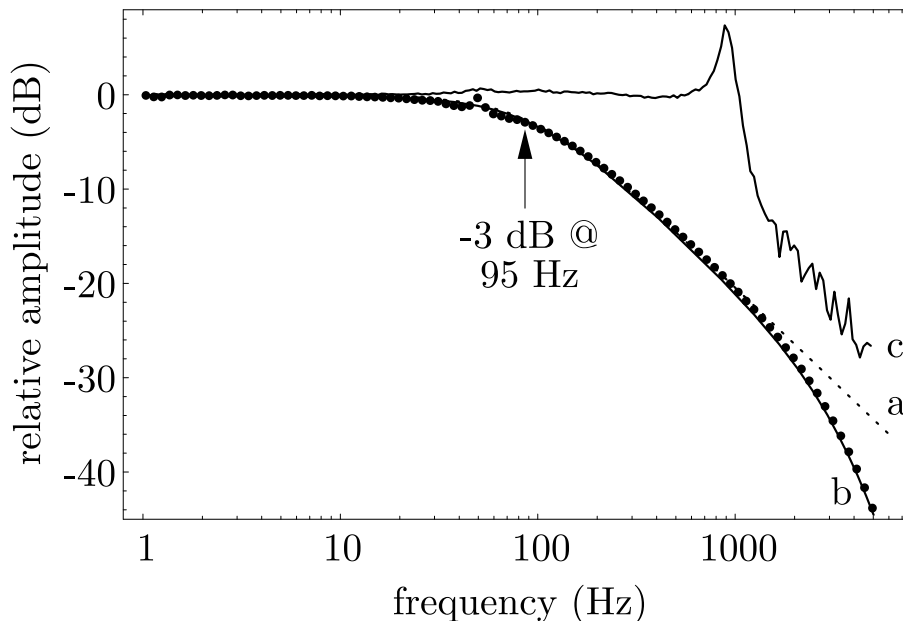


Figure 2.8: Frequency response of the magnetometer, measured by recording the response to an oscillating magnetic field generated by a test coil. The dots show measured points recorded in free running mode under conditions optimized for maximal magnetometric resolution. (a) Calculated first-order low-pass filter corresponding to a spin polarization lifetime of 1.67 ms. (b) Fitted frequency response taking into account (a) and the 4th order low-pass filter of the lock-in amplifier (time constant = 30 μ s). (c) Measured frequency response in the phase-stabilized mode.

in both the free-running (without feedback) mode and in the phase-stabilized mode where the phase signal is used to stabilize ω_{rf} to the Larmor frequency ω_L . For large loop gain the bandwidth is mainly limited by loop delays.

A third method to achieve large bandwidths is the so-called self-oscillating mode. In this mode the oscillating signal measured by the photodiode is not demodulated but rather phase-shifted and fed back to the rf-coils. For a 90° phase shift the system then oscillates at the Larmor frequency. In order to measure the magnetic field, the frequency of this oscillation has to be measured. Magnetic field changes then show up — at least theoretically [4] — as instantaneous frequency changes. In practice, reaction times smaller than a single Larmor period have been observed [15].

Of the three modes outlined above, the latter two both rely on frequency measurements. The self-oscillating magnetometer provides a frequency that has to be measured. The phase-stabilized magnetometer measures the frequency via a reference frequency locked to the Larmor frequency. As a consequence, both methods suffer from the reduced magnetometric resolution predicted by Eq. (2.18). Therefore, we have concentrated on the free-running mode of operation for which the magnetometric resolution is given by Eq. (2.19) and the bandwidth by Eq. (2.22).

Thanks to the rather high light power required for optimal magnetometric res-

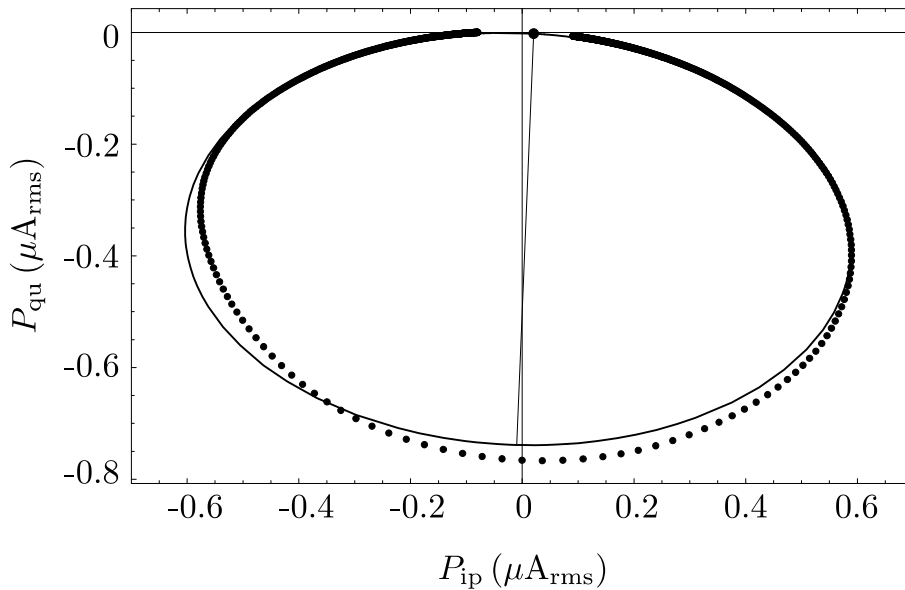


Figure 2.9: The dots represent a Nyquist plot of the magnetic resonance measured under optimized conditions. The solid line is a fit of Eq. (2.15) with added offset and phase rotation to the measured data. The fit model assumes a constant magnetic field distribution. The offset is indicated by the dot close to the origin. The short diameter of the ellipse is drawn in order to illustrate the phase rotation of 2.4° .

olution at higher cell temperatures, the cut-off frequency of the magnetometer was 95 Hz. The bandwidth of the device under these conditions can be extracted from the transfer function (Fig. 5.1(b)) and is about 140 Hz. Because of the time constant of the lock-in amplifier, the measured bandwidth is 10 Hz smaller than the $\pi/2 \times 95$ Hz one would expect for a first order low-pass filter [Eq. (2.22)].

2.4.3 Experimental lineshapes

Figure 2.9 shows a Nyquist plot with experimental data and a model simultaneously fit to the in-phase and quadrature components of the data. The data show a certain asymmetry that can not be reproduced by the model. The Nyquist plots for different magnetic field distributions (Fig. 2.5) suggest that the asymmetry is caused by inhomogeneous magnetic fields. Unfortunately the models discussed in Sec. 2.2.2 do not fit the data correctly, implying that higher-order gradients cause the deformation of the measured lineshape. The fact that the asymmetry is more pronounced for high rf amplitudes indicates that inhomogeneous rf-fields — causing the different parts of the ensemble to contribute with different widths — have to be considered. Unfortunately, models for such inhomogeneities do not lead to analytic line shapes. An empirical model which assumes the measured resonance consists of a sum of several resonances, each at a different position and with a different width, can be fit to the data. The data can be fit perfectly if the number of subresonances is high

enough. However, such fits have a slow convergence and do not provide the needed information about the width and amplitude of the resonance in single fit parameters. For practical reasons (during the optimization more than 2000 spectra were fit) we decided to use the constant magnetic field distribution model for fitting data similar to the ones in Fig. 2.9.

Magnetic field inhomogeneities have much less influence on the shape of the phase signal resulting in more reliable values for Γ_2 . The phase signal represents the speed with which the resonance evolves through the Nyquist plot. Using both the phase signal and the Nyquist plot, the in-phase and quadrature components of the resonance were reconstructed, however, the frequency scaling were given by the phase signal only.

2.4.4 Optimization measurements

For the optimization of the NEM given by Eq. (2.19) the S/N ratio of the lock-in input signal and the linewidth Γ_2 have to be measured. Figure 2.7 shows a frequency spectrum recorded at the input of the lock-in amplifier using a FFT spectrum analyzer. The frequency ω_{rf} was tuned to the center of the magnetic resonance so that the modulation of the photocurrent was at its maximum amplitude. The power spectrum shows a narrow peak at ω_{rf} surrounded by noise peaks that characterize the magnetic field noise. Monochromatic magnetic field fluctuations, e.g., line frequency interference, modulate the phase of the measured sine wave and show up in the power spectrum as sidebands. The low frequency flicker noise of the magnetic field thus generates a continuum of sidebands that sum up to the background structure surrounding the peak in Fig. 2.7. The estimation of the intrinsic sensitivity is based on the assumption that those sidebands would disappear in a perfectly constant magnetic field. The amplitude noise of the signal is mainly due to the electron shot noise in the photodiode, which generates a white noise spectrum. For frequencies which are more than 1 kHz away from the resonance, the noise level drops to the white noise floor. The electron shot noise is the fundamental noise level that can not be avoided. The noise spectral density ρ_I can be calculated from the DC current I_{DC} flowing through the photodiode:

$$\rho_I = \sqrt{2eI_{DC}}. \quad (2.23)$$

At room-temperature the measured rms noise in the spectrum was 5% to 20% above the shot-noise level, depending on induced noise on the photocurrent and the laser frequency stabilization that could cause excess noise in the light intensity. The rms noise rose rapidly for higher temperatures because of the increasing leakage current in the photodiode. Unfortunately, in the experimental setup the photodiodes were in good thermal contact with the Cs cell and, given that the optimal operating temperature of the Cs cells turned out to be in the range of 50° C to 60° C, the photodiode produced an excess noise larger than the shot noise of the photocurrent. Figure 2.7 shows a spectrum recorded under conditions optimized for maximal magnetometric resolution. At 53° C the measured rms noise was higher than the shot noise by a factor of 1.55. However, this limitation can be overcome easily since

the photodiodes do not need to be close to the Cs cell and thus can be operated at room-temperature. In order to avoid the problem of drifting values of ρ during the optimization of ρ_B , the theoretical shot noise level ρ_I was used for ρ in Eq. 2.17 instead of the measured noise.

The amplitude A of the signal can be extracted from the FFT-spectrum by integrating the spectrum over three points ($\pm 1\text{Hz}$) around the center frequency. The procedure was needed since the Hanning window used by the spectrum analyzer to reconstruct the spectrum causes a slight broadening of the central peak. The values calculated in that way are in good agreement with those measured by the lock-in amplifier.

The third parameter needed to calculate the intrinsic sensitivity is the half-width Γ_2 of the magnetic resonance. The value was extracted from a magnetic resonance spectrum recorded by the lock-in amplifier during a frequency sweep of the applied oscillating magnetic field. As discussed in Section 2.4.3 a constant-gradient model was fit to the data in order to extract Γ_2 .

For optimizing in a three-dimensional parameter space, the time for one measurement had to be kept as short as possible. When the lock-in amplifier signal was used as a measure for A [see Eq. (2.17)] and the noise was calculated from the DC current it was not necessary to record a FFT spectrum for each set of parameters of the optimization procedure. In that way the time for a single NEM measurement was reduced to the 20 s sweep time of ω_{rf} plus the time needed to measure the DC current and the temperature of the cell. The measurement was controlled by a PC running dedicated software for recording and fitting the magnetic resonance signals. The amplitude of the rf field, B_{rf} , was changed automatically by the software, resulting in series of typically ten NEMs as a function of B_{rf} . A typical optimization run was made by recording many such series while the system slowly heated up. Repeating those runs for different light powers finally resulted in data for the whole parameter space.

2.5 Results

2.5.1 Dependence on rf amplitude

The first study made with the magnetometer examined the dependence of the magnetic resonance on the rf amplitude B_{rf} measured a series of spectra recorded at room temperature. Figure 2.10 shows the dependence of the magnetic resonance signal width on the rf amplitude measured by the coil voltage U_{rf} . The width of the phase signal (see Fig. 2.10) was fit with a constant, whereas the common width of the in-phase and quadrature components were given by Eq. (2.5). To fit the widths correctly, a constant width had to be added to Eq. (2.5). The additional constant width can be interpreted as a residual broadening caused by magnetic field inhomogeneities of higher order than the one considered in the line fitting model. The Nyquist plot (see Fig. 2.9) shows that higher order gradients are present and the excellent agreement in Fig. 2.10 suggests that they can be treated as an additional broadening.

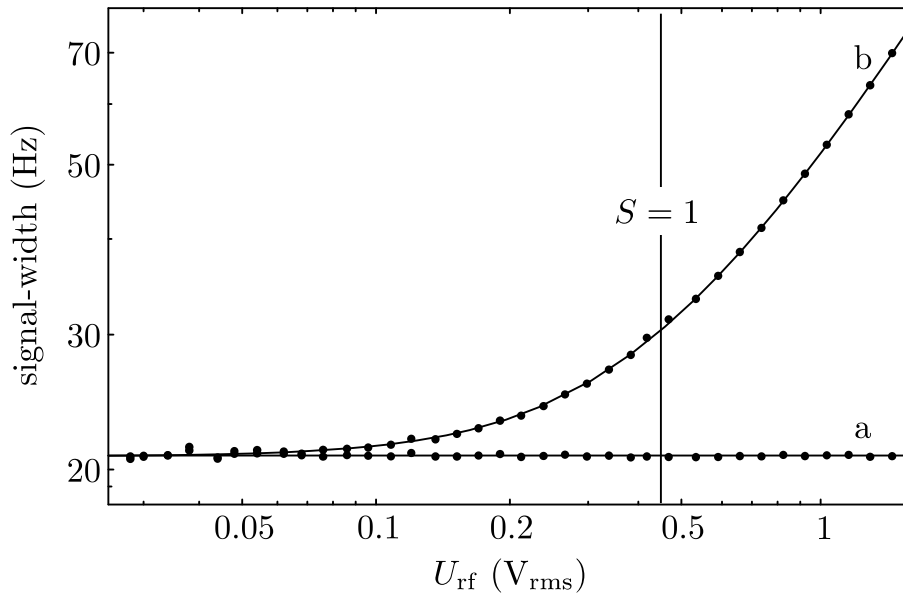


Figure 2.10: Dependence of the magnetic resonance linewidth on the rf amplitude U_{rf} . The points are extracted from measured magnetic resonance spectra by least squares fitting of model Eq. (2.15). The phase signal (a) has a constant linewidth whereas the common widths of the in-phase and quadrature signals (b) increase rapidly with rf amplitude. The solid line represents a model fitted to the data that assumed an additional broadening caused by inhomogeneous magnetic fields.

Figure 2.11 shows the amplitudes of the in-phase and quadrature magnetic resonance signals. The amplitudes were extracted from the same spectra used for Fig. 2.10. The fit model used to explain the amplitudes (solid lines in Fig. 2.11) was based on Eqs. (2.10) and (2.11) with a background proportional to B_{rf} . The origin of the background was an inductive pick up of the \vec{B}_1 field by the photocurrent loop which caused an additional phase-shifted sine wave to be superposed on the photocurrent. As discussed in the theory part (see Fig. 2.4) that lead to an offset in the measured amplitudes of the magnetic resonance signal.

The NEM as a function of rf amplitude is inversely proportional to the quadrature amplitude (a_2 in Fig. 2.11), since the linewidth of the phase signal and the shot noise do not change with rf amplitude. The optimal rf amplitude was determined from the data shown in Fig. 2.11 and corresponds to $S = 1$.

2.5.2 Dependence on temperature and light power

As described in section 2.4.4 the dependence of the NEM on the temperature was recorded while the system was slowly heated. The rf amplitude was automatically scanned so that for every temperature the optimal rf amplitude could be determined. Figure 5.4 shows a contour plot of the NEM as a function of temperature and light power. If the light power is increased, the temperature (and hence Cs atom density)

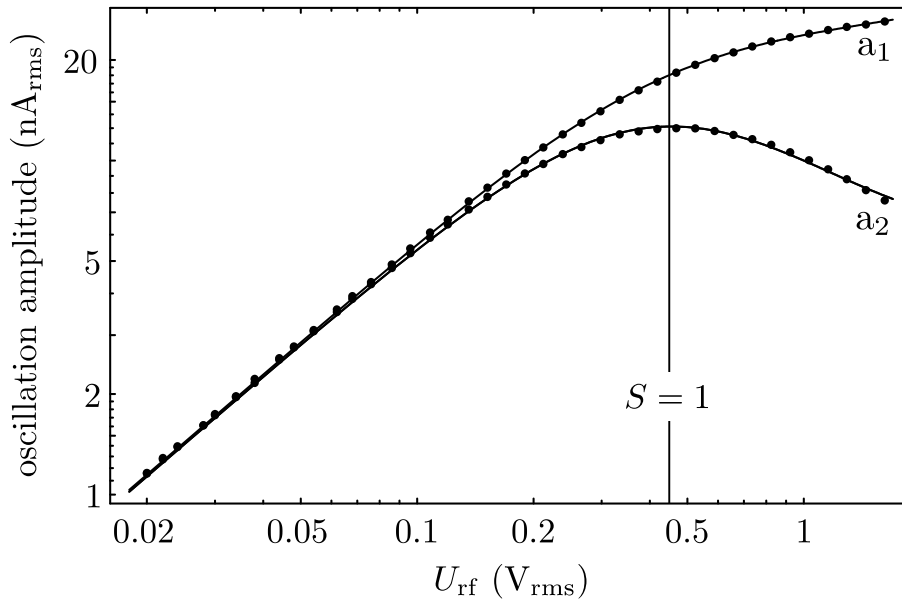


Figure 2.11: Amplitude of the in-phase (a_1) and quadrature (a_2) signals as a function of rf amplitude U_{rf} . The points represent values extracted from measured magnetic resonance spectra. The solid lines show a model fit to the data points (see text). The quadrature amplitude a_2 is equal to the amplitude of the incoming sine wave on resonance ($\delta = 0$).

has also to be increased to maintain optimal resonance conditions. Figure 2.13(b) shows the power transmitted through the cell relative to the incident light power. A relative transmission of 0.37 corresponds to an absorption length which matches the cell length. Taking into account losses at the windows, a density corresponding to 1.4 absorption lengths was found to be optimal.

For each light power the optimal temperature is indicated by a dot in Fig. 5.4. Plotting the NEM along the optimum temperature power curve, i.e., the curve connecting the dots, results in the plot shown in Fig. 2.13(d). For light powers below $15 \mu\text{W}$ and the corresponding temperatures the sensitivity rapidly degrades. The loss in sensitivity is less pronounced if the power and temperature are chosen above the optimum. Values for R_{SN} of up to 500 000 (114 dB) were measured at a resolution bandwidth of 1 Hz.

The optimal magnetic field resolution of our magnetometer is reached at a light power of $15 \mu\text{W}$ and a temperature of 53°C . With that set of parameters, the usable bandwidth of the magnetometer was determined by a cut-off frequency of about 80 Hz (see Fig. 2.13(a)). In order to meet the required 100 Hz bandwidth a slightly larger light power can be used. All characterizing measurements (cf. Figs. 2.2, 5.1, 2.9, and 2.7) were therefore performed with a light power of $20 \mu\text{W}$ at 54°C .

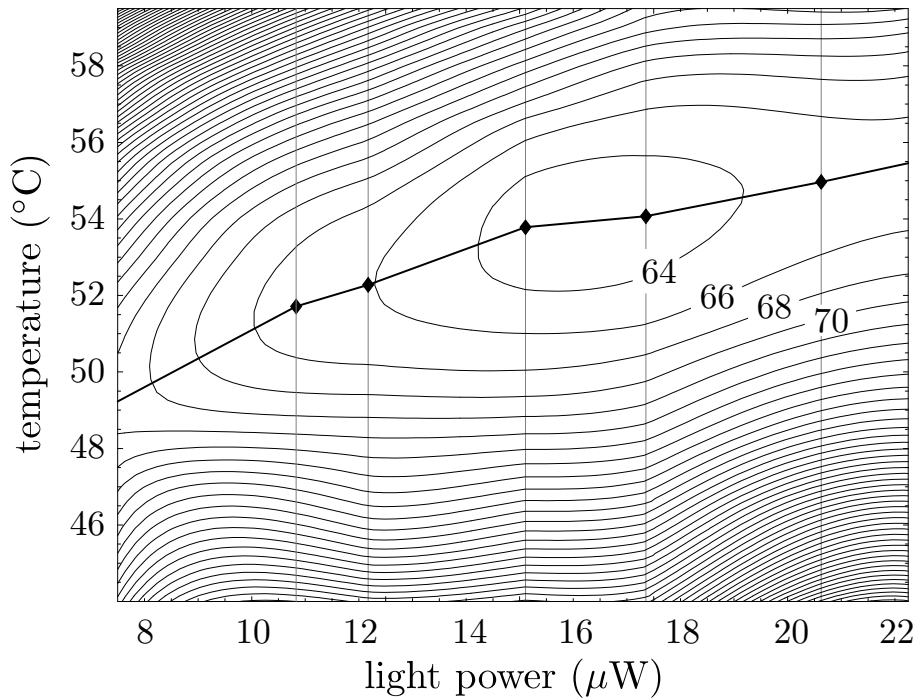


Figure 2.12: Contour plot of the magnetometric resolution (NEM) as a function of temperature and light power. The map is calculated by numeric interpolation from seven optimization runs (indicated by vertical lines). The labels at the contours mark the NEM in $\text{fT}/\text{Hz}^{1/2}$. The points of minimal NEM for each optimization run are indicated by points. The connecting line is a cut along which the data of Fig. 2.13 are obtained. Including the variation of the rf amplitude 970 parameter sets were recorded and analyzed to produce the map.

2.6 Conclusion

Optimizing the performance of the magnetometer has led to a set of parameters for which the device offers a large sensitivity and a large bandwidth. Both requirements can be met at the same time because of rather large linewidths that turned out to be optimal. Under these conditions the high magnetometric sensitivity relies on the achieved very high signal/noise ratios. The system has the potential to operate at a R_{SN} of 500000 (Fig. 2.7) and we hope to be able to demonstrate this once the photodiodes can be removed from the heated Cs cell. However, even using the measured R_{SN} of 320000, the intrinsic sensitivity of $100 \text{ fT}/\text{Hz}^{1/2}$ is good enough for less demanding cardiomagnetic measurements.

The magnetometer bandwidth of 140 Hz in the free-running phase-detecting mode (Fig. 5.1) is high enough for cardiac measurements. The phase-detecting mode avoids the fundamental limitations associated with frequency measurements using short integration times.

An important open experimental question is whether the predicted intrinsic sen-

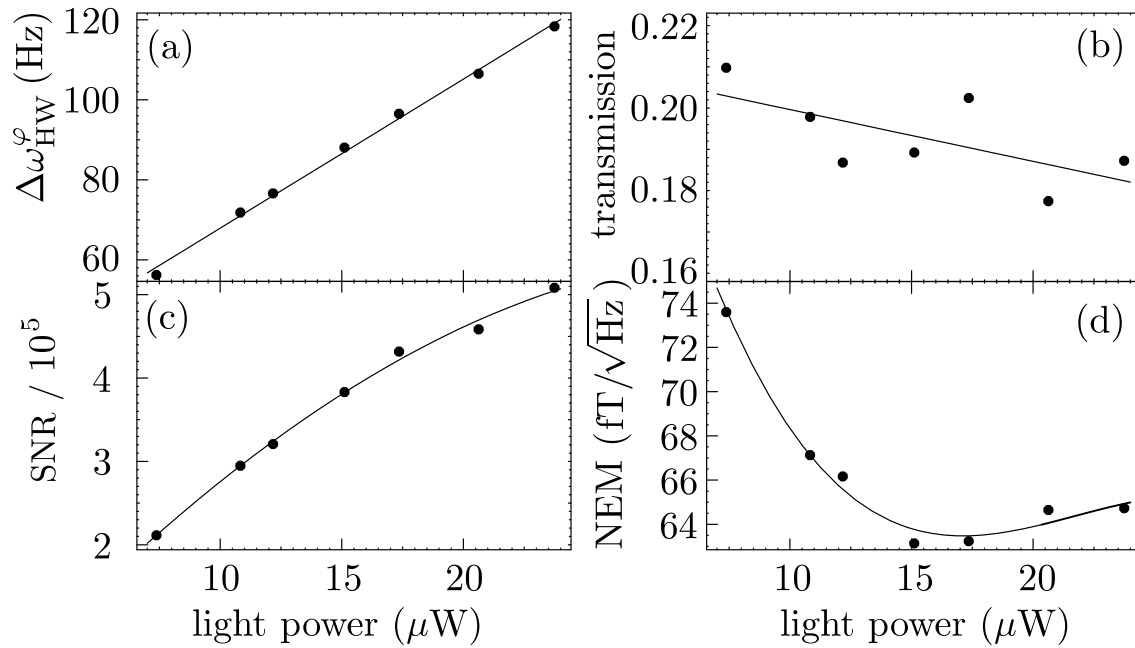


Figure 2.13: Magnetic resonance parameters as a function of incident light power: (a) shows the width of the phase signal that determines the cut-off frequency of the magnetometer bandwidth; (b) shows the DC transmission through the Cs cell relative to the incident light power; (c) is the signal/noise ratio of the lock-in input signal with respect to calculated shot noise; (d) shows the NEM at the points indicated in Fig. 5.4.

sitivity can be reached using several of the present OPMs in a higher order gradiometer geometry. With gradiometric SQUID sensors it is possible to achieve NEM value on the order of $20 \text{ fT/Hz}^{1/2}$ in unshielded environments [16]. In future we plan to use cells with spin-preserving wall coatings rather than buffer-gas cells as sensing elements. Coated cells have the advantage that the atoms traverse the volume many times during the spin coherence lifetime, therefore averaging out field inhomogeneities. We are therefore confident that the present limit from field gradients can be overcome and that optical magnetometers can reach an operation mode limited by their intrinsic sensitivity.

2.7 Appendix A: The Cramér–Rao bound for frequency measuring magnetometers

For the measurement of the frequency ω of a sine wave with a rms amplitude A sampled at $N \gg 1$ points separated by time intervals T_s the Cramér–Rao lower bound for the variance V_ω of ω in the presence of white Gaussian amplitude noise of variance σ^2 is given by [14]:

$$V_\omega = \frac{12\sigma^2}{A^2 T_M^2 N}, \quad (2.24)$$

where $T_M = NT_s$ is the total time interval for one frequency determination. The bandwidth on the input side of the lock-in amplifier is therefore $F_{\text{bw}} = 1/2T_s = N/2T_M$, that at the output is $f_{\text{bw}} = 1/2T_M$. With the definition of the signal-to-noise ratio, Eq. (2.17), V_ω can be expressed independently of the number of samples:

$$V_\omega = \frac{12\rho_i^2 F_{\text{bw}}}{A^2 T_M^2 N} = \frac{6}{R_{\text{SN}}^2 T_M^3}. \quad (2.25)$$

Ideal measuring processes are limited by that condition only. Frequency measurements by a FFT with peak interpolation is a Cramér–Rao bound limited measuring process [14].

From that bound a lower limit for the performance of a frequency measuring magnetometer can be derived. The so-called self-oscillating M_x magnetometer [4] is of this type since it supplies an oscillating signal with a frequency proportional to the magnetic field. With Eq. (2.1) it follows that the root spectral density of the measurement noise ρ_B is given by:

$$\rho_B = \sqrt{\frac{V_B}{f_{\text{bw}}}} = \frac{4\sqrt{3}\sqrt{f_{\text{bw}}}}{\gamma_F R_{\text{SN}}}. \quad (2.26)$$

2.8 Appendix B: The Cramér–Rao bound for phase measuring magnetometers

The Cramér–Rao lower bound for the measurement of the phase of a signal with known frequency is given by [14]:

$$V_\varphi = \frac{\sigma^2}{A^2 N}. \quad (2.27)$$

An example of a measurement process limited only by that condition is the lock-in phase detection where the phase is calculated from the in-phase and quadrature outputs of the lock-in amplifier [see Eq. (2.7)]. In order to calculate the variance V_φ of the phase measurement we assume a white amplitude noise spectrum with a power spectral density ρ^2 :

$$V_\varphi = \frac{\rho^2}{A^2 2T_M}. \quad (2.28)$$

Using this expression and the definition of R_{SN} [Eq. (2.17)], Eq. (2.28) can be written as

$$\sigma_\varphi^2 = V_\varphi = \frac{\rho^2 f_{\text{bw}}}{A^2} = \frac{f_{\text{bw}}}{R_{\text{SN}}^2}. \quad (2.29)$$

From the measured phase φ , the detuning $\delta = \omega_{\text{rf}} - \omega_L$ can be derived. For $\varphi \ll 1$, Eq. (2.7) leads to $\delta \approx \Gamma_2 \varphi$. Using Eq. (2.1), the detuning can be expressed as a magnetic field difference $\Delta B = \delta/\gamma$ which leads, together with Eq. (2.29), to the magnetic field resolution σ_B :

$$\sigma_B = \frac{\sigma_\delta}{\gamma_F} = \frac{\sigma_\varphi \Gamma}{\gamma_F} = \frac{\Gamma \sqrt{f_{\text{bw}}}}{\gamma_F R_{\text{SN}} \sqrt{f_{\text{bw}}}}. \quad (2.30)$$

The root spectral density of the noise in the Δ_B measurement, $\rho_B = \sigma_B/f_{\text{bw}}^{1/2}$, is thus given by:

$$\rho_B = \frac{\Gamma}{\gamma_F R_{\text{SN}} \sqrt{f_{\text{bw}}}}. \quad (2.31)$$

Acknowledgments

This work was supported by grants from the Schweizerischer Nationalfonds and the Deutsche Forschungsgemeinschaft. The authors wish to thank Martin Rebetz for efficient help in understanding the frequency response of the magnetometer and Paul Knowles for useful discussions and a critical reading of the manuscript.

References

- [1] W. Andrä and H. Nowak eds., *Magnetism in Medicine* (Wiley-VCH, Berlin 1998).

-
- [2] J. P. Wikswo, “Biomagnetic sources and their models”, in *Proceedings of the Seventh International Conference on Biomagnetism*, S. J. Williamson, M. Hoke, G. Stroink, and M. Kotani, eds., (Plenum Press, New York-London, 1998), pp. 1–18.
 - [3] D. Cohen, E. A. Edelsack, and J. E. Zimmerman, “Magnetocardiograms taken inside a shielded room with a superconducting point-contact magnetometer,” *Appl. Phys. Lett.* **16**, 278 (1970).
 - [4] A. L. Bloom, “Principles of Operation of the Rubidium Vapor Magnetometer,” *Appl. Opt.* **1**, 61–68 (1962).
 - [5] J. Dupont-Roc, S. Haroche, and C. Cohen-Tannoudji, “Detection of very weak magnetic fields (10⁻⁹ Gauss) by ⁸⁷Rb-zero-field level crossing resonances,” *Phys. Lett.* **28A**, 638 (1969).
 - [6] E. B. Alexandrov and V. A. Bonch-Bruevich, “Optically pumped atomic magnetometers after 3 decades,” *Opt. Eng.* **31(4)**, 711–717 (1992).
 - [7] A. Kastler, “The Hanle Effect and its use for the measurement of very small magnetic fields,” *Nucl. Instr. Meth.* **110**, 259–265 (1973).
 - [8] D. Budker, D. F. Kimball, S. M. Rochester, V. V. Yashchuk, and M. Zolotarev, “Sensitive magnetometry based on nonlinear magneto-optical rotation,” *Phys. Rev. A* **63**, 043403 (2000).
 - [9] M. N. Livanov, A. N. Kozlov, S. E. Sinelnikova, J. A. Kholodov, V. P. Markin, A. M. Gorbach, and A. V. Korinewsky, “Record of the Human Magnetocardiogram by the Quantum Gradiometer with Optical Pumping,” *Adv. Cardiol.* **28**, 78 (1981).
 - [10] S. Kanorsky, S. Lang, S. Lücke, S. Ross, T. Hänsch, and A. Weis, “Millihertz magnetic resonance spectroscopy of Cs atoms in body-centered-cubic ⁴He,” *Phys. Rev. A* **54**, R1010–R1013 (1996).
 - [11] G. Bison, R. Wynands, and A. Weis, “A laser-pumped magnetometer for the mapping of human cardiomagnetic fields,” *Appl. Phys. B* **76**, 325–328 (2003).
 - [12] G. Bison, R. Wynands, and A. Weis, “Dynamical mapping of the human cardiomagnetic field with a room-temperature, laser-optical sensor,” *Optics Express* **11**, 904–909 (2003).
 - [13] K. L. Corwin, Z.-T. Lu, C. F. Hand, R. J. Epstein, and C. E. Wieman, “Frequency-stabilized diode laser with the Zeeman shift in an atomic vapor,” *Appl. Optics* **37(15)**, 3295–3298 (1998).
 - [14] D. C. Rife and R. R. Boorstyn, “Single-Tone Parameter Estimation from Discrete-Time Observations,” *IEEE Transactions on Information Theory* **20(5)**, 591–598 (1974).

- [15] P. Dyal, R. T. J. Jr., and J. C. Giles, "Response of self-oscillating rubidium vapor magnetometers to rapid field changes," *Rev. Sci. Instrum.* **40**(4), 601 (1969).
- [16] I. Tavarozzi, S. Comani, C. D. Gratta, G. L. Romani, S. D. Luzio, D. Brisinda, S. Gallina, M. Zimarino, R. Fenici, and R. D. Caterina, "Magnetocardiography: current status and perspectives. Part I: Physical principals and instrumentation," *Ital. Heart J.* **3**, 75 (2002).

Chapter 3

A laser-pumped magnetometer for the mapping of human cardio-magnetic fields

G. Bison
R. Wynands
A. Weis

Published in Applied Physics B **76**, 325-328, submitted January 8, 2003.

Magnetic fields produced by biological organisms contain valuable information on the underlying physiological processes and their pathologies. Currently, superconducting detectors cooled far below room temperature are required to measure these generally weak biomagnetic signals. We have developed a sensitive laser magnetometer based on optical pumping of cesium atoms that makes it possible to map the magnetic field produced by the beating human heart. A gradiometer formed by two identical sensors greatly reduces the influence of external stray magnetic fields. The magnetometer operates at room temperature and therefore opens the way to affordable and convenient monitoring of biomagnetic fields in research and medical diagnostics.

Magnetometers based on superconducting quantum interference devices (SQUID) currently are the detectors of choice for weak magnetic fields. One important domain of application of SQUID magnetometers is the detection of fields of biological origin [1, 2]. For instance, electric currents in the beating heart not only produce time-varying electric potential differences on the body surface (measurable as the electrocardiogram, ECG) but are also accompanied by a weak magnetic field — measurable as the magnetocardiogram (MCG) [3, 4]. The human heart is the strongest biomagnetic source but still the highest feature in the MCG has an amplitude of less than 100 pT, about 10^{-6} of the geomagnetic field.

The need to use cryogenic cooling liquids and the relatively high cost of SQUID-based devices are the main reasons why such devices are still restricted to research laboratories, although several commercial multichannel SQUID-devices have become available in the past decade. Biomagnetism is a rapidly expanding field of medical research and its community has stressed that the development of alternative, low-cost biomagnetic detectors would constitute an important step towards the wider distribution and acceptance of biomagnetic diagnostics [5]. Although most research in clinical contexts is still in an exploratory phase, several areas have been identified where MCG diagnostics is superior to ECG and similar techniques [6]. There are also practical advantages, for instance the fact that MCG recording is not only a harmless and non-invasive but also a non-contact method.

An alternative technique for biomagnetometry is the use of optically pumped atomic vapors, in which magnetic fields are detected via the induced Larmor precession of a long-lived spin polarization, prepared and detected by optical means [7]. A cardiomagnetometer based on optically pumped vapors was demonstrated by a Soviet team in the 1980's [8, 9], but this research was discontinued. Motivated by the growing interest in (SQUID-based) biomagnetic diagnostics, the need for low-cost alternative detectors, and recent advances in optical magnetometry and in signal denoising techniques we have developed an optically pumped magnetometer (OPM) system that offers sufficient sensitivity, bandwidth, and spatial resolution for the detection of human cardiomagnetic fields. Here we report on the design and performance of this device and demonstrate that it allows us to generate two-dimensional maps of the magnetic field component normal to the torso with a quality that is comparable to SQUID-based maps.

The technique of optical pumping, developed more than half a century ago, is a powerful means for the generation of a high degree of electronic and nuclear spin polarization in dilute atomic vapors. When special precautions are taken to ensure a long lifetime of the sample's spin coherence, any perturbations of this coherence — such as those induced by external magnetic fields — can be detected with extreme sensitivity. Already in the 1960's the ground-state Hanle effect in pumped Rb vapor was employed to detect magnetic field changes in the sub-100 fT range [10]. However, such a Hanle-effect based magnetometer cannot be applied in a straightforward way for biomagnetic diagnostics. This type of device is a vector magnetometer, which is sensitive to a single component of the magnetic field only and it reaches the quoted sensitivity only in extremely homogeneous fields with a stable direction. Moreover, the device used a large sensor cell with a diameter of 6 cm and averaging times of several seconds.

A competitive optically pumped biomagnetometer for MCG recordings has to meet the following requirements. *Sensitivity:* the most pronounced feature in the MCG (the R-peak, inset in Fig. 3.3) has an amplitude of approximately 100 pT, while the less pronounced features (P and T waves, Q and S peaks) are ten or more times smaller. The diagnostic power of the MCG trace depends directly on the quality (signal-to-noise ratio) with which these features and the quiet intervals in between can be recorded. *Spatial resolution:* For the mapping of the MCG signal one needs a spatial resolution of 10-20 mm. *Bandwidth:* in order to provide an

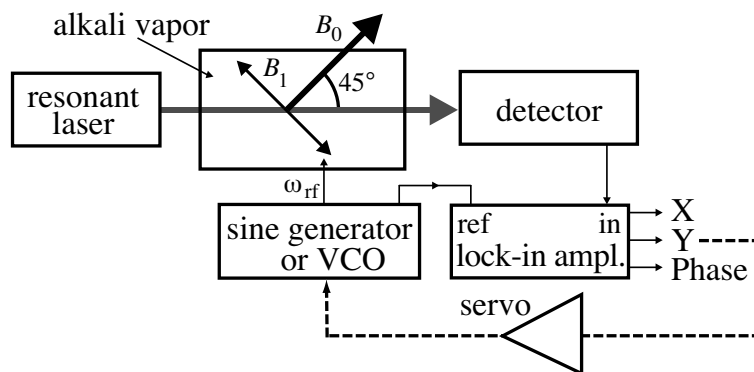


Figure 3.1: Principle of operation of the optically-pumped, phase-locked M_x -magnetometer. For phase-locked operation, the free-running function generator is locked to the Y output signal (dashed line)

undistorted shape of the time-dependent magnetic field the detector has to have a flat response in a frequency range spanning at least DC-40 Hz.

The magnetometer used in the present work is an optical/radio-frequency double resonance device operated in the phase-locked M_x -mode. Its principle of operation is sketched in Fig. 3.1. A resonant circularly polarized laser beam creates spin polarization in the atomic vapor via optical pumping. The corresponding magnetization precesses around the external magnetic field B_0 at the Larmor frequency ω_L . A reference phase is imposed on this continuous creation and precession process by a magnetic field B_1 co-rotating with the spins around the field B_0 at the frequency ω_{rf} . The driven magnetization induces an oscillating component of magnetization on the laser beam axis, which modifies the optical absorption properties of the medium in a periodic way. This oscillation is detected by monitoring the power transmitted through the sample with a photodiode and a lock-in amplifier synchronized to ω_{rf} . Either the in-phase signal (X), the quadrature signal (Y) or the phase $\phi = \arctan(Y/X)$ of the power modulation can be used for magnetometry. All these signals show a resonant behavior when ω_{rf} approaches the Larmor frequency. The Y and ϕ signals are of particular interest because the corresponding line shapes feature a zero-crossing at line center with a steep slope, so that small changes ΔB_0 of the magnetic field result in signal changes that are directly proportional to the field change. The sensitivity of the M_x -magnetometer to external magnetic fields varies as $\sin 2\theta$, where θ is the angle between the laser beam direction and the magnetic field and has thus an optimum sensitivity for $\theta = 45^\circ$. When the Y or ϕ signal is fed back to control ω_{rf} (phase-locked operation) the response bandwidth is no longer limited by the magnetic-resonance linewidth, the same advantage as that of the self-oscillating configuration [11].

The actual magnetometer was realized in the following way. The sensor proper is an evacuated cylindrical glass cell (diameter 20 mm, length 20 mm) filled with a droplet of cesium metal and a buffer gas consisting of a mixture of neon and argon at partial pressures of 4.5 and 0.8 kPa, respectively. This choice of sensor was

determined by availability of a pair of equal cells and corresponds to the optimum parameters for an atomic frequency reference [12] but unfortunately not for a magnetometer. The sensor was heated to 30° by hot air flowing through a coil of plastic tubing surrounding it.

Optical pumping is achieved by light from an extended-cavity semiconductor laser whose frequency was actively locked to the $F = 4$ hyperfine line of the Cs D_1 transition ($\lambda = 894\text{ nm}$) using an auxiliary vapor cell [13]. The laser beam is transported by a multimode fiber to the magnetometer proper, where it is circularly polarized before entering the sensor cell. The power transmitted through the cell is detected by a non-magnetic photodiode placed near the cell. A bias field $B_0 = 5\ \mu\text{T}$ is applied to the sensor at $\theta = 45^\circ$ by a pair of large (100 cm diameter) coils; due to space constraints the distance between the coils had to be 66 cm, much larger than dictated by the Helmholtz condition. The radio-frequency field is applied by a pair of quadratic coils of 62 cm side length and mutual distance. The photocurrent is analyzed by a lock-in amplifier referenced by the radio-frequency ω_{rf} . When operated in this M_x -configuration the device acts as a scalar magnetometer whose signal is a function of $|B_0|$. As the MCG-induced field changes $\Delta\vec{B}$ are much smaller than the offset field \vec{B}_0 applied in the z -direction, the signal changes of the magnetometer will be (to first order) proportional to ΔB_z only [14]; this makes the device act as an effective vector magnetometer.

A major challenge for the recording of extremely small magnetic fields is the need of suppressing oscillating and randomly fluctuating ambient fields (Fig. 3.2), dominant components of which in the present case arise from the AC power line (50 Hz) and a nearby railway line (50 Hz/3). Both passive and active measures were taken to suppress these interfering signals. The measurements were performed in a partially shielded room ($1.7 \times 2.3 \times 2.6\text{ m}^3$) formed by an 8 mm layer of copper-coated pure aluminum and a single 1 mm layer of mu-metal, which suppressed 50-Hz components by a factor of 150. The active suppression was based on a first-order gradiometric arrangement of two identical magnetometers (Fig. 3.3). Due to the rapid decay of the MCG field with distance from the chest and the relatively large homogeneity of ambient fields, the sensor placed near the chest responds to MCG and ambient fields, while the second sensor responds mainly to ambient fields, so that the signal of interest can be extracted as the difference signal. This was realized as follows in practice: The distant magnetometer was operated in a phase-locked mode, by controlling the radio frequency ω_{rf} (which is common to both sensor cells). The servo loop thus ensures that the instantaneous Larmor precession frequency of the atomic moments is always in resonance with the driving frequency ω_{rf} at the position of the distant sensor; simultaneously it corrects the background fluctuations for the sensor near the chest, provided the ambient field and the correction field are both homogeneous. In this way line-frequency interference in the MCG sensor could be reduced by an additional factor of 150, which is sufficient to facilitate the direct visualization of the MCG signals on an oscilloscope. This factor is limited by the inhomogeneity of the stray fields.

The intrinsic sensitivity of our M_x -OPM cannot be obtained from the noise level in the time traces because this noise is dominated by the temporal instability of

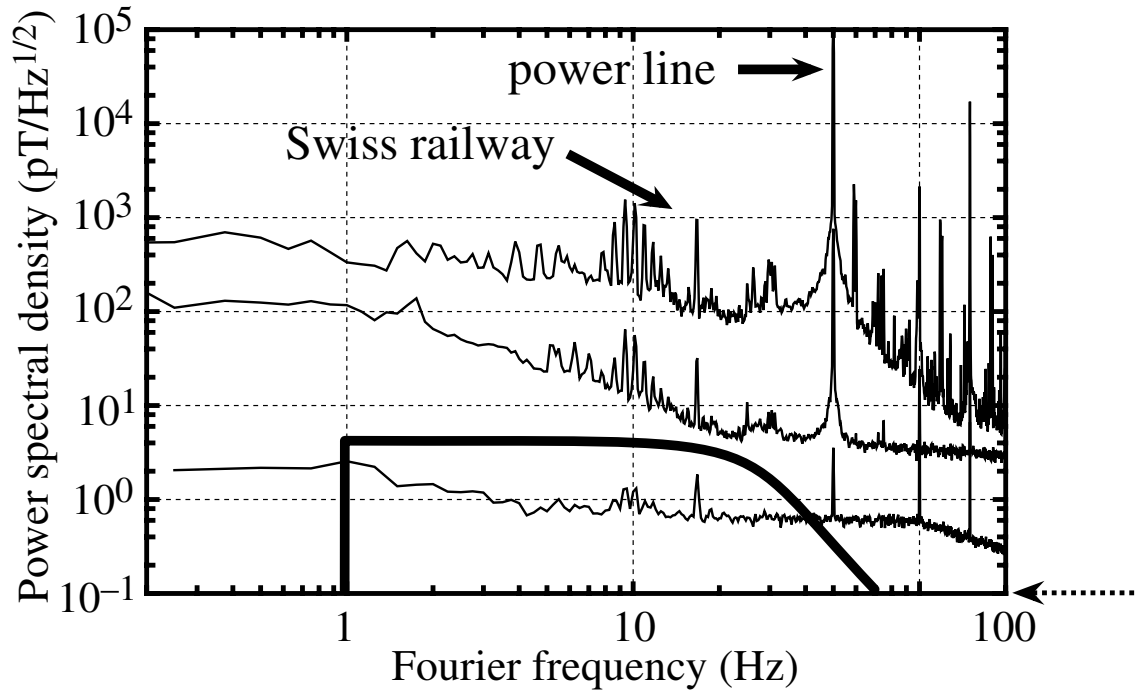


Figure 3.2: Power spectral density of magnetic noise sources and signals. Top trace: laboratory noise. Middle trace: noise inside the shielded room. Bottom trace: noise of the gradiometer signal. The smooth line is the envelope of the power spectrum of an idealized MCG signal. The dotted arrow indicates the intrinsic noise level of a single channel

the magnetic stray fields. Instead, we measured the power spectrum of the input signal of the lock-in amplifier. It has a very simple shape: above 1 kHz it features a flat background with a narrow peak at $\omega_{\text{rf}}/2\pi$. The background is typically 5-10% above the shot-noise level computed from the DC value of the photocurrent of the photodiode. The ratio of the peak amplitude and the background level gives the signal-to-noise ratio of the detection and hence the intrinsic sensitivity.

After a first round of optimizations with respect to radio-frequency and laser power, one obtains an intrinsic sensitivity level of $99 \text{ fT}/\sqrt{\text{Hz}}$, which already now compares favorably with typical noise levels of high- T_c SQUID systems ($10 \dots 100 \text{ fT}/\sqrt{\text{Hz}}$). This sensitivity is definitively sufficient for the recording of the human MCG.

Figure 3.4a shows an example of the MCG data of one of the authors, recorded with a sample rate of 200 Hz. The main noise component on the signal are still oscillations at 50 Hz and harmonics thereof. The MCG clearly exhibits the typical features, i.e., the QRS complex as well as the T waves (see inset in Fig. 3.3). When a sophisticated denoising algorithm based on state-space analysis [15] is applied to the data the curve represented in Fig. 3.4b is obtained [16], comparable in quality to similarly denoised SQUID data.

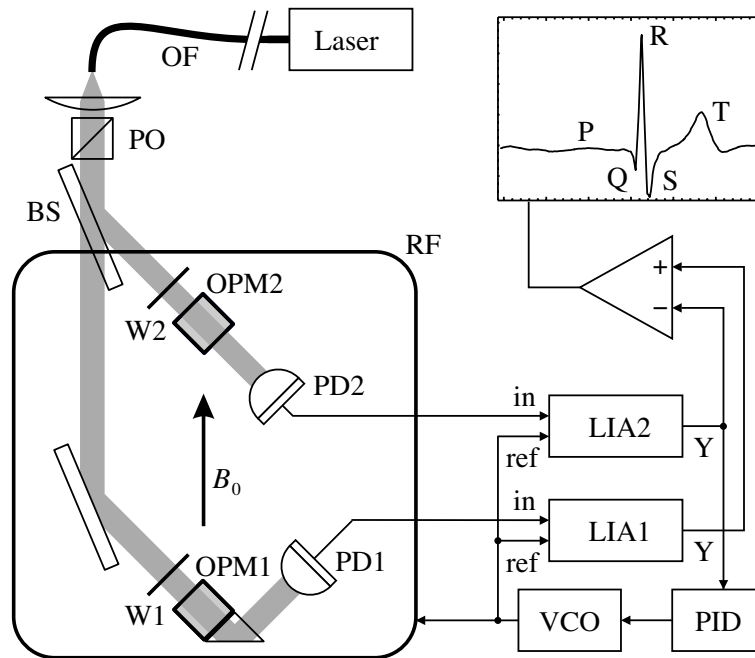


Figure 3.3: Setup of the first-order OPM gradiometer and the measurement electronics (not to scale). Optical and electronic components: optical fiber (OF), polarizer (PO), beam splitter (BS), quarter-wave plates (W1, W2), photodiodes (PD1, PD2), cesium vapor cells (OPM1, OPM2), lock-in amplifiers (LIA1, LIA2), servo amplifier (PID), voltage-controlled oscillator (VCO). INSET: Conventional labelling of characteristic MCG features

One of the advantages of MCG diagnostics over conventional ECG diagnostics is the fact that the former allows one to record the spatial dependence of the signal, thereby offering the possibility to localize specific heart conditions; reconstruction of the underlying current distribution is possible with higher resolution than in the case of multi-lead ECG recording (body surface-potential mapping) [6]. In order to demonstrate the capability of our system for such recordings we have designed a non-magnetic movable table that allows positioning the subject at well-defined positions with respect to the sensor. By recording ten-second MCG time series at each of 6×6 grid points (separated by 40 mm) above the chest a two-dimensional map of the B_z -component of the MCG field of a subject is obtained. Such a mapping takes about 35 minutes. Average amplitudes of the R-peak were inferred from each time series by visual inspection and a two-dimensional interpolation algorithm was applied to obtain an iso-field map such as the one shown in Fig. 3.5. It is to be noted that this map is of similar quality as the maps generated by (multi-channel) SQUID devices. However, because of the very crude signal analysis used to construct the map its diagnostic value has to be treated with caution. Our main goal was merely to demonstrate that the present technique allows mapping with good statistical quality.

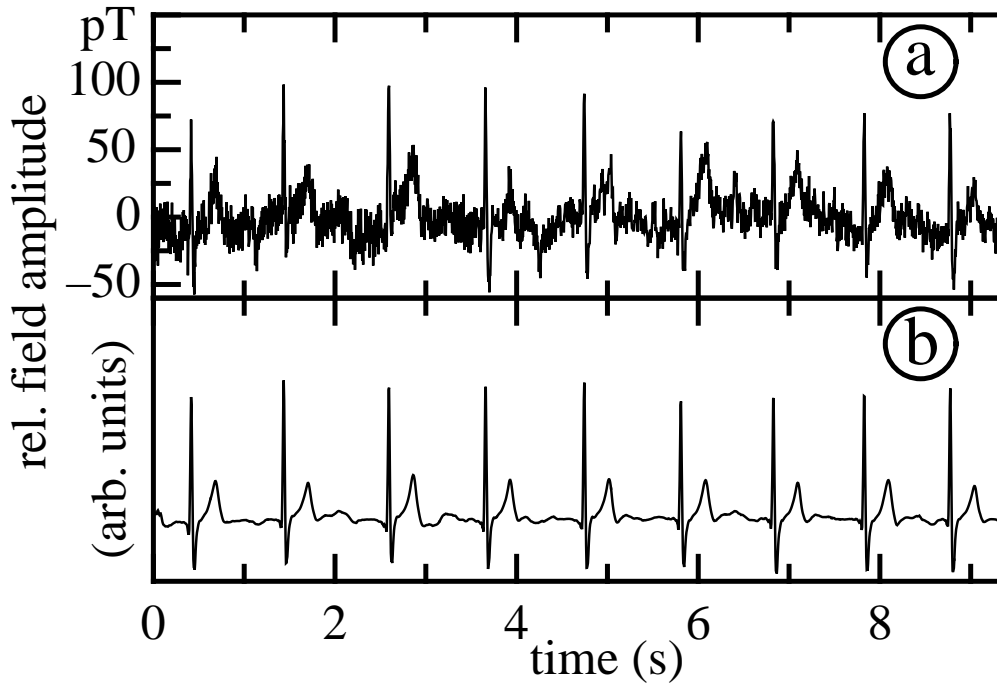


Figure 3.4: Time series of the magnetocardiogram of one of the authors. **(a)** Output data of the gradiometer. **(b)** The data filtered with a state-of-the-art denoising algorithm [15, 16]

In conclusion we can state that – although intrinsically less sensitive than SQUID detectors – optically pumped magnetometers can be used to record two-dimensional maps of human cardiomagnetic signals. The fact that OPMs are less expensive by more than one order of magnitude than SQUID detectors and that their operation is practically maintenance- and cost-free should contribute substantially to a broader acceptance of magnetocardiography as a diagnostic tool. The next experimental step will be the generation of maps also for other times during the cardiac cycle, for instance in the form of a movie. This will require averaging over several heart beats in order to improve the signal-to-noise ratio. Future developments in our laboratory will aim at enhancing the sensitivity of the device by optimization of system parameters such as buffer gas pressure, cell temperature and field inhomogeneity, improving the gradiometric suppression in order to operate the device in an unshielded environment, developing and applying denoising algorithms, and designing multi-channel devices.

This work was supported by grants from the Schweizerischer Nationalfonds and the Deutsche Forschungsgemeinschaft. The authors thank U. Bischler for efficient help with the recording of mapping data.

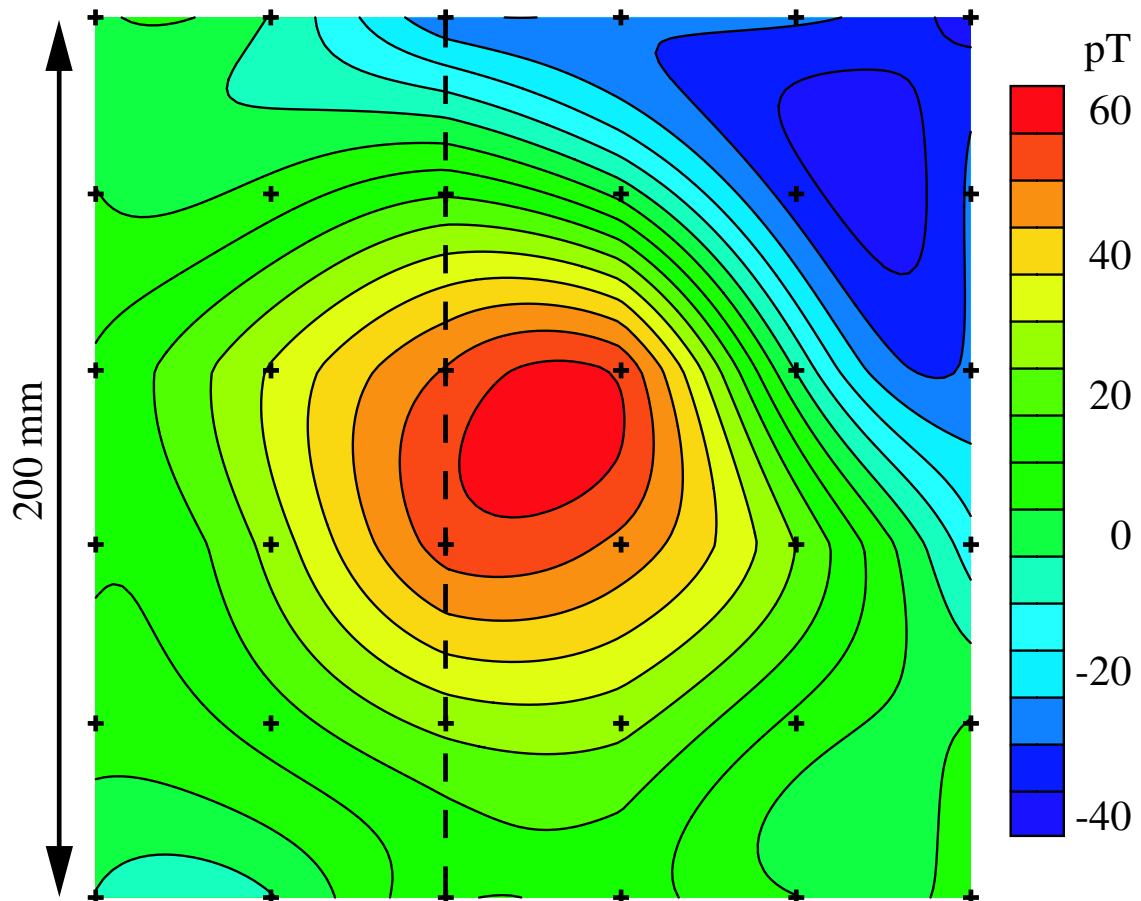


Figure 3.5: Map of the R-peak amplitude of one of the authors as a function of position above the chest. Data was taken at the points indicated by the crosses. The dotted line indicates the position of the sternum

References

- [1] W. Andrä, H. Nowak (eds.), *Magnetism in Medicine*, (Wiley-VCH, Berlin 1998).
- [2] Yu. A. Kholodov, A. N. Kozlov, A. M. Gorbach, *Magnetic fields of biological objects* (Nauka Publisher, Moscow 1990).
- [3] G. M. Baule, R. McFee: *Am. Heart J.* **66**, 95 (1963).
- [4] D. Cohen, E. A. Edelsack, J. E. Zimmerman: *Appl. Phys. Lett.* **16**, 278 (1970).
- [5] I. Tavarozzi, S. Comani, C. Del Gratta, G. L. Romani, S. Di Luzio, D. Brisinda, S. Gallina, M. Zimarino, R. Fenici, R. De Caterina: *Ital. Heart J.* **3**, 75 (2002).
- [6] I. Tavarozzi, S. Comani, C. Del Gratta, S. Di Luzio, G. L. Romani, S. Gallina, M. Zimarino, D. Brisinda, R. Fenici, R. De Caterina: *Ital. Heart J.* **3**, 151 (2002).
- [7] E. B. Alexandrov, V. A. Bonch-Bruevich, N. N. Yakobson: *Sov. J. Opt. Technol.* **60**, 754 (1993).
- [8] M. N. Livanov, A. N. Kozlov, S. E. Sinelnikova, Ju. A. Kholodov, V. P. Markin, A. M. Gorbach, A. V. Korinewsky: *Adv. Cardiol.* **28**, 78 (1981).
- [9] I. O. Fomin, S. E. Sinelnikova, A. N. Koslov, V. N. Uranov, V. A. Gorshkov: *Kardiologija* **23**, 66 (1983).
- [10] C. Cohen-Tannoudji, J. Dupont-Roc, S. Haroche, F. Laloë: *Phys. Rev. Lett.* **22**, 758 (1969).
- [11] A. L. Bloom: *Appl. Opt.* **1**, 61 (1962).
- [12] S. Knappe, R. Wynands, J. Kitching, L. Hollberg: *J. Opt. Soc. B* **18**, 1545 (2001).
- [13] K. L. Corwin, Z.-T. Lu, C. F. Hand, R. J. Epstein, C. E. Wieman: *Appl. Opt.* **37**, 3295 (1998).
- [14] C. Affolderbach, M. Stähler, S. Knappe, R. Wynands: *Appl. Phys. B* **75**, 605 (2002).
- [15] K. Sternickel, A. Effern, K. Lehnertz, T. Schreiber, P. David: *Phys. Rev. E* **63**, 036209 (2001).
- [16] Denoising performed courtesy of K. Sternickel (CardioMag Imaging, Inc., Schenectady, USA).

Chapter 4

Dynamical mapping of the human cardiomagnetic field with a room-temperature, laser-optical sensor

G. Bison
R. Wynands
A. Weis

Published in Optics Express **11(8)**, 904-909, submitted February 11, 2003.

The magnetic field produced by the human heart carries valuable information for medical research, as well as for diagnostics and screening for disease. We have developed an optical method that allows us to produce movies of the temporal dynamics of the human cardiomagnetic field map. While such movies have been generated before with the help of SQUID magnetometers, our technique operates at room temperature and promises substantial economic advantages.

4.1 Introduction

The study of biologically generated magnetic fields basically started in 1963, when the magnetic field generated by the human heart was detected for the first time [1]. At the time, a large induction coil was used, while since the 1970ies superconducting quantum-interference devices (SQUIDs) have been the detectors of choice for biomagnetic fields [2]. Although such SQUID detectors are expensive to buy and operate, a quite active research community has sprung up around biomagnetism, with major areas of interest being the magnetic fields of the human heart (magneto-cardiography, MCG) [5] and brain (magnetoencephalography, MEG) [3, 4].

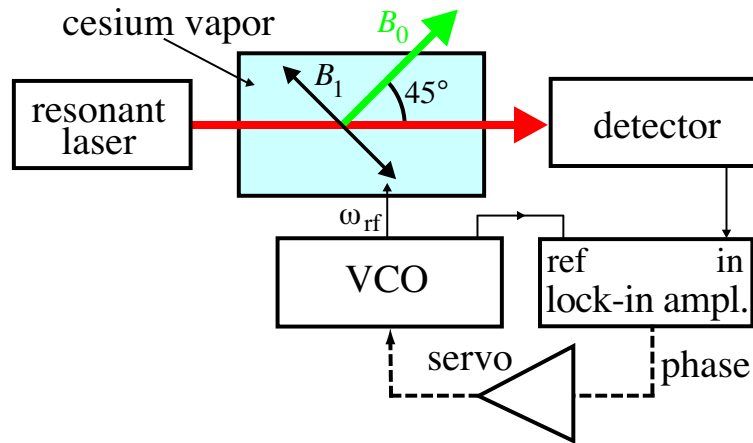


Figure 4.1: Schematic setup of the optically-pumped M_x -magnetometer in the phase-locked mode. The voltage-controlled oscillator (VCO) is locked to the phase signal (dashed line)

Our main interest lies in the development of new techniques for sensitive optical magnetometry. We have concentrated on the magnetic field generated by the human heart because this is one of the strongest biomagnetic signals and therefore an obvious first target. Still, with a maximum amplitude of 100 pT the human MCG is extremely weak, about 10^{-6} of the geomagnetic field and orders of magnitude weaker than typical stray fields in a normal environment. From the point of view of medical applications, a map of the cardiomagnetic field, taken during suitable intervals of the cardiac cycle, can help to detect pathological changes in the heart and its function. While biomagnetic diagnostics is still mostly an area of research and exploration, a recent review by cardiologists identifies various circumstances where the technique has great value [6]. In a related review [5], the same authors describe the instrumentation available for biomagnetic research to-date, stating that more convenient detectors will be needed before biomagnetic diagnostics can realize its full potential.

We believe that we can provide such a technique in the form of a newly developed laser-pumped cesium vapor magnetometer in a gradiometer configuration. As a demonstration of the technical feasibility and the future potential of our technique we have mapped the human cardiomagnetic field outside the chest with a time resolution of milliseconds and a spatial resolution of a few centimeters, typical of biomagnetic requirements.

4.2 Experimental method and setup

The magnetometer we developed for the present work is an optical/radio-frequency double resonance device operated in the phase-locked M_x -mode (Fig. 4.1) [7]. A resonant circularly polarized laser beam from an extended-cavity diode laser ($\lambda = 894$ nm) optically pumps and thereby spin-polarizes a thermal vapor of cesium

atoms, which is contained in a glass cell (2 cm long, 2 cm diameter) together with a buffer gas. The Larmor precession of the corresponding atomic magnetization around a bias field of $B_0 = 5 \mu\text{T}$, subtending an angle of 45° with respect to the laser beam direction, is resonantly driven by a radio-frequency (rf) field B_1 at right angle to \vec{B}_0 . Due to this precession the optical transmission of the vapor changes periodically, in step (but not necessarily in phase) with the magnitude of the component of the magnetization along the laser beam direction. The modulation of the transmitted light power at the Larmor precession frequency is detected with a non-magnetic photodiode placed behind the vapor cell and demodulated with a lock-in amplifier synchronized to the rf. The phase of the response exhibits a steep linear slope at line center, so that a small change ΔB_0 of the magnetic field results in a signal change that is directly proportional to the field change. When the output signal is fed back to control the driving rf frequency (phase-locked operation, dashed line in Fig. 4.1) the response bandwidth of the magnetometer is no longer limited by the magnetic-resonance linewidth, the same advantage as that of the self-oscillating configuration [7]. This is important because a response bandwidth of at least DC-40 Hz is required for a useful interpretation of cardiomagnetic signals.

When operated in this M_x -configuration the device acts as a scalar magnetometer whose signal is a function of $|\vec{B}_0|$. As the MCG-induced field changes $\Delta \vec{B}$ are much smaller than the offset field \vec{B}_0 applied in the z -direction, the signal changes of the magnetometer will be (to first order) proportional to ΔB_z only [8].

Since the biomagnetic fields are so weak, great care must be taken to reduce the influence of external stray fields, for instance line-frequency noise or that from electrical machinery in the vicinity. In this first demonstration setup, we have operated the device inside a partially shielded room, where line-frequency interference is reduced about 150-fold, to about 0.4 nT rms (root-mean-square) amplitude.

The required further reduction is achieved by an optical gradiometer [8]. Since the cardiomagnetic field decays rapidly with distance from the chest, while stray fields are rather homogeneous by comparison, a sensor placed near the chest detects both cardiomagnetic and ambient fields, while a second sensor 7 cm away responds mainly to ambient fields. The difference signal, which is free of the homogeneous component of the stray fields, is formed as follows. The distant magnetometer is operated in a phase-locked mode, by controlling the common radio frequency for both cells. This servo loop ensures that the instantaneous Larmor precession frequency of the atomic moments at the position of the distant sensor is always in resonance with the driving frequency; because of the common rf, homogeneous background fluctuations are corrected for in the sensor near the chest.

In this way, line-frequency interference in the MCG sensor can be reduced by about another two orders of magnitude, which is then sufficient to facilitate the direct visualization of the MCG on an oscilloscope. This additional noise reduction is limited by fluctuations of inhomogeneous stray fields, which are not compensated by the first-order gradiometer. The overall compensation will be improved in a future design using higher-order gradiometers, as has been demonstrated for SQUID magnetometry [3].

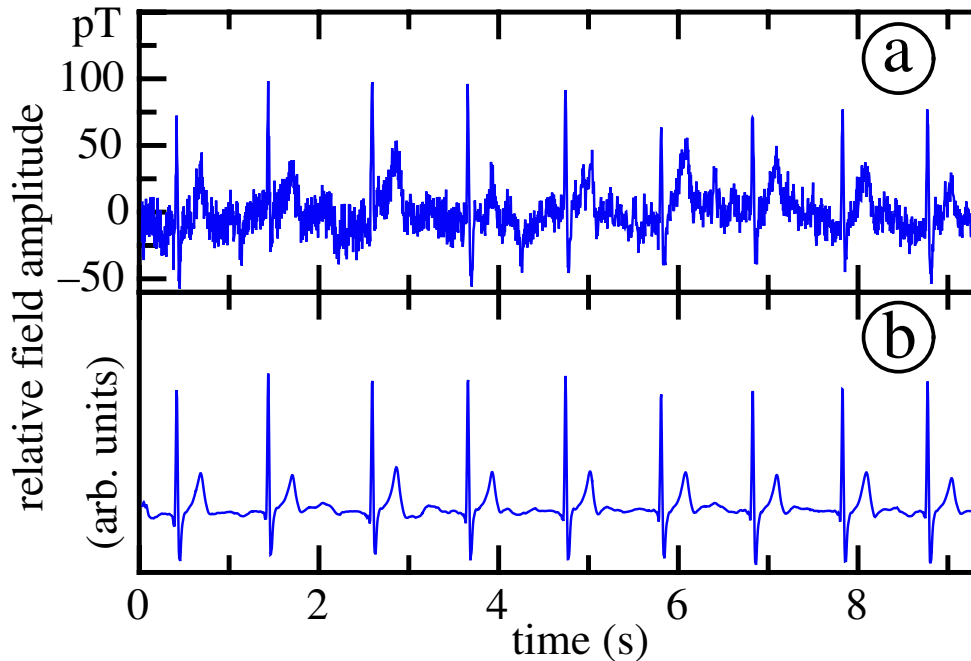


Figure 4.2: Time series of the magnetocardiogram of one of the authors. (a) Output data of the gradiometer. (b) The data filtered with a state-of-the-art denoising algorithm [10, 11]. This filtering procedure was not employed for any of the other results in this report.

4.3 Results

Detection noise at the input of the lock-in amplifier is typically about 5–10% above shot noise, giving an intrinsic sensitivity of $100 \text{ fT}/\sqrt{\text{Hz}}$, which is in the range of high- T_c SQUIDs for biomedical applications.

The MCG data (Figure 4.2a) obtained with an early version of this optical gradiometer allows one to distinguish the typical features, i.e., the QRS complex as well as the T wave (see inset in Fig. 4.2). This data is comparable in quality to earlier attempts at optical biomagnetometry [12, 13], work that comprised taking isolated MCG traces and that was soon discontinued (as far as we know). Our unfiltered and unaveraged data is already good enough to produce spatially resolved maps of the cardiomagnetic field for those instances of the cardiac cycle where the field is particularly strong, like the R peak [9] (for the conventional labelling of ECG and MCG features see Fig. 4.3). When for illustration purposes a sophisticated denoising algorithm based on state-space analysis [10] is applied to the data the curve represented in Fig. 4.2b is obtained [11], comparable in quality to similarly denoised SQUID data. This filtering procedure was not employed for any of the other results in this report.

In order to obtain maps also for other instances during the heart cycle it is necessary to improve the signal quality, for example by averaging over several cycles.

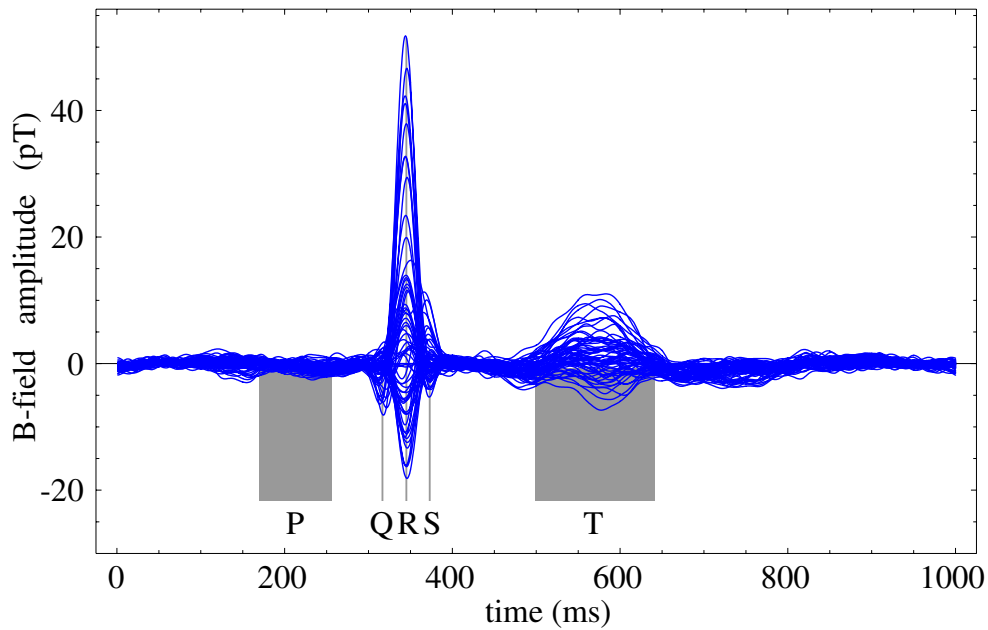


Figure 4.3: All 63 MCGs (each averaged over 100-120 beats) taken on the grid above the chest, plotted together in order to show the range of signal amplitudes and shapes. The characteristic MCG features are by convention designated by the letters P, Q, R, S, and T.

Since even at rest the heart beat is not perfectly regular one needs a way to trigger the signal. A simple 3-lead ECG-device was used for this purpose. Non-magnetic electrodes were connected to the left and right wrist of the subject, with a reference electrode connected to the left ankle.

Then 63 pairs of time series (100s long) of the gradiometer signal and the ECG trace were recorded on a 8×8 grid of points over the chest separated by 4 cm each (one corner point could not be accessed due to geometrical constraints in our current setup). For each of those pairs, the positions of the local maxima of the second derivative of the ECG trace (i.e., the centers of the R peaks) were used in an off-line data treatment to identify the exact position of each beat. The MCG traces were then cut into (potentially overlapping) segments of 1000 data points (corresponding to 1 s of data) such that the R peak was at index 333 in each of the segments. Finally, the data points with the same index were averaged. It should be noted that the same triggering and averaging procedure is also necessary for SQUID-generated data. In Fig. 4.3, all 63 averaged MCGs are plotted on top of each other, thus showing the overall range and shape of the MCG signals.

Data of this quality is good enough to document the dynamics of the cardio-magnetic field distribution in two dimensions. An intuitive way of presenting that information is to produce an iso-field map for each of the 1000 sample times and string them together into a movie of the spatio-temporal dynamics of the cardio-magnetic field. In order to get an impression of the quality of and the information provided by such a movie, we show three frames in Fig. 4.4, taken from the movies

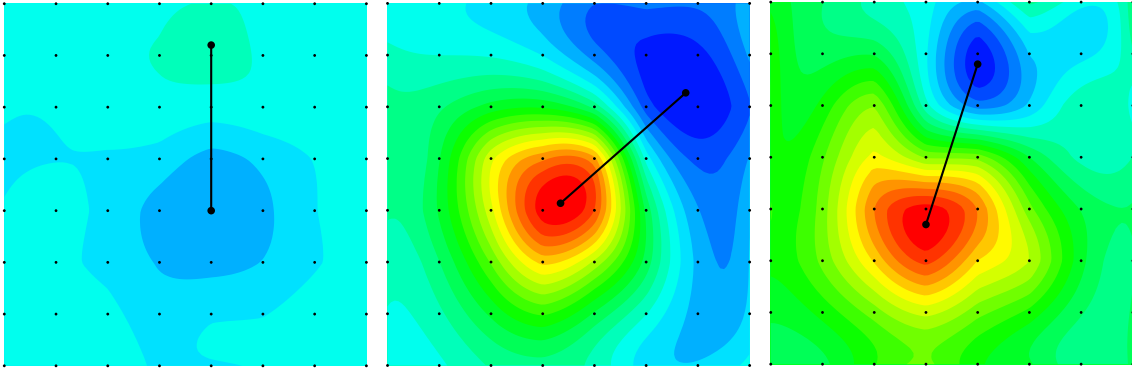


Figure 4.4: (QRS dynamics, [QuickTime Movie \(1.5 MB\)](#); T dynamics [QuickTime Movie \(2.4 MB\)](#)) Selected video frames taken from the movies accompanying this publication. The red area corresponds to maximum field pointing towards the chest (maximum ΔB_z), blue to the strongest field emerging from the chest (minimum ΔB_z). Within each movie, all frames have the same color scale and are oriented such that the top right corner corresponds to the grid point closest to the left shoulder. The black line connects the local maximum and minimum in each frame. LEFT: Field distribution at the Q dip. CENTER: Field distribution at the R peak. RIGHT: Field distribution at the crest of the T wave (different color scale).

accompanying this publication. The movies itself cover, respectively, the region of the QRS complex, where the strongest signals are encountered, and of the T wave, a region of particular interest for cardiologists [14]. In the eye of a physicist, the field distributions look approximately like they were being produced by an effective current flowing along a finite-sized line segment oriented perpendicularly to the line connecting the field maximum and the field minimum in each frame. For the T-interval the angular orientation of this current has shown diagnostic value [14] superior to that from ECGs at rest for the detection of coronary arterial diseases. The angles obtained with our setup for our test subject (Fig. 4.5) are compatible with those obtained with SQUIDs for healthy persons [14].

4.4 Conclusion

Although intrinsically less sensitive than SQUID detectors, laser-pumped magnetometers can be used to record two-dimensional maps of human cardiomagnetic signals: the main problem is not sensitivity but noise suppression. The fact that OPMs are less expensive by more than one order of magnitude than SQUID detectors and that their operation is practically maintenance- and cost-free should contribute substantially to a broader acceptance of magnetocardiography as a diagnostic tool. We envision that, once cardiomagnetometry has found its place in medical routine, the standard sensors will not be SQUIDs but rather laser-pumped OPMs.

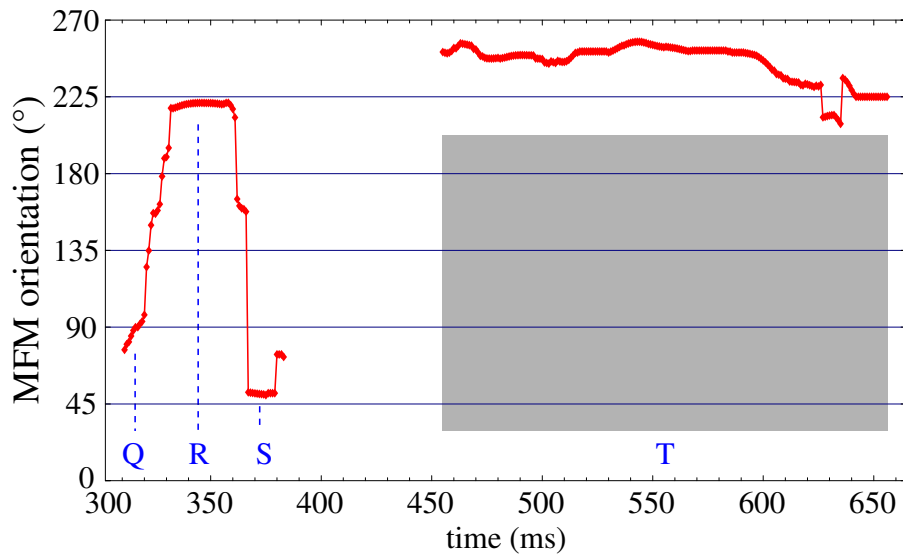


Figure 4.5: Orientation of the line pointing from the local field minimum to the local field maximum, called the magnetic-field-map (MFM) orientation in [14]. Angles are shown only for those time intervals where both field minimum and maximum clearly stand out against the noise level. An angle of 0° corresponds to a line pointing towards the right of the frame, with angles increasing in the counter-clockwise direction.

Acknowledgements

This work was supported by grants from the Schweizerischer Nationalfonds and the Deutsche Forschungsgemeinschaft. We acknowledge the skillful work of the mechanical workshop of the Physics Department and of Jean-Luc Schenker.

References

- [1] G. M. Baule, R. McFee, “Detection of the magnetic field of the heart,” *Am. Heart J.* **66**, 95-96 (1963).
- [2] D. Cohen, E. A. Edelsack, J. E. Zimmerman, “Magnetocardiograms taken inside a shielded room with a superconducting point-contact magnetometer,” *Appl. Phys. Lett.* **16**, 278-280 (1970).
- [3] W. Andrä, H. Nowak (eds.), “Magnetism in Medicine” (Wiley-VCH, Berlin 1998).
- [4] Yu. A. Kholodov, A. N. Kozlov, A. M. Gorbach, “Magnetic fields of biological objects” (Nauka Publisher, Moscow 1990).
- [5] I. Tavarozzi, S. Comani, C. Del Gratta, G. L. Romani, S. Di Luzio, D. Brisinda, S. Gallina, M. Zimarino, R. Fenici, R. De Caterina, “Magnetocardiography: cur-

- rent status and perspectives. Part I: Physical principles and instrumentation,” *Ital. Heart J.* **3**, 75-85 (2002).
- [6] I. Tavarozzi, S. Comani, C. Del Gratta, S. Di Luzio, G. L. Romani, S. Gallina, M. Zimarino, D. Brisinda, R. Fenici, R. De Caterina, “Magnetocardiography: current status and perspectives. Part II: Clinical applications,” *Ital. Heart J.* **3**, 151-165 (2002).
- [7] A. L. Bloom, “Principles of operation of the Rubidium vapor magnetometer,” *Appl. Opt.* **1**, 61-68 (1962).
- [8] C. Affolderbach, M. Stähler, S. Knappe, R. Wynands, “An all-optical, high-sensitivity magnetic gradiometer,” *Appl. Phys. B* **75**, 605-612 (2002).
- [9] G. Bison, R. Wynands, A. Weis, “A laser-pumped magnetometer for the mapping of human cardio-magnetic fields,” *Appl. Phys. B* **76**, 325-328 (2003).
- [10] K. Sternickel, A. Effern, K. Lehnertz, T. Schreiber, P. David, “Nonlinear noise reduction using reference data,” *Phys. Rev. E* **63**, 036209-1-4 (2001).
- [11] Denoising performed courtesy of K. Sternickel (CardioMag Imaging, Inc., Schenectady, USA).
- [12] M. N. Livanov, A. N. Kozlov, S. E. Sinelnikova, Ju. A. Kholodov, V. P. Markin, A. M. Gorbach, A. V. Korinewsky, “Record of the human magnetocardiogram by the quantum gradiometer with optical pumping,” *Adv. Cardiol.* **28**, 78-80 (1981).
- [13] I. O. Fomin, S. E. Sinelnikova, A. N. Koslov, V. N. Uranov, V. A. Gorshkov, “On recording the heart’s magnetic field,” *Kardiologija* **23**, 66-68 (1983).
- [14] P. van Leeuwen, B. Hailer, S. Lange, D. Donker, D. Grönemeyer, “Spatial and temporal changes during the QT-interval in the magnetic field of patients with coronary artery disease,” *Biomed. Tech.* **44**, 139-142 (1999).

Chapter 5

Mapping of the cardiomagnetic field using a room-temperature magnetometer

G. Bison
R. Wynands
A. Weis

Biomedizinische Technik **48**, Suppl. 2, (2004), in press.

5.1 Introduction

The cardiomagnetometry community has stressed on several occasions that more affordable magnetometers are needed to help magnetocardiogram (MCG) diagnostics become widely accepted [1]. At present even the clinical validation of the MCG is affected by the restricted availability of cardio-magnetometers. As a cost-effective alternative to the currently used SQUID-detectors we have developed a novel room-temperature magnetometer based on the magnetic resonance of cesium vapor that allows us to map the cardio-magnetic field and its dynamics.

5.2 Methods

The magnetometer is a variant of the so-called optical pumping magnetometer (OPM). Common to all OPMs is the use of a vapor of paramagnetic atoms — usually sealed in a glass-cell — as the actual sensor. The name OPM refers to a process called optical pumping, which aligns (polarizes) the spins of the atoms by irradiating them with circularly polarized light. As the spins of the atoms interact with the magnetic field as well as with the light, the optical properties of the polarized vapor become magnetic-field dependent, thus allowing one to measure the field by optical means. Many schemes of OPMs have been developed since the 1960s, differing mainly in the way the optical properties of the medium are measured. Having an affordable multichannel cardiomagnetometer in mind, we opted for a detection

technique known as optically detected magnetic resonance. Our device is a scalar magnetometer that can tolerate quite large magnetic fields up to the earth's field with only mild constraints on the direction of the field. This is a significant advantage compared to many other OPMs that require very well defined and homogenous magnetic fields, or even zero background fields. In contrast to the classical design that uses discharge lamps, we use circularly polarized light ($3 \mu\text{W}$) from a single-mode extended-cavity diode laser to polarize the atoms. The wavelength of the laser (894 nm) is actively stabilized to the $6S_{1/2} \rightarrow 6P_{1/2}$ absorption line of the cesium atoms. In an external magnetic field B_0 generated by large coils, the sample polarization precesses around the field axis at the Larmor frequency $\omega_L = \gamma|B_0|$, where γ is a material-dependent constant. This precession is driven by a second magnetic field oscillating at the frequency ω_{rf} . As a consequence, the power of the light beam transmitted through the sample is modulated in a synchronous way. This modulation is detected with a photodiode placed behind the sample. We measure the relative phase ϕ of the oscillating photocurrent with respect to the oscillating magnetic field. When $\omega_{\text{rf}} = \omega_L$ (resonance condition) this phase is $\phi_0 = -90^\circ$. Any small change of the magnetic field corresponds to a change $\Delta\omega_L$ of the Larmor frequency and induces a change of the phase by an amount $\Delta\phi$, which is proportional to $\Delta\omega_L$. This is the essence of the detection of the small field perturbations ΔB produced by the heart field. In the free-running mode ω_{rf} is fixed and $\Delta\phi$ is recorded as a measure for the magnetic field strength. This mode of operation is sensitive only if ω_{rf} is close to ω_L , thus limiting the acceptable variation of magnetic fields to several nT. To overcome this restriction, ω_{rf} can be actively stabilized to the center of the magnetic resonance using ϕ_0 as a reference for a feedback control system. In this way ω_{rf} is phase-locked to the Larmor frequency.

The slope $\Delta\phi/\Delta B$ of the phase response to field changes is proportional to the lifetime τ of the sample magnetization (polarization). The addition of an inert buffer gas to the cesium vapor reduces depolarizing wall collisions, thereby strongly increasing τ . The required sensitivity for cardiomagnetic measurements can only be achieved with long spin lifetimes on the order of several ms. In many OPM designs the atoms integrate the magnetic field during their spin lifetime τ , resulting in a slow response to magnetic field changes. Depending on the mode of operation much higher bandwidths than those corresponding to the time constant τ can be achieved. Figure 5.1 shows the frequency response of the magnetometer to an oscillating magnetic field generated by a test coil. In the free-running mode the response is mainly limited by τ resulting in a bandwidth of 30 Hz (Fig. 5.1 a,b). In the phase-locked mode the bandwidth is much higher and is limited by delays in the feedback loop only (Fig. 5.1 c).

The intrinsic sensitivity of the magnetometer has been calculated from the signal-to-noise ratio of the detection and the width of the magnetic resonance and is on the order of $80 \text{ fT}/\text{Hz}^{1/2}$. Magnetic interference from perturbations in our magnetically noisy laboratory is orders of magnitude larger than the heart magnetic field. We use a shielded room (suppression of 50Hz interference by a factor of 150) in combination with a first-order gradiometer consisting of two identical OPMs to suppress ambient magnetic noise (see Fig. 5.2). The reference magnetometer (OPM2, PD2, LIA2 in

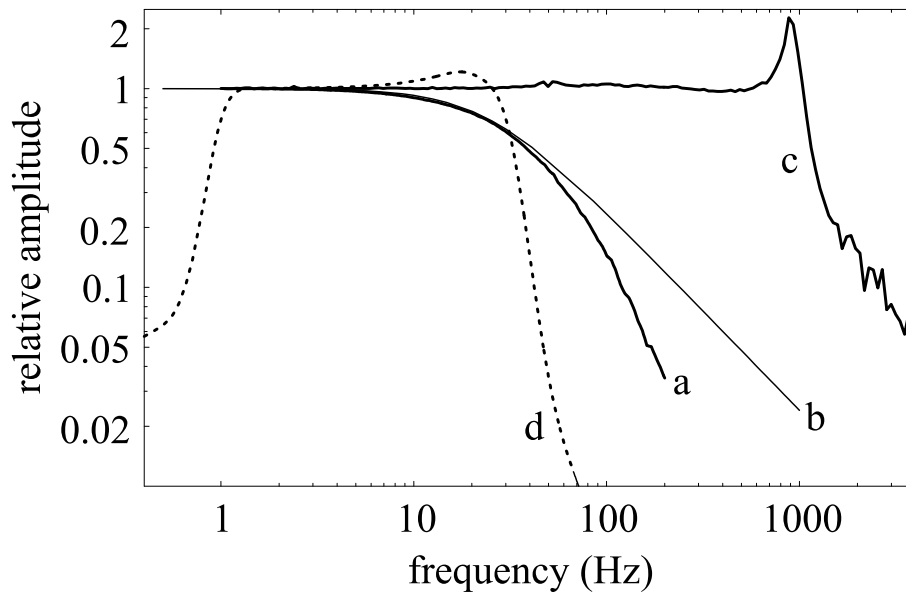


Figure 5.1: Frequency response of the magnetometer. a) Free-running mode (bandwidth 30Hz). b) Theoretical curve for a spin lifetime of 6.6 ms. The discrepancy between a) and b) can be explained by the presence of additional filters in the detection system. c) Phase-locked mode (bandwidth 1000 Hz). d) Optimal (Wiener) filter used for off-line data treatment.

Fig. 5.2) is operated in the phase-locked mode, generating the radio-frequency rf common to both magnetometers. The heart magnetometer proper (OPM1, PD1, LIA1 in Fig. 5.2), operated in free-running mode, detects the difference between ω_{rf} and its own Larmor frequency, thus generating the gradiometer signal.

As the heart magnetometer is operated in free-running mode it suffers from the bandwidth limitation mentioned above. Future designs will overcome this limitation by operating all magnetometers in the phase-locked mode and using a digital-electronic or software gradiometer for noise suppression. In the present study an optimal (Wiener) filter (Fig. 5.1 d) was used to extract the part of the frequency spectrum where the signal lies above the noise. Additionally the filter was modified to correct for the limited bandwidth in this part of the spectrum, resulting in a flat frequency response till 30 Hz. In order to record magnetic field maps with our single channel gradiometer, a nonmagnetic bed on a low-friction support is used to place the subject at well-defined positions with respect to the sensor. By recording 100-s long MCG time series at each of 6x6 grid points (separated by 40 mm) across the chest a two-dimensional map of the Bz-component (perpendicular to the skin) of the MCG field of the subject is obtained. A three-lead ECG time series was recorded simultaneously to the MCG as a reference for off-line averaging. Time-resolved magnetic field maps recorded with this technique as well as details about the off-line data treatment are published in [3].

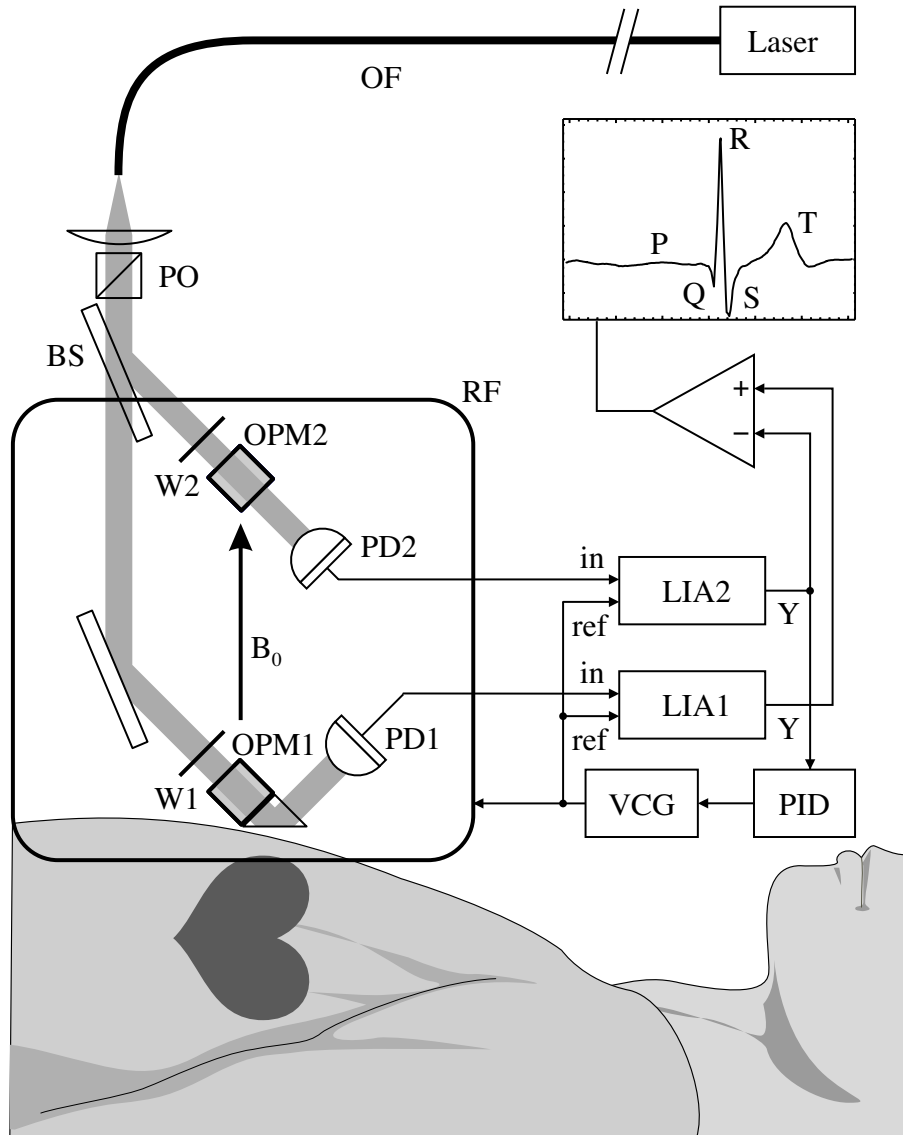


Figure 5.2: Schematic of the gradiometer with read-out and stabilization electronics (not to scale). The separation of the two magnetometers is 7 cm. LIA: lock-in amplifier, VCO: voltage-controlled oscillator, PID: electronic servo control, PD: photodiode, PO: polarizer, BS: beam splitter, W: quarter-wave plate, OF: optical fiber.

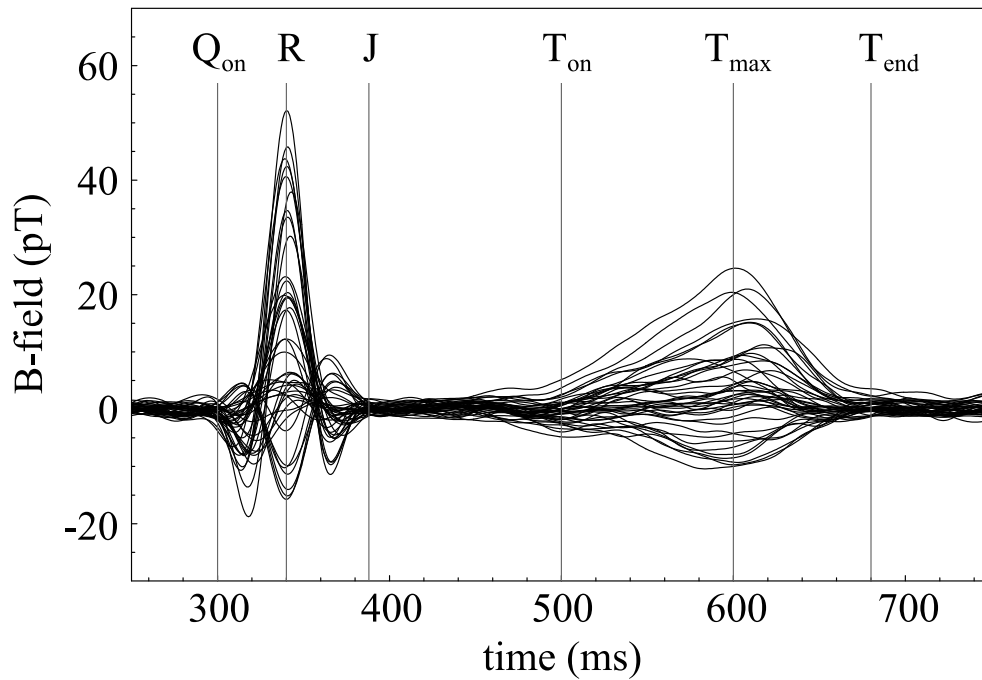


Figure 5.3: Overlapped MCG pulses with the time indices used for time normalization.

5.3 Results

So far, magnetic field maps (MFM) of four different healthy subjects (three male, one female) were recorded with or device. Figure 5.3 shows the overlapped MCG-pulses of the most recent measurement. We used a time normalization based on six time indices (see Fig. 5.3) in order to compare different measurements. The indices were manually set and used to match the pulse to a standard pulse by linear interpolation.

The data was further analyzed by generating iso-field maps using third-order interpolation in two dimensions [3, 5]. A resulting map is shown in Fig. 5.4. As these maps are difficult to interpret for untrained observers, we extracted from our maps the so-called MFM orientation as a simple quantitative parameter, a concept described in [4]. The MFM orientation calculated from the centers of gravity of the positive and negative field amplitudes are shown in Fig. 5.5. Nearly all points fall within the 95% confidence interval found for healthy subjects using a SQUID magnetometer [5] (gray area in Fig. 5.5).

5.4 Discussion

Results as displayed in Fig. 5.5 show that our room-temperature magnetometer is capable of producing diagnostically relevant information. During the intervals with high signal amplitudes, the MFM orientation can be determined quite accurately

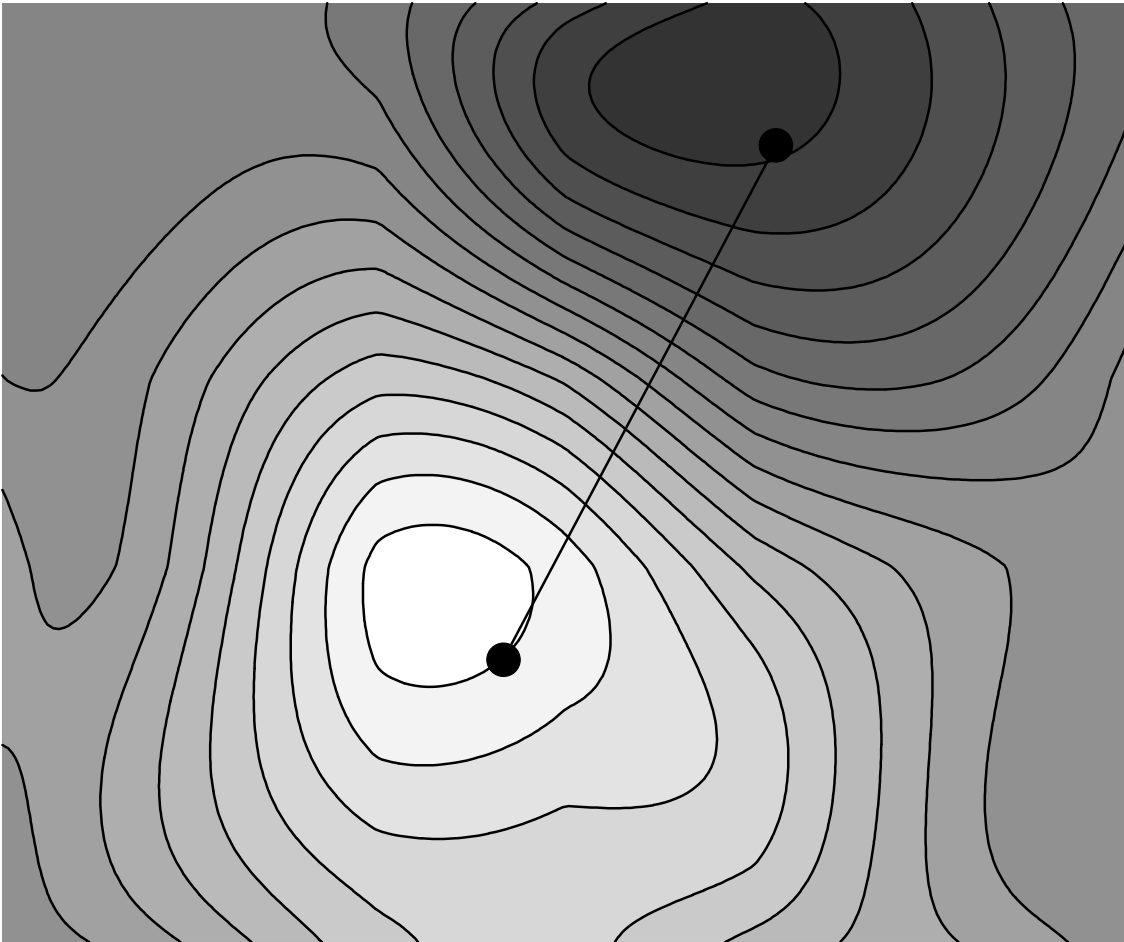


Figure 5.4: Magnetic field map of a healthy volunteer at the maximum of the T wave, measured with the room-temperature laser magnetometer at 7x6 positions. The line indicates the MFM orientation.

whereas for intervals with low signals — like between J and T_{on} or after T_{end} — the values become noisier. From Fig. 5.3 it becomes apparent that at the present stage of development the noise floor still affects the signal during the quiet intervals. Nevertheless, the good agreement of the SQUID-generated reference data and the traces recorded with our OPM inspires confidence that the two detection techniques lead to comparable results. Another approach of comparing SQUID and OPM generated magnetic field maps is published in [6]. Both studies show that our OPM-based MCG technique can be a valuable addition to the arsenal of diagnostic methods in cardiology.

Acknowledgements

This work was supported by grants from the Schweizerischer Nationalfonds and the Deutsche Forschungsgemeinschaft. The authors thank S. Ulzega and Ch. Andreeva

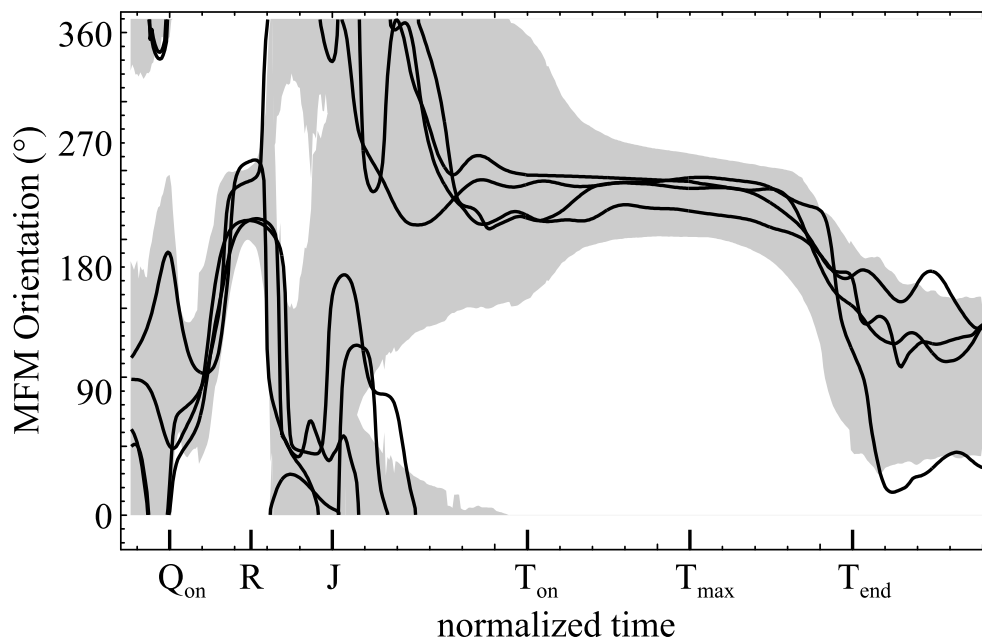


Figure 5.5: Magnetic field map (MFM) orientation for four mappings performed with our magnetometer. Gray bands: data from [5], showing 95% confidence intervals of MFM orientations recorded with healthy subjects using a multi-channel SQUID detector.

for volunteering as additional test persons. A special thank is due to Peter van Leeuwen for sharing his data on MFM orientation with us.

References

- [1] I. Tavarozzi, S. Comani, C. Del Gratta, S. Di Luzio, G. L. Romani, S. Gallina, M. Zimarino, D. Brisinda, R. Fenici, R. De Caterina, “Magnetocardiography: current status and perspectives. Part II: Clinical applications,” *Ital. Heart J.* **3**, 151-165 (2002).
- [2] G. Bison, R. Wynands, A. Weis, A laser-pumped magnetometer for the mapping of human cardio-magnetic fields. *Appl. Phys. B* **76**, 325-328 (2003)
- [3] G. Bison, R. Wynands, A. Weis, Dynamical mapping of the human cardio-magnetic field using a room-temperature, laser-optical sensor. *Opt. Express*, **11**, 904-909 (2003).
- [4] P. van Leeuwen, B. Hailer, S. Lange, D. Donker, D. Grönemeyer, Spatial and temporal changes during the QT-interval in the magnetic field of patients with coronary artery disease, *Biomed. Tech.* **44**, 139-142 (2003).
- [5] P. van Leeuwen, A. Klein, K. Matil, D. Geue, C. Poplutz, S. Lange, B. Hailer,

Dietrich Grönemeyer, Influence of area of coverage on cardiac magnetic field map orientation, *Biomed. Tech.* (2003).

- [6] R. Fenici, G. Bison, R. Wynands, D. Brisinda, A. M. Meloni, A. Weis, Comparison of Magnetocardiographic Mapping with SQUID-based and Laser-pumped Magnetometers in Normal Subjects, *Biomed. Tech.* **48**, Suppl. 2, (2004), in press (see Chapter 6).

Chapter 6

Comparison of magnetocardiographic mapping with SQUID-based and laser-pumped magnetometers in normal subjects

R. Fenici
G. Bison
R. Wynands
D. Brisinda
A. M. Meloni
A. Weis

Biomedizinische Technik **48**, Suppl. 2, (2004), in press.

6.1 Introduction

From the point of view of the average clinician, an ideal instrument for magnetocardiographic mapping (MCG) should be multichannel, easy to operate and maintenance-free, low cost, and reliable at patient bedside. Presently available systems for multichannel magnetocardiography are based on SQUID technology, which is expensive and implies the additional difficulty and cost of continuous system refrigeration with liquid helium. Also HT-SQUID technology, which would at least cut the cost of refrigeration, although rapidly progressing, is still very expensive. Recently, interesting results have been reported with a novel single-channel optical-pumping magnetometer (OPM) [1, 2], which technology could simplify most of the above mentioned problems. However so far preliminary measurements with the OPM were carried out in a non clinical environment. Therefore it was necessary to validate their quality and reproducibility through comparison with recordings carried out in the same subjects with a multichannel MCG system designed for clinical use in an unshielded hospital environment. This has been the aim of our cooperative

pilot study, which preliminary results are reported here.

6.2 Methods

Two normal male volunteers were investigated first with the single-channel OPM [1, 2] (sensitivity $80 \text{ fT/Hz}^{1/2}$ at 1 Hz, first-order gradiometer) of the department of physics in the University of Fribourg. Thereafter the same subjects were studied with the 36-channel DC-SQUID system [3] (sensitivity $20 \text{ fT/Hz}^{1/2}$ at 1 Hz, second-order gradiometer) of the Catholic University in Rome (Fig. 6.1). The z component of the cardiac magnetic field was mapped, using the same 36-point grid ($20 \times 20 \text{ cm}^2$). The time required for equivalent 36-points MCG mapping was about 1.5 hours with the single channel OPM sequential mapping, and 90 sec for multichannel mapping, respectively. After time averaging of row data, averaged data were converted to the same format, and analyzed with the same software (Neuromag-HUT, Helsinki, Finland). For inverse source localization and imaging the Equivalent Current Dipole (ECD) and Current Density Imaging (CDI) models, in a realistic standard torso, were applied.

6.3 Results

A first rough comparison between OPM and the Rome MMCG system was done, in a first case, on the morphology of the QRS and T wave magnetic field distribution, after “manual” alignment of the OPM recordings, to coincide with the typical 36-point recording grid used in Rome. Morphological comparison at the QRS and T wave peaks was satisfactory (Fig. 6.2).

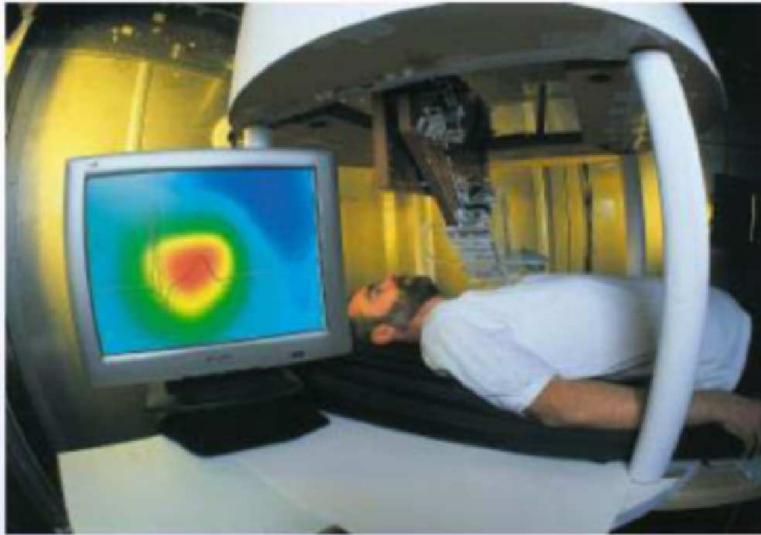
Therefore a more accurate analysis was attempted after conversion of averaged data to a third common format readable with the Helsinki software. Also with this software it was confirmed that OPM signals were of quality good enough to reconstruct in both investigated cases, not only the ventricular MFD but also that related to atrial depolarization (Fig. 6.3). However, atrial OPM source localization with the ECD model was in a wrong position, when compared with that obtained with SQUID signals (Fig. 6.3-6.5).

In both cases, besides the ECD mode and CDI provided an impressive and reproducible imaging of ventricular depolarization and repolarization. In particular CDI, carried out in time coincidence with the depolarization of the interventricular septum, at the peak of the QRS and of the T wave, were almost identical in both cases, independently of the recording system. Moreover also interindividual reproducibility was surprisingly good (Fig. 6.6).

6.4 Discussion

Preliminary measurements carried out in Fribourg more than one year ago and recently published [1], had already shown the high potential of their laser pumped

- **Single-channel OPM (Fribourg)**



- **36-channel SQUID MCG (Rome)**



Figure 6.1: Overview of the two different instrumentations used for the comparison. The OPM is still at the stage of a physics laboratory prototype.

Case 1: GB

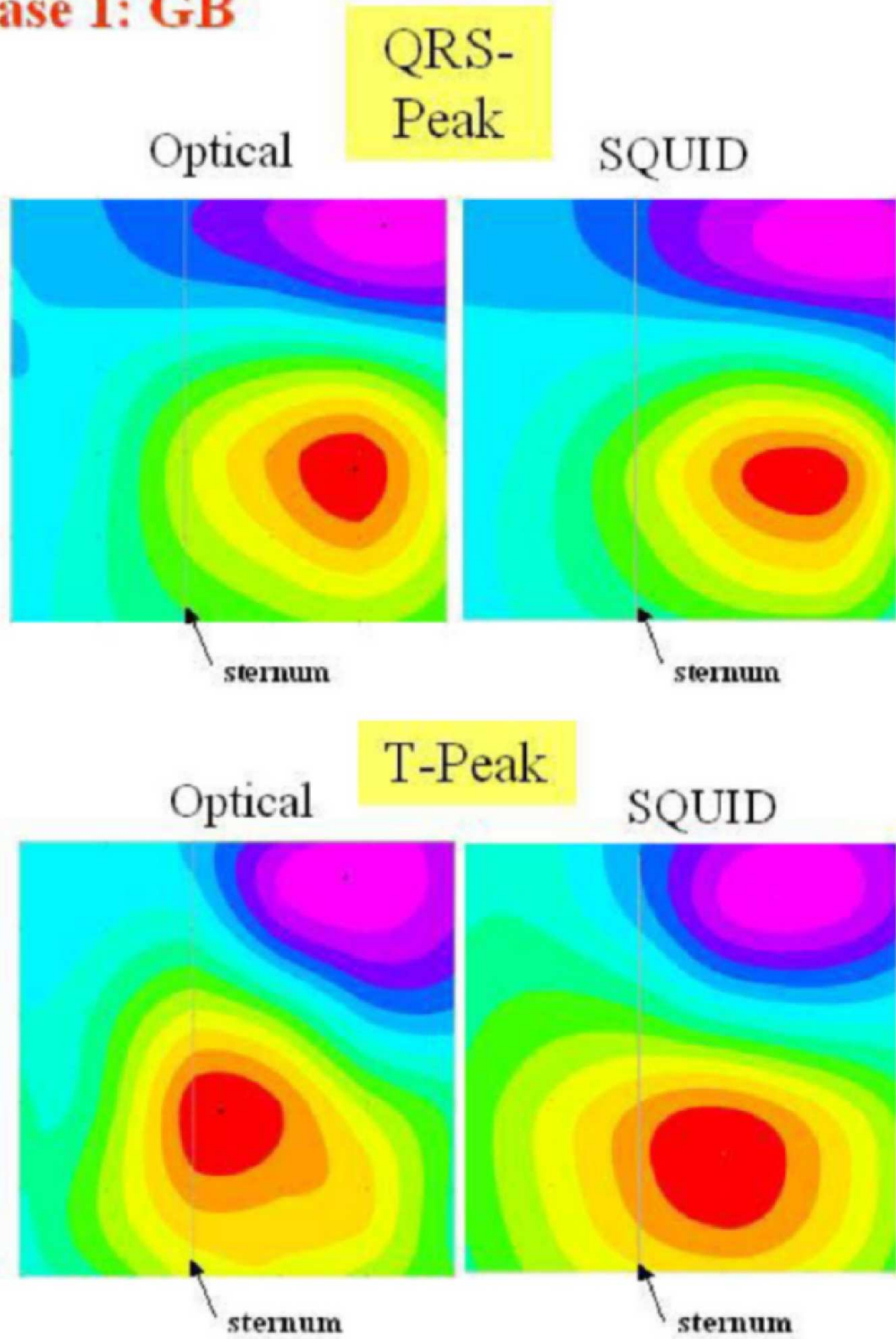


Figure 6.2: First comparison of MFD from MCG recorded with optical (Fri-bourg) and cryogenic (Rome) magnetometers in case 1.

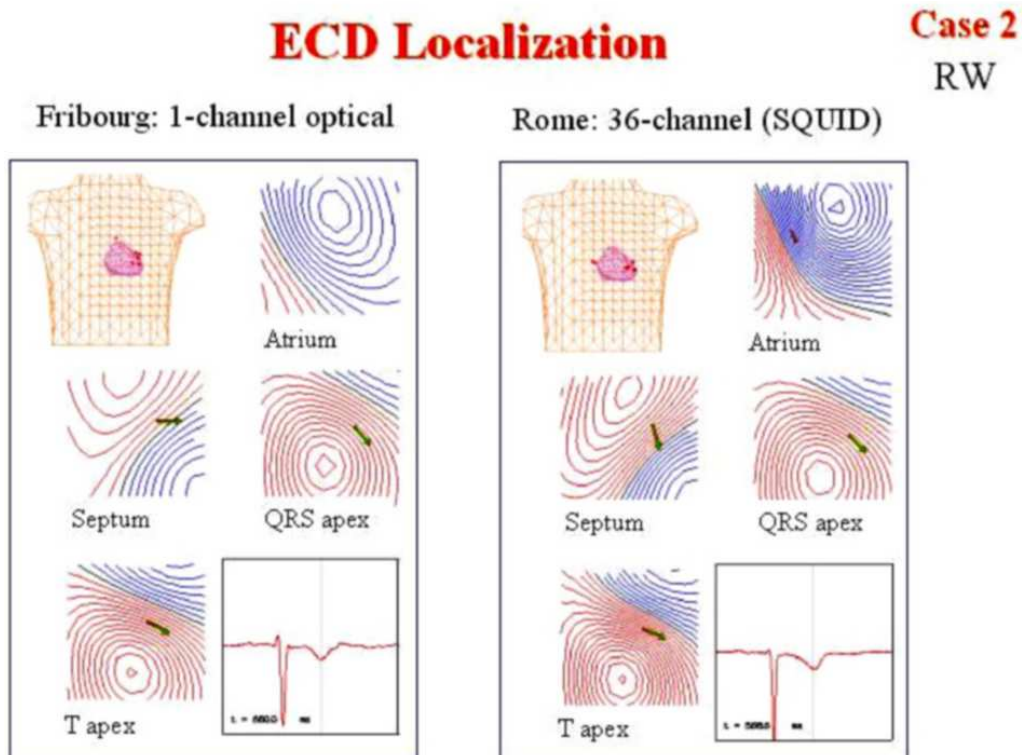


Figure 6.3: Comparison of MFD and source localization, in case 2, after conversion of the averaged data to the Helsinki data format.

magnetometer to record human magnetocardiograms very similar to those usually obtained with cryogenic sensors. However, at the moment OPMs are intrinsically less sensitive than SQUID detectors and clinical experience, validating the quality of imaging of cardiac magnetic fields provided by OPM, was completely tacking. The Rome 36-channel system for clinical MMCG has been already validated with both clinical and experimental studies [3, 4, 5, 6], and by comparative recordings carried out in the Helsinki shielded room. Therefore it can be considered a reliable reference system to test the quality of the recordings obtained with the OPM. The comparative measurements reported in this paper, although carried out in two normal cases only, suggest that MCG mapping, carried out with a single OPM in a shielded room, provides MCG patterns well consistent with those obtained with a state-of-art unshielded multichannel SQUID-based systems.

Therefore we believe that, although at the moment still confined in a shielded room, OPMs have the potential to compete in a near future with cryogenic sensor, especially taking into account that OPM are potentially one order of magnitude less expensive than SQUID sensors and practically maintenance- and cost-free.

The impressive results of our preliminary comparative measurements warrant further investigation. However, they suggest that an investment to construct an OPM-based multichannel system, working without the need of shielded rooms, is more that justified and should be considered as soon as possible. Such a new device

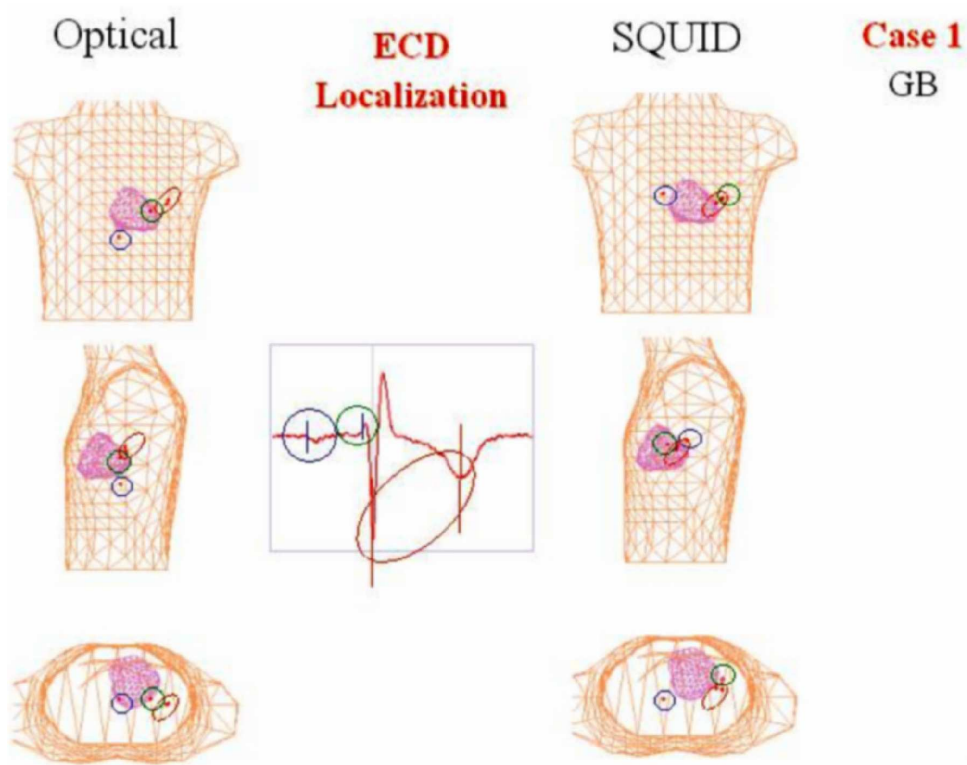


Figure 6.4: Comparison of MCG 3D localizations with the ECD model, at the P wave peak, ventricular septum depolarization QRS and T peaks, in case 1.

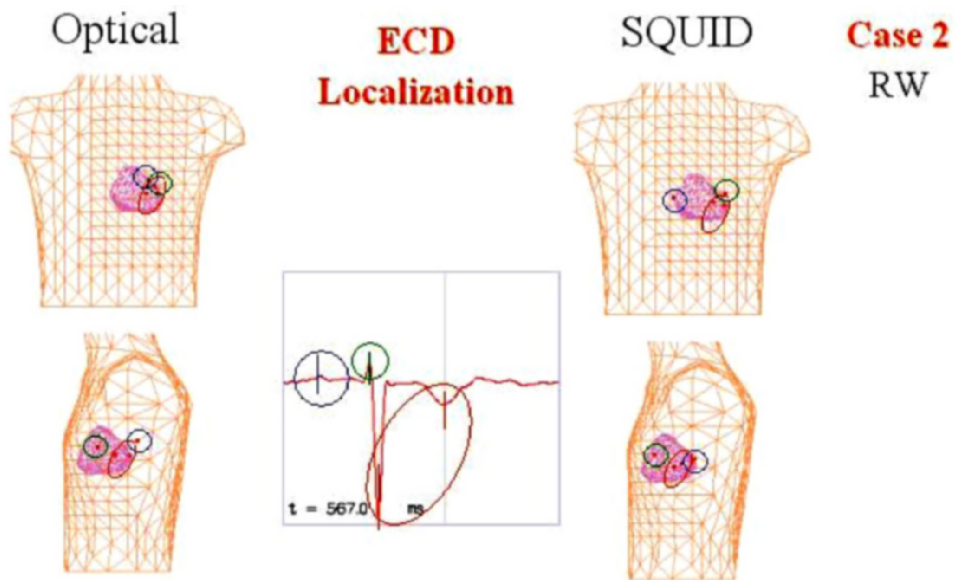


Figure 6.5: comparison of MCG localizations with the ECD model, at the P wave peak, at interventricular septum depolarization, and at QRS and T peaks, in case 2.

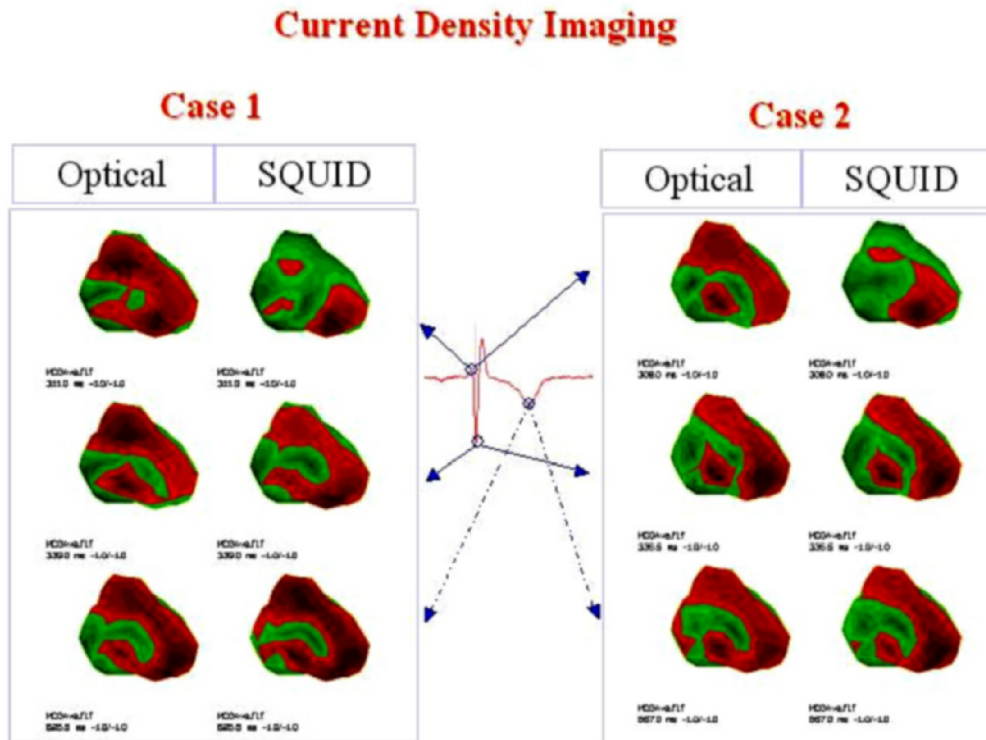


Figure 6.6: Comparison of Current Density Imaging, in case 1 and 2, at inter-ventricular septum depolarization, and at QRS and T peaks. Intraindividual and interindividual reproducibility are impressive, with both recording systems.

in fact would contribute to a faster and broader clinical acceptance of MCG as a diagnostic tool, taking into account the recent demonstration that unshielded MMCG is gathering a significant interest for the detection of cardiac ischemia [7], the triage of patients with acute chest pain [8], and for the monitoring of fetal cardiac electrogenesis [9].

Acknowledgements

Partially supported by MIUR grants # 9906571299_001 and 2001064829_001.

References

- [1] Bison G, Wynands R, Weis A. A laser-pumped magnetometer for the mapping of human cardio-magnetic fields. *Appl. Phys.* 2003 76: 325-328.
- [2] Bison G, Wynands R, Weis A. Dynamical mapping of the human cardiomagnetic field using a room-temperature, laser-optical sensor. *Opt. Express* 2003, 11: 904-909, 2003.

- [3] CardioMag Imaging Inc. (CMI), Schenectady, USA, 36- channel system 2436 (alpha version).
- [4] Fenici R, Brisinda D, Meloni AM, Fenici P. First 36- channel System for Clinical Magnetocardiography in Unshielded Hospital Laboratory for Cardiac Electrophysiology. *International Journal of Bioelectromagnetism* 2003, 5: 80-83.
- [5] Fenici R, Brisinda D, Nenonen J, Fenci P. Phantom validation of multichannel magnetocardiography source localization. *PACE* 2003, 26 (1, Part II): 426-430.
- [6] Fenici R, Brisinda D, Nenonen J, Fenici P. Non invasive study of preexcitation by multichannel magnetocardiography. *PACE* 2003, 26 (1, Part II): 431-435.
- [7] Brisinda D, Meloni AM, Fenici R. First 36-channel Magnetocardiographic Study of CAD Patients in an Unshielded Laboratory for Interventional and Intensive Cardiac Care. In: Magnin I, Montagnat J, Clarysse P, et al, Eds., *Proceedings of Functional Imaging and Modelling of the Heart*. June 5-6 2003 Lyon France. Springer, Berlin, 2003.
- [8] Park JW, Gerk U, Reichert U, et al. Magnetocardiography for the diagnosis of ischemica heart disease in bundle brunch block patients with acute chest pain: results of the Hoyerswerda Registry Study. *Proceedings of the 3rd World congress on heart disease July 12-15 2003 In Washington DC*.
- [9] Wakai RT, Strasburger JF, Li Z, Deal BJ, Gotteiner NL. Magnetocardiographic rhythm patterns at initiation and termination of fetal supraventricular tachycardia. *Circulation* 2003, 107(2): 307-12.

Chapter 7

Conclusions and Outlook

With this thesis several important milestones of the cardiomagnetometry project of the FRAP group have been achieved. An optical magnetometer was designed, built, optimized and successfully used for MCG measurements. Data from two volunteers recorded with the optical magnetometer were compared to data recorded with SQUID magnetometers and showed that the device works as expected — at least with healthy subjects. However, there is much room for improvements of the present device, which are discussed in the following sections.

7.1 Future improvements of the sensor

The comparison of data recorded with commercial SQUID magnetometers and our optical device have shown that SQUID measurements are less affected by noise even in unshielded environments. As a consequence, a major goal for the future development of the optical cardiomagnetometer is to decrease that noise level in order to increase the diagnostic value of the recorded data.

7.1.1 Coated cells

The high intrinsic resolution of the optical magnetometer described in Chapter 2 is mainly due to the excellent detection signal/noise ratio obtained at an operation temperature of 53°C. In order to improve the sensor one can either aim at further increasing that signal/noise ratio or aim at decreasing the magnetic resonance linewidth. Since the signal/noise is already quite high decreasing the linewidth seems therefore to be the more promising route to follow.

The magnetic resonance of the buffer gas cells used in the optical magnetometer is inhomogeneously broadened by magnetic fields gradients. This broadening can be avoided using coated cells where the atoms fly on ballistic trajectories with many wall collisions thereby effectively averaging the magnetic field over the cell volume. Due to this effect, called motional narrowing, signals from coated cells are less sensitive to magnetic field gradients. For the use of optical magnetometers in unshielded clinical environments, where gradients probably can not be avoided, this is a crucial improvement that will be studied in the future.

So far we relied on a Russian supplier for coating the cells with paraffin and filling them with Cs by vacuum distillation. The unit price for such a filling is 500 US\$. In order to become independent of that supplier we have set-up a small glass-blowing workshop with a filling station in our laboratory. A laboratory technician is in the course of being trained for the preparation of the cells. So far he has already successfully filled buffer gas cells. He is currently undertaking first steps to prepare coated cells.

7.1.2 Double pass

The relatively high operation temperature (53°C) that turned out to be optimal for the buffer gas magnetometer might be a problem for hospital use of the optical magnetometer. One advantage of the optical magnetometer is that the sensor cells can be placed very near — as close as 2 mm — to the surface of the patient's chest leading to larger cardiac signals than with cryogenic SQUID magnetometers. However, in that configuration the surface of the sensor is heated to about (50°C) and may be touched by the patient's chest.

The advantage of heated cells is the higher atomic density in the gas phase. As a consequence the optical absorption is larger and leads to lower transmitted light power and a larger modulation depth. Since the shot-noise is proportional to the square root of the transmitted DC power the high operation temperature yields a low shot-noise and a large signal amplitude. This effect is overcompensated by an additional broadening of the resonance at very high temperatures leading to the optimum at 53°C . A similar effect can also be obtained without heating the cell. When the laser beam, after having passed the cell, is reflected onto itself by a mirror, the optical path length through the atomic medium is doubled (Fig 7.1 a). In optically thin media this leads to a doubling of the absorption with the same signal/noise-ratio increase as from heating.

In principle multiple reflections (see Fig 7.1 b) or even a resonant cavity could be used to increase the optical path length substantially. For such arrangements glass cells with low reflection loss are needed, which represent an intolerable increase of complexity. Furthermore the effective gain in signal/noise is limited by losses in the mirror reflections resulting in no substantial improvement compared to the double-pass configuration.

For buffer gas cells that need to be illuminated by large laser beams an alternative configuration has to be used because atoms outside of the beam do not contribute to the signal (Fig. 7.1 c).

7.1.3 Higher order gradiometers

The noise of the first order gradiometer signal (Fig. 7.2 a) measured by the present device is dominated by magnetic noise due to fluctuating gradients. This is the most important reason why the magnetometer does not show a noise level limited by its intrinsic noise. SQUID-based magnetometers use higher order gradiometers to suppress not only fluctuating field components but also fluctuating gradients. A

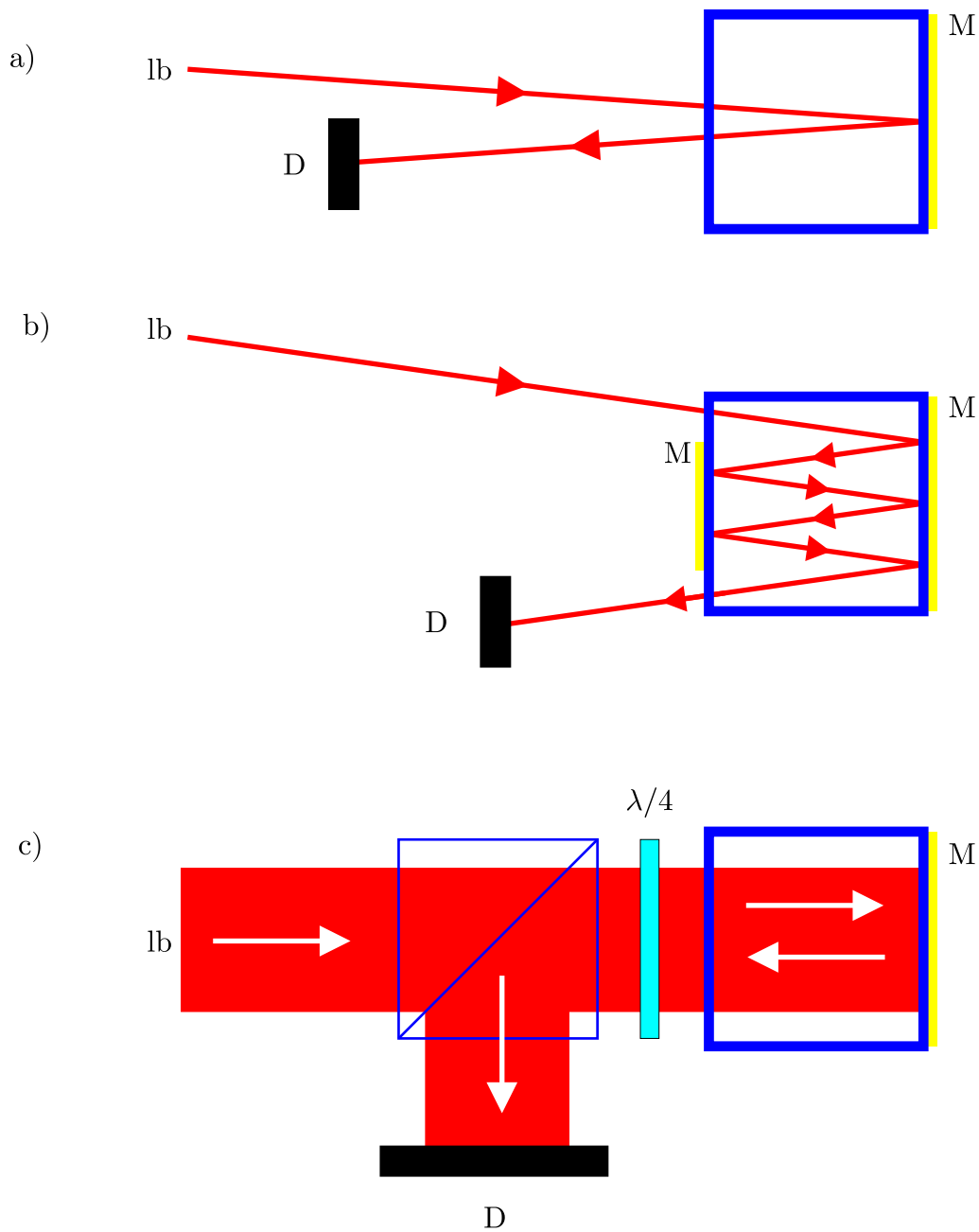


Figure 7.1: a) Double pass configuration. The laser beam (lb) passes the glass cell and is reflected by the mirror M. The reflected beam passes the cell again and is detected by the detector D. The small deviations from the optimal angle $\theta = 45^\circ$ can be neglected since the sensitivity is proportional to $\sin 2\theta$. b) Multipass configuration. The double pass configuration can be extended to a multipass configuration using two mirrors. c) For extend beams as they are used with buffer gas cells the reflected beam can be deflected using a quarter wave plate ($\lambda/4$) in combination with a polarizing beamsplitter cube (pbc). After the quarter wave plate the polarization of the reflected beam is orthogonal to the incident polarization and is deflected by the pbc towards the detector D.

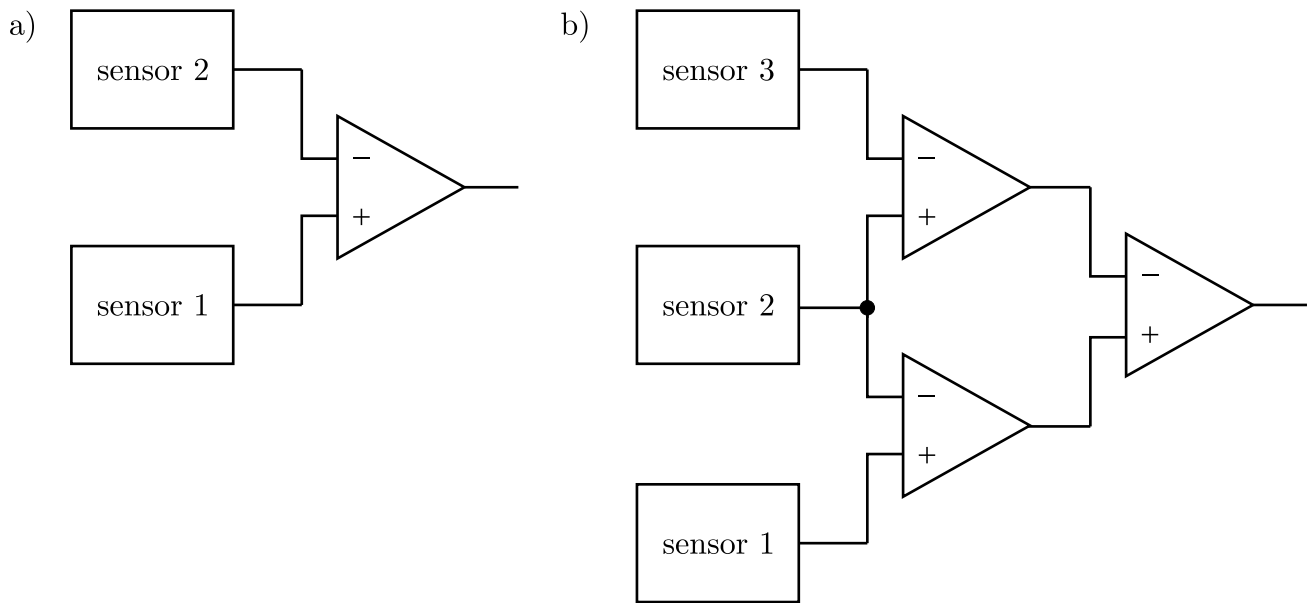


Figure 7.2: a) First order gradiometer. b) Second order gradiometer.

second order SQUID gradiometer (Fig. 7.2 b), for example, can reach a noise level of $20 \text{ fT}/\text{Hz}^{1/2}$ in unshielded environments. Similar second order gradiometers should greatly increase the performance of the optical magnetometer as well and will be tested in the future.

7.1.4 Multichannel arrangement

A cardiomagnetometer for clinical use, such as state-of-the-art SQUID detectors, should have multiple channels covering the relevant region of the chest so that a complete map can be recorded simultaneously. Multichannel recording will reduce the data acquisition time from two hours to two minutes, allowing us to examine patients with a heart condition which cannot be expected to lay still for two hours. However, the scaling of the device from the present single channel configuration to a 30 channel device is a nontrivial technological task.

7.2 Outlook

An important goal for the future of the project is to compare the diagnostic power for heart diseases of optical and SQUID-based magnetometers. Therefore a new version of the optical magnetometer has to be constructed that can be placed in a hospital environment. In parallel some inconvenient aspects of the present device will be improved. These improvements involve the design of integrated electronics, of a user friendly laser system, of advanced denoising software and of inexpensive shielding chambers with compensation coils. Since some of these tasks clearly exceed

the competencies of the FRAP group we have gathered a consortium of partners in different countries (CD, D, I, GR) with complementary expertise for attaching the task. Six research groups and three companies have expressed their interest to join us in a project (CardIMAG) for which we applied funding at the 6th Framework Program of the European Union. After a first meeting with the new partners and the acceptance of the EU of our pre-proposal we are confident that the project will be successfully continued and that one day optical cardiomagnometers may become a standard clinical tool.

Danksagung

An dieser Stelle möchte ich allen danken, die zum Gelingen dieser Arbeit beigetragen haben.

Ein besonderer Dank gilt Prof. Antoine Weis. Ich möchte mich herzlich für die enge Zusammenarbeit mit ihm als begeisterten und begeisternden Wissenschaftler und Lehrer bedanken. Auch für die Freiheit, die ich beim Durchführen der Experimente genossen habe, möchte ich mich bedanken. Das dadurch entgegengebrachte Vertrauen habe ich immer als sehr motivierend empfunden. Neben der wissenschaftlichen Betreuung möchte ich mich auch für die interessanten Reisen — vor allem nach Russland — bedanken, bei denen sich Tun als erfahrener Kenner der verschiedensten Sitten (vom Konzertbesuch bis zum Vodka trinken) erwies.

Dr. Robert Wynands gilt ebenfalls besonderer Dank für seine enge Unterstützung „mit Herz, Hand und Verstand“, die auch nach seinem Wechsel zur PTB nicht abbricht. Ich denke gerne an die spannenden Tage zurück, in denen wir die ersten Signale gemessen haben und für die er seinen Urlaub unterbrach. Ebenfalls bedanken möchte ich mich für den hohen Grad an Perfektion, den Robert bei unseren Publikationen etabliert hat.

Dr. Sergio-Nicola Erné möchte ich für sein Interesse an meiner Arbeit danken. Mit seinem Enthusiasmus gab er mir das Gefühl, dass die Ergebnisse meiner Doktorarbeit sinnvoll genutzt werden können, und hat mich in der Entscheidung bestärkt, weiter an diesem Thema forschen zu wollen. Ihm und Dr. Frank Scheffold danke ich ausserdem dafür, dass sie sich bereit erklärt haben, die Begutachtung zu übernehmen.

Den Mitarbeiterinnen und Mitarbeitern am Herzmagnetometrieprojekt, Silke Ospelkaus-Schwarzer, Philippe Sproll, Martin Rebetez, Hervé Saudon und Mondher Gatri danke ich für die freundliche Zusammenarbeit, die hohe Motivation und die guten Ergebnisse. Stephan Gröger danke ich für interessante Diskussionen und dafür dass er die Präzisionsmagnetometrie in unserer Gruppe voran gebracht hat.

Bei den Mitgliedern unserer Arbeitsgruppe, Taro Eichler, Patrick Haymoz, Adrian Hofer, Xueren Huang, Peter Moroshkin, Reinhard Müller-Siebert, Christian Ospelkaus, Stephan Tandler und Simone Ulzega bedanke ich mich für das gute Arbeitsklima und für die Hilfsbereitschaft.

Daniel Nettels und Ulrich Rasbach möchte ich besonders für ihre Freundschaft, die über die Arbeit hinaus ging, und die lustigen Stunden in Labor, Büro und diversen Kneipen danken. Daniel ist aber auch ein interessanter Diskussionspartner, der mich mit kritischen Fragen oft einem besseren Verständnis der Physik näher gebracht hat.

I thank Paul Knowles for useful discussions and a critical reading of the manuscript. Special thanks extended to the volunteers, Robert Wynands, Simone Ulzega, and Christina Andreeva who patiently lay still during the two hours necessary for the measurements.

Daniel Nettels, Stephan Gröger und besonders Tun Weis und Robert Wynands danke ich für das kritische Lesen der Manuskripte und für die vielen Verbesserungsvorschläge.

Angewandte Projekte wie dieses kommen nicht ohne die Hilfe der technischen Werkstätten aus. Die vielgelobte Qualität der mechanischen wie elektronischen Werkstatt des Departements hat entscheidend zum Gelingen dieser Arbeit beigetragen. Besonders möchte ich Elmar Moser, Oswald Raetzo, Jean-Luc Schenker, Roland Schmid, und Roger Vonlanthen danken.

Ich danke dem Schweizerischen Nationalfonds für die Finanzierung der Projekte (Nr. 21-63401.00 und Nr. 205350-100441), die diese Arbeit möglich gemacht hat.

Schließlich danke ich meinen Eltern, die mir ermöglicht haben, im Ausland zu studieren ohne den Kontakt zur Heimat zu verlieren. Sie haben mich immer unterstützt und ermutigt meinen Weg zu gehen.

Curriculum vitae G. Bison

Name Bison
First Name Georg, Paul
Date of birth 10.10.1974
Place of birth Bonn, Germany
Nationality German
Marital status Unmarried
Languages German (native speaker)
English (fluent)
French (basic knowledge)
Private address Place du Petit-Saint-Jean 39
CH-1700 Fribourg
T: +41 78 817 95 80
Professional address Département de Physique
Université de Fribourg
Chemin du Musée 3
CH-1700 Fribourg
T: +41 26 300 90 31
F: +41 26 300 96 31
E-Mail georg.bison@unifr.ch



Education

June 1994 Abitur (high school diploma)
1994-1999 Physics studies at the University of Bonn
1997-1998 One year course on European patent and trademark law.
1999-2000 Diploma work directed by Prof. A. Weis, "Low-field-magnetometry with optically pumped cesium vapor", in German
August 2000 Physikdiplom (master in Physics), Universität Bonn
since 2000 Ph.D. Student at the University of Fribourg
March to June 2003 Create Switzerland Entrepreneurship Course

Professional Activities

1993-2000 Independent computer consultant for both hardware and software.

Teaching Activities

- 1999-2000 Student lab assistant, University of Bonn
2000-2004 Lecture assistant for 8 semesters covering the lectures “Physics 1”, “Physics 2”, “Computer Programming”, and “Optics” at the University of Fribourg

Papers

1. *A laser-pumped magnetometer for the mapping of human cardio-magnetic fields*, G. Bison, R. Wynands, A. Weis, Appl. Phys. B **76**, 325-328 (2003), Rapid Communication
2. *Dynamical mapping of the human cardiomagnetic field with a room-temperature, laser-optical sensor*, G. Bison, R. Wynands, A. Weis, Optics Express **11**, 904-909 (2003)
3. *The human heart beat detected by cesium atoms* A. Weis, G. Bison, R. Wynands Physical and Chemical News, accepted for publication, 2003.
4. *Search for a Neutron Electric Dipole Moment: Status Report*, E. Alexandrov, M. Balabas, G. Bison, K. Bodek, M. Daum, A. Dovator, A. Fomin, P. Geltenbort, R. Henneck, S. Kalinin, K. Kirch, I. Krasnoshokova, M. Lasakov, V. Marchenkov, A. Murashkin, A. Pazgalev, I. Potapov, M. Sazhin, U. Schmidt, A. Serebrov, G. Shmelev, I. Shoka, R. Taldaev, V. Varlamov, A. Vasiliev, A. Weis, N. Yakobson, PSI-Scientific report R-00-05 2003.
5. *Mapping of the cardiomagnetic field using a optical room-temperature magnetometer* G. Bison, R. Wynands, and A. Weis, Biomed. Tech. **48**, Suppl. 2, (2004), in press.
6. *Comparison of Magnetocardiographic Mapping with SQUID-based and Laser-pumped Magnetometers in Normal Subjects*, R. Fenici, G. Bison, R. Wynands, D. Brisinda, A. M. Meloni, and A. Weis, Biomed. Tech. **48**, Suppl. 2, (2004), in press.
7. *Optimization and performance of an optical cardiomagnetometer*, G. Bison, R. Wynands, and A. Weis, submitted to JOSA B (2004).

Proceedings

1. *Interaction time caused modification of absorption and fluorescence of atomic cesium vapor* V. Papoyan, D. H. Sarkisyan, Yu. P. Malakyan, G. Bison, and A. Weis, Proceedings of the Conference on Laser Physics-2000, Ashtarak (Armenia), 2000.
2. *Resonant nonlinear magneto-optical effects of atoms in vapors, beams and quantum crystals* A. Weis (invited key note lecture), G. Bison, D. Nettels, U. Rasbach, and R. Müller-Siebert. International Conference on Coherent and Nonlinear Optics, Minsk (Belarus), 2001 SPIE proceedings.

3. *Magnetocardiography using optical gradiometers*, R. Wynands (presenter), G. Bison, S. Schwarzer, C. Affolderbach, A. Weis, International Conference on Atomic Physics (ICAP), Cambridge (USA), July 2002.
4. *Performance of a room temperature optical cardio-magnetometer*, G. Bison (speaker), S. Schwarzer, R. Wynands, and A. Weis, Proceedings of the 13th International Conference on Biomagnetism, Jena, Germany, August 2002
5. *The human heart beat detected by cesium atoms*, A. Weis (speaker), G. Bison, and R. Wynands, Physique des Interactions Rayonnement-Matiere, Settat/Marrakech, February 2003.
6. *A laser-optical magnetometer for the mapping of the human cardio-magnetic field*, G. Bison (speaker), R. Wynands, and A. Weis, Proceedings of the Second International Conference on Laser Optics for Young Scientists. St. Petersburg, Russia, July 2003
7. *Laser cardiomagnetometry - our hearts beat for cesium* R. Wynands (invited talk), G. Bison, A. Weis, Proceedings of the International Conference on Atomic Physics (ICOLS) XVI, Palm Cove (Australia), July 2003. key note lecture

Invited Talks

- *Wie die Cäsiumatome das Herz schlagen sehen*, G. Bison (speaker), R. Wynands, A. Weis, Seminar-talk at the Institute for Physical High Technology Jena, Germany 18.12.2002.
- *A laser-optical magnetometer for the mapping of the human cardio-magnetic field*, G. Bison (speaker), R. Wynands, A. Weis, 11th Conference on Laser Optics, St. Petersburg, Russia, July 2003.
- *Optical Pumping Magnetometers*, G. Bison (speaker), R. Wynands, and A. Weis, invited key-note lecture at the conference for Kryoelektronische Bauelemente (Kryo '03), Blaubeuren Oktober 2003.

Patent applications

- A. Weis, R. Wynands, G. Bison, Magnetic resonance device, Europäische Patentanmeldung (Nummer 02 405 506.3), Juni 2002.

Awards

- “Best Paper Award” for “Towards an optical cardio-magnetometer” presented at the International Quantum Electronics Conference and Conference on Lasers, Applications, and Technologies for Young Scientists in Moscow, June 2002.

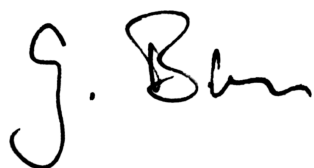
- “Young Investigators Award” for the paper “Performance of a room–temperature optical cardiomagnetometer” presented at the International Conference on Biomagnetism in Jena, Germany (August 2002).
- “Best Paper Award” for “A laser-pumped magnetometer for the mapping of human cardiomagnetic fields” presented at the Second International Conference on Laser Optics for Young Scientists in St. Petersburg (July 2003).
- “Innovation Award”¹ of the Wall Street Journal Europe (November 2003).
- “Phonak Preis 2004” for Applied Physics of the Swiss Physical Society (March 2004).
- “Berthold Leibinger Innovationspreis”², Nomination by the Berthold Leibinger Foundation, Ditzingen, Mach 23, 2004.
- NETS Prize 2004 of the Gebert Rüb Foundation “New Entrepreneurs in Technology and Science, Selected High Potential of the Year”.

¹The University of Fribourg, represented by G. Bison, R. Wynands, and A. Weis, was selected as “Runner-Up” with special mention of the Jury in the Biotech-Medical category.

²A. Weis, G. Bison, and R. Wynands were nominated by the Jury for “price worthy research work” in the field of applied laser physics with the topic *Laser magnetometer for realtime diagnostics of the beating human heart* .

Ich versichere, dass ich diese Arbeit selbstständig und ohne unerlaubte Hilfe verfasst und keine anderen als die angegebenen Quellen und Hilfsmittel benutzt sowie Zitate kenntlich gemacht habe.

1700 Freiburg (Schweiz), den 28. April 2004

A handwritten signature in black ink, consisting of a large, stylized 'G' followed by a period and the letters 'Bison' in a cursive script.

Georg Bison